

ABSTRACT

Title of dissertation: **GAS-FILLED AXISYMMETRIC
ACOUSTIC RESONATORS**

Adel El-Sabbagh, Doctor of Philosophy, 2005

Dissertation directed by: **Professor Amr Baz
A. James Clark School of Engineering**

In this dissertation, the harmonic oscillations of gas-filled axisymmetric acoustic cavities near resonance conditions are considered. This problem has gained considerable interest during the last decade when compression ratios of up to 340% have been achieved. The objective of this dissertation is to develop theoretical models that can predict the performance of resonators of complex geometries in a straightforward manner to enable the selection of optimal resonator configurations that yield high compression ratios. With this goal in mind, a mathematical model is developed based on the equations of conservation of mass, linear momentum, and state equation for ideal gas. The model accounts for the full nonlinear behavior of the gas oscillations. The equations are cast in a weighted residual form which can be solved provided that the exact mode shapes for the linear problem can be determined. The model is proved to be accurate in capturing experimental phenomena such as the formation of shock waves at large excitations. However, it is solvable only for resonators with simple geometries. In order to overcome these deficiencies, a finite element model is developed based on the weak form of the governing equations. The finite element

model enables the prediction of resonators of complex geometries with either body or boundary excitation sources at different flow conditions.

Furthermore, the model is integrated with the dynamics of axisymmetric piezoelectric bimorphs that are used to actuate the acoustic cavity instead of the conventional actuation systems. The coupling between the cavity and piezoelectric bimorph models is achieved by considering their mutual interactions. The validity of the coupled model is validated experimentally and against the predictions of a commercial finite element software (ANSYS) that deals with linear acoustic equations. Close agreement is obtained between theory and experiment indicating that the developed analytical and experimental tools can be confidently used in the design of axisymmetric acoustic resonators that possess a high potential of applicability in designing smart structures and vibration control.

GAS-FILLED AXISYMMETRIC
ACOUSTIC RESONATORS

by

Adel El-Sabbagh

Dissertation submitted to the Faculty of the Graduate School of the
University of Maryland, College Park in partial fulfillment
of the requirements for the degree of
Doctor of Philosophy
2005

Advisory Committee:

Professor Amr Baz, Chair/Advisor
Professor Balakumar Balachandran
Professor Inderjit Chopra
Professor Norman Wereley
Professor Donald DeVoe

© Copyright by
Adel El-Sabbagh
2005

DEDICATION

To family.

ACKNOWLEDGMENTS

I would like to thank my advisor, Prof. A. Baz for all the support he provided to me during the past four years. Through him, I have learnt a lot of wonderful things. In my humble opinion, the most important of which is to have perseverance and resolution to do the best. Because of him my graduate experience has been one that I will cherish forever.

I am indebted to all my teachers in Ain Shams University especially Prof. A. Elkharboutly who guided me during my first steps on this path.

I also owe my gratitude to all my friends and coworkers who have made this work possible. It will be difficult to mention all the names but I wish they all know how much I appreciate their help.

I am also thankful to my parents who have always given me the support I needed throughout my entire life. Although being almost 10,000 miles away, everyday I feel blessed by their prayers. My brothers have always provided guidance, support, and tenderness.

I cannot express my gratitude to my wife Yomna. Her sacrifices are most appreciated. To her, I would like to present a bouquet of flowers, on which is written "I know you did all of this out of love. Thank you!"

Last but definitely not least, I would like to thank my two young boys; Belal and Hesham in whose eyes I always see fresh hope.

Finally, all praise is due to Allah Who blessed me with all these loving people.

TABLE OF CONTENTS

1	Introduction	1
1.1	Literature Survey	1
1.2	Objectives	9
1.3	Scope of Work	11
2	Theoretical Analysis of Acoustic Resonators	13
2.1	Introduction	13
2.2	Theoretical Model	14
2.2.1	Governing Equations	14
2.2.2	Velocity Potential Function	16
2.2.3	Dimensionless Variables	19
2.2.4	Model Analysis	20
2.2.5	Solution and Post Processing	27
2.3	Application of the Model	29
2.3.1	Cylindrical Resonators	29
2.3.2	Exponential Resonator	37
2.3.3	Linearly Varying Area Resonators	41
2.4	Theoretical Model of Piston Driven Resonators	46
2.4.1	Equations of Piston Driven Resonators	47
2.4.2	Boundary Conditions of Piston Driven Resonators	49
2.5	Summary	51
3	Finite Element Formulation for Arbitrary Shaped Resonators	53
3.1	Introduction	53
3.2	Finite Element Model for Entirely Driven Resonators	54
3.2.1	Free Oscillations of Entirely Driven Resonators	55
3.2.2	Forced Oscillations of Entirely Driven Resonators	58
3.3	Numerical Examples for Entirely Driven Resonators	64
3.3.1	Cylindrical Resonators	64
3.3.2	Exponential Resonators	65
3.3.3	Linearly Varying Area Resonators	67
3.3.4	Conclusion for the Model Performance	68
3.4	Finite Element Model for Piston Driven Resonators	69
3.4.1	Free Oscillations of Piston Driven Resonators	70
3.4.2	Forced Oscillations of Piston Driven Resonators	71

3.5	Axisymmetric Resonators with External Flow	73
3.5.1	Finite Element Modeling for Flow Boundary Conditions	74
3.5.2	Numerical Examples for Resonators with Flow	77
3.6	Summary	79
4	FEM of a Coupled Nonlinear Model for Acoustic Resonators Driven by Piezoelectric Bimorphs	81
4.1	Introduction	81
4.2	Basic Model of the Fluid System	83
4.2.1	Free Oscillations of the Fluid System	83
4.2.2	Nonlinear Forced Oscillations of the Fluid System	86
4.2.3	Fluid Flow Across the Boundaries of the Resonator	89
4.3	Piezoelectric Bimorph Actuators	89
4.4	Combining and Coupling the Fluid and Piezoelectric Actuator Models	96
4.4.1	Combined System	96
4.4.2	Coupled System	98
4.4.3	Forced Oscillations of the Coupled System	100
4.5	Evaluation of the Coupled System Model	102
4.5.1	Uncoupled Vs. Coupled Systems	102
4.5.2	Actuated Piezoelectric Driven Resonators and Geometry Optimization	106
4.6	Intermediate Diaphragm Excitation	110
4.7	Summary	113
5	Experimental Validation	115
5.1	Introduction	115
5.2	Entirely Driven Resonators	116
5.3	Piston Driven Resonators	121
5.4	Resonators with Flow	125
5.5	Axisymmetric Resonators Driven by Piezoelectric Bimorphs	130
5.6	Resonators Driven by Piezoelectric Bimorphs with Intermediate Diaphragm	135
5.7	Commercial Finite Element Software Validation	140
5.7.1	Axisymmetric Acoustic Resonators	140
5.7.2	Piezoelectric Bimorph Actuators	140
5.7.3	Piston Driven Acoustic Resonators	142
5.7.4	Coupled Acoustic-Piezoelectric Models	144
5.7.5	Resonators with Intermediate Diaphragm	145
5.8	Summary	146
6	Contributions and Future Work	149
6.1	Contributions	149
6.2	Future Work	152
6.2.1	Resonator Geometry Optimization	152
6.2.2	Double Cavity Resonator	152

6.2.3	Piezo-Acoustic Actuation System	153
6.2.4	Refrigeration Compressors	155

LIST OF TABLES

2.1	Natural frequencies of linearly varying area ducts with two different parameters versus a straight duct with the same length $l = 0.165$ m, with $c_0 = 330$ m/s.	44
4.1	Physical, mechanical and electrical properties of a 2.5" piezo-electric bimorph.	103
5.1	Physical, mechanical and electrical properties of a 3" piezo-electric bimorph.	131

LIST OF FIGURES

2.1	Pressure ratio predicted at one end of a cylindrical resonator excited at different frequencies $\Omega = (0.9, 0.95, 0.98, 1, 1.02, 1.05)$, with an amplitude $a_0 = 100g$. ($D = 0.01, l = 0.165$ m, $c_0 = 330$ m/s, $\gamma = 1.2, N = 20$).	31
2.2	Pressure ratio predicted at one end of a cylindrical resonator excited at $\Omega = 1$ with different acceleration amplitudes $a_0 = \{10, 100, 300\}g$. ($D = 0.01, l = 0.165$ m, $c_0 = 330$ m/s, $\gamma = 1.2, N = 20$).	32
2.3	Pressure ratio predicted at one end of a cylindrical resonator excited at $\Omega = 1$ with different acceleration amplitudes $a_0 = \{10, 100, 300\}g$. ($D = 0.04, l = 0.165$ m, $c_0 = 330$ m/s, $\gamma = 1.2, N = 20$).	33
2.4	Pressure ratio predicted at different locations of a cylindrical resonator ($X = \{0.0, 0.2, 0.4, 0.6, 0.8, 1.0\}$), excited at $\Omega = 1, a_0 = 100g$. ($D = 0.01, l = 0.165$ m, $c_0 = 330$ m/s, $\gamma = 1.2, N = 20$).	34
2.5	Evolution of the time dependent coefficients $\eta_1(T)$ and $\eta_1(T)$ at 1g in a cylindrical cavity excited at $\Omega = 1$. ($D = 0.01, l = 0.165$ m, $c_0 = 330$ m/s, $\gamma = 1.2, N = 2$).	35
2.6	Pressure ratio at 1g in a cylindrical cavity excited at $\Omega = 1$. ($D = 0.01, l = 0.165$ m, $c = 330$ m/s, $\gamma = 1.2, N = 2$).	36
2.7	Evolution of the time dependent coefficients $\eta_1(T)$ and $\eta_1(T)$ at 100g in a cylindrical cavity excited at $\Omega = 1$. ($D = 0.01, l = 0.165$ m, $c_0 = 330$ m/s, $\gamma = 1.2, N = 2$).	36
2.8	Pressure ratio at 100g in a cylindrical cavity excited at $\Omega = 1$. ($D = 0.01, l = 0.165$ m, $c_0 = 330$ m/s, $\gamma = 1.2, N = 2$).	37
2.9	Pressure ratio predicted at the small end of an exponential resonator ($\alpha = 5.75$) excited at different frequencies $\Omega = \{1.288, 1.329, 1.342, 1.356, 1.370, 1.383\}$ with an amplitude of $a_0 = 250g$. ($D = 0.01, l = 0.224$ m, $c_0 = 330$ m/s, $\gamma = 1.2, N = 5$).	39

2.10	Pressure ratio predicted at the small end of an exponential resonator ($\alpha = 5.75$) excited at $\Omega = 1$ with different amplitudes $a_0 = 100g, 250g, 400g$. ($D = 0.01, l = 0.224$ m, $c_0 = 330$ m/s, $\gamma = 1.2, N = 20$.)	40
2.11	Geometry of a linearly varying area resonator.	42
2.12	Pressure ratio predicted at the small end of a linearly varying area resonator ($\beta = 10$) excited at $\Omega = 1$ with different amplitudes $a_0 = 10g, 100g, 300g$. ($D = 0.01, l = 0.225$ m, $c = 330$ m/s, $\gamma = 1.2, N = 10$.)	45
2.13	Pressure ratio predicted at one end of a linearly varying area resonator ($\beta = \frac{1}{3}$) excited at $\Omega = 1$ with different amplitudes $a_0 = 50g, 100g, 200g$. ($D = 0.01, l = 0.225$ m, $c = 330$ m/s, $\gamma = 1.2, N = 4$.)	46
3.1	Schematic of an Entirely Driven Resonator.	55
3.2	Three-node acoustic element.	57
3.3	Geometry of a cylindrical resonator (left) and its velocity mode shapes (right).	65
3.4	Comparison of the pressure ratio predictions carried out by the proposed finite element and the exact models for a cylindrical resonator, ($l = 0.165$ m, $c_0 = 330$ m/s, $D = 0.01, \gamma = 1.2$, and $N = 20$.)	66
3.5	Geometry of an exponential resonator (left) with $\alpha = 5.75$ and its velocity mode shapes (right).	66
3.6	Comparison of the pressure ratio predictions carried out by the proposed finite element and the exact models for an exponential resonator ($\alpha = 5.75, l = 0.224$ m, $c_0 = 330$ m/s, $D = 0.01, \gamma = 1.2$, and $N = 10$.)	67
3.7	Geometry of a linearly varying area resonator (left) with $\beta = \frac{1}{3}$ and its velocity mode shapes (right).	68
3.8	Comparison of the pressure ratio predictions carried out by the proposed finite element and the exact models for a linearly varying area resonator ($\beta = \frac{1}{3}, l = 0.225$ m, $c_0 = 330$ m/s, $D = 0.01, \gamma = 1.2$, and $N = 5$.)	69
3.9	Schematic for a Piston Driven Resonator.	70

3.10	Schematic for an axisymmetric resonator with input and output check valves mounted at the ends.	74
3.11	Pressure ratio predicted by the proposed finite element for an entirely driven exponential resonator, $\alpha = 5.75$, $l = 0.224$ m, $c = 330$ m/s, $D = 0.01$, $\gamma = 1.4$, and $N = 10$, under different flow boundary conditions, $v_0 = 0.001c_0, 0.010c_0$, and $0.020c_0$	78
3.12	Pressure ratio predicted by the proposed finite element for a cylindrical resonator, $l = 0.165$ m, $c = 330$ m/s, $D = 0.01$, $\gamma = 1.4$, and $N = 10$, under different flow boundary conditions, $v_0 = 0.01c_0, 0.05c_0$, and $0.10c_0$	78
4.1	Schematic for a three layer piezoelectric bimorph	90
4.2	Schematic for a two-node piezoelectric element	91
4.3	Schematic of a finite element mesh combining both the piezoelectric and acoustic finite element meshes.	96
4.4	Schematic of the axisymmetric resonator used in evaluating the coupled system model.	102
4.5	Mode shapes of the uncoupled system model.	104
4.6	Mode shapes of the coupled system model.	105
4.7	A 0.5 m length resonator geometry.	107
4.8	Pressure ratio predicted by the proposed model at the small end of the 0.5 m resonator shown in Figure 4.7.	107
4.9	Different resonator geometries; bottle, funnel, and cone used in cavity optimization.	108
4.10	Different resonator geometries; bottle, funnel, and cone used in cavity optimization.	109
4.11	A schematic of a diaphragm driven resonator excited by a piezoelectric bimorph.	110
5.1	Experimental setup used for entirely driven resonators. . . .	116
5.2	The resonator used in entirely driven resonator experiments.	117

5.3	Schematic of the dimensions in inch of the resonator used in entirely driven resonator experiments.	118
5.4	Comparison between the experimental and theoretical time histories of the pressure ratio of the entirely driven resonator at 40 g in time domain.	119
5.5	Comparison between the experimental and theoretical time histories of the pressure ratio of the entirely driven resonator at 60 g in time domain.	119
5.6	Comparison between the theoretical and experimental frequency responses of the entirely driven resonator at 40 g. . .	120
5.7	Comparison between the theoretical and experimental frequency responses of the entirely driven resonator at 60 g. . .	120
5.8	Experimental setup used for piston driven resonators using an electromechanical shaker as the drive.	121
5.9	Experimental setup used for piston driven resonators using a Piezoelectric Stack as the drive	122
5.10	Comparison of theoretical (left) to experimental (right) results for piston driven resonators.	123
5.11	Comparison between the predictions of the proposed model and the experimental results of Galiev <i>et al.</i> [22] for a 3.4 m long cylindrical resonator excited at 550g.	124
5.12	LFPX 0500500B Piezoelectric valve, from The LEE Company.	125
5.13	LFPX 0500500B Piezoelectric valve control circuit.	126
5.14	Testing of the piezoelectric valve.	127
5.15	Schematic for the testing of the piezoelectric valve.	127
5.16	Pressure drop in the piezoelectric valve.	128
5.17	Piezoelectric valve mounting on an acoustic resonator.	129
5.18	Entirely driven resonator with flow experimental setup.	129
5.19	Piston driven resonator with flow experimental setup.	131
5.20	Displacements of the piezoelectric bimorph excited at 100 Hz.	132

5.21	Displacements of the piezoelectric bimorph excited at 200 Hz.	132
5.22	Displacements of the piezoelectric bimorph excited at 250 Hz.	132
5.23	Displacements of the piezoelectric bimorph excited at 300 Hz.	133
5.24	Displacements of the piezoelectric bimorph excited at 400 Hz.	133
5.25	Piezoelectric bimorph driven resonator.	134
5.26	Frequency response of the funnel resonator driven by a piezo- electric bimorph.	134
5.27	Time response of the 6 inch resonator driven by a piezoelectric bimorph at {200,250,300} V.	136
5.28	A diaphragm is mounted through springs to a piezoelectric bimorph	137
5.29	Experimental setup for an axisymmetric resonator driven by a piezoelectric bimorph through an intermediate diaphragm.	137
5.30	Frequency response of the axisymmetric resonator driven by a piezoelectric bimorph through an intermediate diaphragm.	138
5.31	Frequency response of the actuator without the diaphragm. .	139
5.32	Frequency response of the actuator with the diaphragm. . . .	139
5.33	Elements and first mode shape of the acoustic resonator built by the ANSYS model.	141
5.34	Schematic of a 20 inch resonator.	141
5.35	Elements and first mode shape of the 3" piezoelectric bimorph built by the ANSYS model.	143
5.36	First mode shape of the 3" piezoelectric bimorph predicted by the proposed model.	143
5.37	Pressure distribution predicted by the ANSYS model for a 3.4 m long cylindrical resonator.	144
5.38	First mode of a 20" acoustic resonator driven by a 3" piezo- electric bimorph.	145

5.39	Pressure distribution predicted by the ANSYS model for a 0.5 m long resonator (a) without the diaphragm and (b) with the diaphragm.	146
6.1	A schematic for a double cavity resonator.	154
6.2	A double cavity resonator mounted on an electromechanical shaker.	154
6.3	A Piezo-Acoustic Actuation System (PAAS).	155
6.4	Use of PAR as a refrigeration compressor.	156

NOMENCLATURE

a	Acceleration
A_{jn}	Coefficient tensor of $\ddot{\eta}$
b_{ij}	flexural stiffness coefficients
B_{jn}	Coefficient tensor of η
\mathbf{B}^e	Finite element matrix for the strain-degrees of freedom relationship
c, c_0	Speed and undisturbed speed of sound
$\mathbf{C}_f, \mathbf{C}_p$	Coupling matrices
C_{jnm}	Coefficient tensor of $\eta\dot{\eta}$
\mathbf{D}	Finite element matrix for the stress-strain relationship
d_{ij}	extensional stiffness coefficients
D_{jn}	Coefficient tensor of $\dot{\eta}$
E_i	Elasticity modulus of the i^{th} layer in a piezoelectric bimorph
E_{jnm}	Coefficient tensor of $\eta\eta\eta$
F	Dimensionless acceleration
F_j	Force vector
FEM	Finite element modeling
\mathbf{F}_{p1}	Force vector on the piezoelectric bimorph due to acoustic pressure
$\mathbf{F}_{p2}^{\text{in,out}}$	Force vector on the piezoelectric bimorph due to electric charges
h_i	height of the i^{th} layer in a piezoelectric bimorph
k_{ij}	coupling stiffness coefficients
$\mathbf{K}_f, \mathbf{K}_p$	Fluid and piezoelectric stiffness matrices

\mathbf{K}	Global stiffness matrix
l	Length of the acoustic cavity
l_f^e, l_p^e	Fluid and piezoelectric element lengths
L^e	Element external work
$\mathbf{M}_f, \mathbf{M}_p$	Fluid and piezoelectric mass matrices
\mathbf{M}	Global mass matrix
N	Number of approximation modes
nl	Number of layers in the piezoelectric bimorph
N_i	Hermite interpolation functions
$\mathbf{N}_f, \mathbf{N}_p$	Fluid and piezoelectric interpolation functions vectors
p, p_0	Pressure and ambient pressure
P, P_0	Dimensionless pressure and ambient pressure
r	Radius and radial coordinate
$r^{\text{in,out}}$	Inner and outer radii of the piezoelectric bimorph
s, S	Dimensional and dimensionless cavity cross sectional area
t, T	Dimensional and dimensionless time
T^e	Element kinetic energy
u_r, u_x	Radial and axial displacements of the piezoelectric bimorph
U^e	Element potential energy
U_i	Voltage across the i^{th} layer in a piezoelectric bimorph
\mathbf{u}^e	Vector of piezoelectric element degrees of freedom
\mathbf{U}	Vector of piezoelectric mode shapes

$v_{0,l}$	Gas flow speeds at the ends of the resonator
v_p	Piston speed
W	Weighting functions
\mathbf{W}^e	Finite element matrix for the strain-displacement relationship
x, X	Dimensional and dimensionless axial coordinates
α	Flare constant of exponential cavity
χ	Local coordinate of the piezoelectric reference element
γ	Ratio of specific heats
δ	Dissipation coefficient
ϵ	Strain vector
η	time dependent functions
φ, Φ	Dimensional and dimensionless velocity potential
ν_i	Poisson's ratio of the i^{th} layer in a piezoelectric bimorph
ρ, ρ_0	Density and undisturbed density of the gas
ρ_i	Density of the i^{th} layer in a piezoelectric bimorph
ρ^e	Element density per unit area
σ	Stress vector
Ψ, ψ	Mode shapes and their nodal values of the gas
ω, Ω	Dimensional and dimensionless operating frequency
ξ	Local coordinate of the gas reference element

Chapter 1

Introduction

1.1 Literature Survey

Study of resonant oscillations in closed cavities is an old problem. As a matter of fact, it has been considered by Rayleigh (1842 - 1919) [1]. The problem considers closed, gas-filled tubes oscillating longitudinally at a frequency in the neighborhood of one of the natural frequencies of the gas column. Most of the work has been directed to the special case where this cavity is a fixed cylinder and the gas is being excited by a plane piston at one of its ends. Hartmann [2] introduced a method to excite cylinders filled with gas at their natural frequencies by impinging a gas jet into the tube. Ilgamov *et al.* [3] have reviewed the work done in this field up to 1996.

The concept of overpressure is a major measure of performance in this field. It is

defined as the difference between the wave's peak and the medium ambient pressures:

$$p_{over} = p_{max} - p_0 \quad (1.1)$$

and the pressure ratio p_{ratio} is defined as

$$p_{ratio} = \frac{p_{max}}{p_0} \quad (1.2)$$

while the pressure amplitude δp at the closed end is defined as

$$\delta p = \frac{p_{max} - p_{min}}{2} \quad (1.3)$$

The linear acoustic theory predicts the pressure amplitude δp at the closed end of a cylindrical resonator of length l harmonically excited at the other end with a piston oscillating at a frequency ω and a velocity amplitude v_p in terms of the density ρ_0 and speed of sound c_0 of the undisturbed gas as follows

$$\delta p = \frac{\rho_0 v_p}{\sin(\frac{\omega l}{c_0})} \quad (1.4)$$

It also defines the n^{th} natural frequency of a standing wave formed inside the cylindrical resonator as [1]

$$\omega_n = \frac{n\pi c_0}{l} \quad (1.5)$$

Equation (1.4) legitimately suggests that attaining large pressure variations is achieved by letting ω approach one of the natural frequencies of the gas column and increasing the excitation amplitude v_p . This is a reason why a lot of researchers have used powerful sources of excitations. For example, electromagnetic vibrators have

been used by Coppens and Sanders [5] and Temkin [6, 7], motor cycle engines by Lettau [4], Sturtevant [8] and Zaripov and Ilgamov [9], electrodynamic shakers by Saenger and Hudson [10], Cruikshank [11] and Lawrenson *et al.* [12], and mechanical generators by Merkli and Thomann [13] and Althaus and Thomann [14]. Due to the nature of these types of drives, most of the researchers used long cylindrical tubes to ensure low fundamental frequencies of the resonators. Lettau [4] for instance has used a 12 m long tube, which makes the fundamental frequency be in the range of 15 Hz.

However equation (1.4) is misleading as the pressure amplitudes experimentally attained were very modest especially when compared to the infinite values predicted by the linear acoustic theory. The highest pressure oscillations for cylindrical tubes were 41 kPa attained by Sturtevant [8] using a 3.2 m length tube with 76 mm bore and an excitation of 49 mm amplitude. The reason of this mismatch is that not only does the linear theory neglect damping but most importantly it fails to describe the strongly nonlinear behavior of the gas dynamics when excited close to resonance conditions. Lettau [4] showed that if the frequency of excitation is close to or coincides with the first fundamental frequency of a gas column in a closed tube, shock waves are formed. The formation of these shock waves sets a limit on the values that the overpressures can attain. The same phenomenon was observed by many other researchers, and hence, there was a conviction that a linear model is not capable of describing the problem.

A major breakthrough occurred in 1998 due to the work of Lawrenson *et al.* [12] as

they achieved pressure amplitudes that far exceeded all the previously demonstrated values. They considered the harmonics (amplitudes and phases) as building blocks that can be used together to build whatever waveform was needed. They showed that shock waves are merely a special case of the infinite family of possible synthesized waveforms. If this special case is avoided, then unshocked waveforms with extremely high overpressures may be attained. They showed that the relative phases and amplitudes of the harmonics can be controlled by the resonator geometry. According to Ladbury [15] consonant resonators (also called harmonic tubes as found in Gaitan and Atchley [16]), which are like a simple cylindrical cavity, have the harmonics of the standing wave coincide with the higher modes of the cavity, providing precisely the conditions needed to generate shocks. In dissonant resonators (also called anharmonic tubes by Gaitan and Atchley [16]), such as a cone, modes are not equally spaced, and so harmonics are less likely to coincide with the cavity modes. As a result, resonators that achieve high pressure amplitudes are most likely to be dissonant. However, it should be noted that many dissonant resonators may produce severe shocks at low pressure amplitudes. Lawrenson et al. [12] carried out experiments on different resonator geometries; cylinder, cone, horn-cone and a bulb. These cavities were mounted on an electrodynamic shaker (entire resonator drive) and charged with refrigerant R-134a at 301 kPa. The dynamic pressure was measured using piezoelectric pressure transducers while the static pressure was measured by a strain-gauge-type pressure transducer. The best performance occurred in the horn-cone cavity as they recorded pressure oscillations up to 1390 kPa (340% of the charge pressure). The horn-cone cavity produces a higher pressure ratio for a given power input than the conical one.

Hysteretic effects were also present as the frequency response of the dynamic pressures inside the cone and bulb cavities were dependent on the direction of the sweep, while in the cylindrical cavity no hysteretic effects were recorded. Sugimoto *et al.* [17] tried to avoid the formation of shock waves in cylindrical tubes by attaching an array of periodic Helmholtz resonators to the cavity and hence converting the consonant cylinder into a dissonant tube. The cavity was driven from one end by a linear motor actuating a bellow. These bellows ensure sealing, yet cause irregularities in the tube diameter. They succeeded in preventing the formation of shock waves but the pressure amplitudes were just a little bit more than 10% of the ambient pressure.

Considerable work has been directed towards putting a theoretical model for the physics of the process. Depending on the observation of shock waves, many authors (for example, Betchov [18], Saenger and Hudson [10], Weiner [19], and Temkin [20]) assumed the solution to the resonance of an acoustic cavity as the sum of continuous and discontinuous parts. The nonlinear effects of oscillations to a second order approximation have been first taken into account by Betchov [18].

According to Ilgamov *et al.*[3], Chester's [21] approach turned out to be the most effective. Chester regarded the inviscid, non-heat-conducting case as the basic problem. Later on, he considered other effects of viscosity and thermal conductivity as some corrections to the solution of the equivalent basic problem, although their effect is usually too small. Boundary layer effects can be more significant, while the most important required modification to the basic problem arises from the nonlinear terms. He solved the dynamic equations of the oscillating gas in Eulerian coordinates. The

solution was presented as a continuous function and a discontinuity which shows the shock wave front. More accurate approaches were found later such as the one by Galiev *et al* [22].

Ilinskii *et al.* [23] developed a one-dimensional mathematical model to analyze nonlinear standing waves. They derived the model equations from the fundamental gas dynamics equations for an ideal gas; namely the conservation of mass, conservation of momentum, and the state equation. They considered the total nonlinearity of gas dynamics and not just the second approximation. Volume attenuation due to viscosity has been considered. The model fits for any axisymmetric resonator with an entire resonator drive. They solved the model numerically using the Runge-Kutta method and the numerical results obtained by the model were found to be in good agreement with the measurements obtained experimentally in Lawrenson *et al.* [12].

Chun and Kim [24] developed a one-dimensional model for the resonant oscillations of gas in axisymmetric closed tubes. They attached the frame of reference to the entirely driven cavity, and they made use of three conservation equations; mass, momentum and energy, and two state equations; the total energy and the ideal gas equations. They used the characteristic boundary conditions to supplement the lack of boundary conditions and solved the resulting equations numerically by using a higher-order finite difference scheme. They carried out simulations on four different shapes of tubes; straight, conical, cosine and $\frac{3}{4}$ cosine, all having the same length, volume and smaller end radius. The last three shapes were meant as examples of shapes in which area increases, increases then converges and increases then decreases, respectively.

They introduced a new measure of performance which is the nonlinear energy ratio that quantifies the degree of nonlinearity of the wave patterns by comparing the autospectrum of the pressure signals to the total signal energy. Again, they found the straight tube is the least efficient because a large portion of the input effort spreads over the higher harmonics. The most efficient as a sonic compressor was the cosine tube which can develop up to 6.1 compression ratio at accelerations of 300 m/s². Their model also captures the hysteresis phenomenon in which the resonance frequencies increase with the increase of the excitation force.

Erickson and Zinn [25] solved the same set of equations in Ilinskii *et al.* [23] but neglected third order nonlinearity terms and showed that these high order terms are insignificant. They used a slightly modified Galerkin method. They applied this method to straight and horn shape ducts. The latter has an exponentially varying cross sectional area and is characterized by the flare constant α . Their trial functions were the natural modes of the acoustic cavity that can be found by solving the Sturm-Liouville form [26]. Their weight functions were the product of the trial functions and the cross sectional area of the cavity. This choice of trial functions is similar to the process of modal analysis as in Meirovitch [27] for example. Their results for the straight ducts were in excellent agreement with the results of Ilinskii *et al.* [23] and Chun and Kim [24] while being at a low computational cost. They also evaluated the maximum compression ratio as a function of the flare constant and found that the compression ratio is not monotonic as the flare constant is increased, and it is maximized at $\alpha = 5.75$.

Vanhille and Campos-Pozuelo [28] developed a numerical finite-difference algorithm for the simulation of nonlinear standing waves including dissipation effects in Lagrangian coordinates. Their development was carried out in the time domain and hence they could capture the transient behavior of the fluid. They performed simulations for amplitudes ranging from linear to strongly nonlinear and weak shocks. Their model was a 1-D model and did not account for cavities with varying cross sectional area.

Sugimoto *et al.* [29] developed a nonlinear cubic theory to obtain the frequency response of the resonator that they described in Sugimoto *et al.* [17]. The results of the model matched the experiments qualitatively but not quantitatively.

Alexeev *et al.* [30] studied heat interactions in resonance tubes. They studied the main effects influencing gas motion in a resonance tube including viscous and thermal gas interactions with the walls of the cavity. Shock waves cause temperature increase of the gas and hence affect the resonant frequencies. Under adiabatic boundary conditions, the theory predicts aperiodic gas oscillations, the frequency of which moves after some time out of the resonance band that contradicts the experimental findings where the gas oscillations are almost periodic and the temperature is practically constant. They proposed a model with isothermal boundary conditions accounting for heat and viscous interactions that lead to a reduction in the pressure amplitude and a change in the oscillation phase as well as periodic gas motion this lead to a good agreement with the experimental data even for large piston amplitudes.

Recently, Li *et al.* [31] applied a quasi-Newton type optimization scheme to find optimized axisymmetric geometrical parameters for the shapes proposed by Ilinskii *et al.* [23] and Chun and Kim [24]; cone, horn-cone, and half-cosine. Assuming an entirely driven resonator filled with R-134a, pressure ratios close to 400% are predicted. In Li *et al.* [32], the same optimization model was validated experimentally with conical resonators for pressure ratios up to 130%. The model was also used to validate the assumed dissipation factor which was -without justification- usually taken as 0.01. They found that a value between 0.011 and 0.012 provided the best fit to the model to experimental data. They used the model to predict pressure ratios up to 500% in their optimized horn cones.

Daniels *et al.* [33] carried out experiments on entirely driven conical resonators with four different configurations. At 80 g's, pressure ratios up to 1.9 have been achieved by using a 0.17 m long resonator. They also studied the effect of ventilating the ends of the resonator on the pressure ratios and found that the pressure definitely decreases with increased flow through the resonator. They also introduced the idea of central blockage in which a cylindrical shaft is fixed along the axis of the resonator. The presence of this central blockage negatively affects the developed pressure ratios.

1.2 Objectives

- The main objective of this work is to develop finite element models to simulate the dynamics/acoustics of axisymmetric acoustic resonators. The developed

models will be able to predict the performance of resonators with complex cavity geometries. The resonators are harmonically excited either by oscillating the whole cavity (entirely driven resonators) or by exciting one of the boundaries while holding the other boundaries fixed (piston driven resonators). Emphasis will be placed on the latter resonator configuration because of its practical implications, low input power requirements, and potential use as an acoustic compressor in numerous applications. The finite element model should be able to handle different scenarios including axisymmetric resonators with boundary flow.

- Piezoelectric actuators that have the advantage of being compact, clean, environment friendly, and highly efficient will be considered as a viable means to replace motor cycle engines and electrodynamic shakers in driving the boundary of the cavity. This necessitates including the interaction between the dynamics of the piezoelectric actuator and the gas-filled resonator in the finite element model. The proposed model can be used to optimally design the acoustic resonator.
- Furthermore, experimental implementation of optimal configurations of the resonator will be carried out to demonstrate the potential of resonators in generating high pressure ratios. Also the experimental results will be used to validate the predictions of the mathematical model in an attempt to develop an accurate predictive tool that can be used to design various resonator configurations.

1.3 Scope of Work

A theoretical model for the standing waves in acoustic cavities will be introduced. Exact analytical solutions are only possible in the case of cylindrical, exponential and linearly-varying area cavities. Approximate solution methods and most specifically the finite element method will be used to predict the performance of axisymmetric cavities with arbitrary geometries. The proposed model will be able to handle both cases of entirely and piston driven resonators with and without flow through the boundaries. A finite element model will be also built for the driving piezoelectric actuator. Both models for the gas inside the resonator and the piezoelectric actuator will be coupled together in order to fully understand and simulate the case of piezoelectric driven acoustic resonators. The validity of the approximate solution will be tested by comparing the predictions to the exact solutions in the cases in which an analytical solution is possible. Once validated, the approximate model is used to simulate different geometries in an attempt to reach an optimal cavity configuration for the resonator that yields maximum pressure ratios. The findings of the theoretical model are to be validated experimentally through a set of experiments carried out on various cavity configurations.

This dissertation is organized into six chapters. Chapter 1 presents a brief discussion of the literature and related work. In Chapter 2, the theoretical analysis of acoustic resonators is presented with applications to resonators of simple geometries. In Chapter 3, a finite element model is developed for arbitrary shaped cavities that are

either entirely or piston driven with flow conditions. Chapter 4 integrates the finite element model with a piezoelectric bimorph that is used to resonate the gas inside the cavity without the need for any moving parts. The experimental performance of the acoustic resonators are presented in chapter 5 for entirely or piezoelectric driven configurations. Comparison between the predictions of the finite element model and the experimental results are also included in Chapter 5. In Chapter 6 the findings and the contributions of this work are summarized. Furthermore, it includes also the recommendations for future studies.

Chapter 2

Theoretical Analysis of Acoustic Resonators

2.1 Introduction

In this chapter, the equations governing the dynamics of acoustic resonators will be presented starting from the basic equations; conservation of the mass, conservation of momentum, and state equations. These equations account also for the forcing functions and the energy dissipation in the cavity. Combining all these equations together, the pressure ratio distribution inside the resonator can be predicted in many practical cases. The development of the nonlinear model is based on the work of Ilinskii *et al* [23], and Erickson and Zinn [25]. As a general case, the resonators are assumed to be entirely driven unless otherwise mentioned.

2.2 Theoretical Model

In this section, the theoretical model of harmonic oscillations of gas-filled acoustic resonators will be developed from the basic governing equations; conservation of mass, momentum and state equations. The resonator is assumed to be entirely driven, with the coordinate system being attached to the moving resonator. The gas inside is ideal and heat exchange at the boundaries is assumed to be negligible.

2.2.1 Governing Equations

There are three basic equations needed to describe the oscillation of an acoustic cavity; the conservation of mass, the conservation of linear momentum and the state equations.

The conservation of mass in a one dimensional space has the form

$$\frac{\partial m}{\partial t} + \frac{\partial m_f}{\partial x} = 0 \quad (2.1)$$

where m and m_f are the mass per unit length of the cavity and the mass flow, respectively. Assuming the cavity to be axisymmetric but otherwise arbitrary, then its cross-sectional area s can be expressed as

$$s = s(x) = \pi(r(x))^2 \quad (2.2)$$

where $r(x)$ is the radius of the resonator at x . Therefore m can be expressed as

$$m = \rho s \quad (2.3)$$

and m_f

$$m_f = \rho u s \quad (2.4)$$

where ρ and u are the density and particle velocity, respectively.

Equations (2.2),(2.3), and(2.4) can be substituted in equation(2.1) to give

$$\frac{\partial(\rho s)}{\partial t} + \frac{\partial(\rho u s)}{\partial x} = 0 \quad (2.5)$$

or

$$\frac{\partial \rho}{\partial t} + \frac{1}{s} \frac{\partial(\rho u s)}{\partial x} = 0 \quad (2.6)$$

The conservation of linear momentum in a one dimensional space is

$$\frac{\partial u}{\partial t} + u \frac{\partial u}{\partial x} = -\frac{1}{\rho} \frac{\partial p}{\partial x} - a(t) + \delta \frac{\partial}{\partial x} \left(\frac{1}{s} \frac{\partial}{\partial x} (s u) \right) \quad (2.7)$$

where p and $a(t)$ are the pressure of the gas and the acceleration of the whole resonator, respectively. δ is the dissipation coefficient, which is assumed to be small.

The state equation actually is developed from the conservation of energy and the equations of ideal gas. Under adiabatic conditions (negligible exchange of heat energy with the surroundings), these equations reduce to the following state equation

$$\frac{p}{p_0} = \left(\frac{\rho}{\rho_0} \right)^\gamma \quad (2.8)$$

where

$$\gamma = \frac{c_p}{c_v} \quad (2.9)$$

is the ratio of specific heats of an ideal gas

2.2.2 Velocity Potential Function

In order to simplify the manipulation of the equations, the velocity potential function φ is introduced instead of the velocity u . The velocity potential function is defined as

$$u = \frac{\partial \varphi}{\partial x} \quad (2.10)$$

After substituting equation (2.10) in the conservation of linear momentum equation (2.7), one gets

$$\frac{\partial^2 \varphi}{\partial t \partial x} + \frac{1}{2} \frac{\partial}{\partial x} \left(\frac{\partial \varphi}{\partial x} \right)^2 = -\frac{1}{\rho} \frac{\partial p}{\partial x} - a(t) + \delta \frac{\partial}{\partial x} \left(\frac{1}{s} \frac{\partial}{\partial x} \left(s \frac{\partial \varphi}{\partial x} \right) \right) \quad (2.11)$$

Integrating equation (2.7) once with respect to x , replacing p in terms of ρ from the state equation (2.8), equation (2.11) yields

$$\frac{\partial \varphi}{\partial t} + \frac{1}{2} \left(\frac{\partial \varphi}{\partial x} \right)^2 = -\frac{\gamma p_0}{(\gamma - 1) \rho_0^\gamma} \rho^{\gamma-1} - a(t)x + \frac{\delta}{s} \frac{\partial}{\partial x} \left(s \frac{\partial \varphi}{\partial x} \right) + \phi(t) \quad (2.12)$$

where $\phi(t)$ is an arbitrary time dependant function.

The speed of sound propagation c is known to be [34]

$$c^2 = \frac{dp}{d\rho} = \frac{\gamma p_0}{\rho_0^\gamma} \rho^{\gamma-1} \quad (2.13)$$

$\phi(t)$ is arbitrary. Hence, it can be chosen as

$$\phi(t) = \frac{c_0^2}{\gamma - 1} \quad (2.14)$$

Equations (2.39) and (2.13) are substituted in equation (2.12) to give

$$\frac{\partial \varphi}{\partial t} + \frac{1}{2} \left(\frac{\partial \varphi}{\partial x} \right)^2 = -\frac{c^2 - c_0^2}{\gamma - 1} - a(t)x + \frac{\delta}{s} \frac{\partial}{\partial x} \left(s \frac{\partial \varphi}{\partial x} \right) \quad (2.15)$$

In order to eliminate the explicit dependance of the velocity potential function φ on the density ρ in equation (2.15), it can be differentiated with respect to time t minding that $\phi(t)$ is chosen constant to give

$$\frac{\partial^2 \varphi}{\partial t^2} + \frac{1}{2} \frac{\partial}{\partial t} \left(\frac{\partial \varphi}{\partial x} \right)^2 = -\frac{\gamma p_0}{\rho_0^\gamma} \rho^{\gamma-2} \frac{\partial \rho}{\partial t} - \frac{da}{dt} x + \frac{\delta}{s} \frac{\partial^2}{\partial t \partial x} \left(s \frac{\partial \varphi}{\partial x} \right) \quad (2.16)$$

while the equation of conservation of mass (2.6) can be expressed as

$$\frac{\partial \rho}{\partial t} = -\frac{1}{s} \frac{\partial (\rho u s)}{\partial x} \quad (2.17)$$

$$= -\frac{1}{s} \frac{\partial}{\partial x} \left(s \rho \frac{\partial \varphi}{\partial x} \right) \quad (2.18)$$

$$= -\frac{\partial \rho}{\partial x} \frac{\partial \varphi}{\partial x} - \frac{\rho}{s} \frac{\partial}{\partial x} \left(s \frac{\partial \varphi}{\partial x} \right) \quad (2.19)$$

then equation (2.19) is substituted in equation (2.16) to give

$$\begin{aligned} \frac{\partial^2 \varphi}{\partial t^2} + \frac{1}{2} \frac{\partial}{\partial t} \left(\frac{\partial \varphi}{\partial x} \right)^2 &= \frac{\gamma p_0}{\rho_0^\gamma} \rho^{\gamma-2} \left(\frac{\partial \rho}{\partial x} \frac{\partial \varphi}{\partial x} + \frac{\rho}{s} \frac{\partial}{\partial x} \left(s \frac{\partial \varphi}{\partial x} \right) \right) - \frac{da}{dt} x \\ &\quad + \frac{\delta}{s} \frac{\partial^2}{\partial t \partial x} \left(s \frac{\partial \varphi}{\partial x} \right) \end{aligned} \quad (2.20)$$

$\partial \rho / \partial x$ can be extracted from equation(2.11) as follows

$$\begin{aligned} \frac{\partial \rho}{\partial x} &= \\ &- \left(\frac{\gamma p_0}{\rho_0^\gamma} \rho^{\gamma-2} \right)^{-1} \left[\frac{\partial^2 \varphi}{\partial t \partial x} + \frac{1}{2} \frac{\partial}{\partial x} \left(\frac{\partial \varphi}{\partial x} \right)^2 + a(t) - \delta \frac{\partial}{\partial x} \left(\frac{1}{s} \frac{\partial}{\partial x} \left(s \frac{\partial \varphi}{\partial x} \right) \right) \right] \end{aligned} \quad (2.21)$$

According to Ilinskii *et al.* [23] the dissipative terms may be dropped from the expression of $\partial\rho/\partial x$ in equation (2.21) as δ is small and the expression of $\partial\rho/\partial x$ appears only in the nonlinear terms of equation (2.20).

Eliminating $\partial\rho/\partial x$ by substituting equation (2.21) into equation (2.20) one gets

$$\begin{aligned} \frac{\partial^2\varphi}{\partial t^2} + \frac{1}{2}\frac{\partial}{\partial t}\left(\frac{\partial\varphi}{\partial x}\right)^2 = & - \left[\frac{\partial^2\varphi}{\partial t\partial x} + \frac{1}{2}\frac{\partial}{\partial x}\left(\frac{\partial\varphi}{\partial x}\right)^2 + a(t) \right] \frac{\partial\varphi}{\partial x} \\ & + \frac{\gamma p_0}{\rho_0^\gamma s} \rho^{\gamma-1} \frac{\partial}{\partial x}\left(s\frac{\partial\varphi}{\partial x}\right) - \frac{da}{dt}x + \frac{\delta}{s}\frac{\partial^2}{\partial t\partial x}\left(s\frac{\partial\varphi}{\partial x}\right) \end{aligned} \quad (2.22)$$

Equation (2.13) is substituted in the previous equation to give

$$\begin{aligned} \frac{\partial^2\varphi}{\partial t^2} + \frac{1}{2}\frac{\partial}{\partial t}\left(\frac{\partial\varphi}{\partial x}\right)^2 = & - \left[\frac{\partial^2\varphi}{\partial t\partial x} + \frac{1}{2}\frac{\partial}{\partial x}\left(\frac{\partial\varphi}{\partial x}\right)^2 + a(t) \right] \frac{\partial\varphi}{\partial x} \\ & + \frac{c^2}{s}\frac{\partial}{\partial x}\left(s\frac{\partial\varphi}{\partial x}\right) - \frac{da}{dt}x + \frac{\delta}{s}\frac{\partial^2}{\partial t\partial x}\left(s\frac{\partial\varphi}{\partial x}\right) \end{aligned} \quad (2.23)$$

The speed of propagation c is expressed in terms of the velocity potential function using equations (2.13) and (2.10)

$$c^2 = c_0^2 - (\gamma - 1) \left[\frac{\partial\varphi}{\partial t} + \frac{1}{2}\left(\frac{\partial\varphi}{\partial x}\right)^2 + a(t)x \right] \quad (2.24)$$

where the dissipative term has been neglected again because it yields highly nonlinear terms.

Equation (2.24) is substituted in equation (2.23) yielding

$$\begin{aligned} \frac{c_0^2}{s}\frac{\partial}{\partial x}\left(s\frac{\partial\varphi}{\partial x}\right) - \frac{\partial^2\varphi}{\partial t^2} = & \frac{da}{dt}x + a(t)\frac{\partial\varphi}{\partial x} + \frac{\gamma-1}{s}a(t)x\frac{\partial}{\partial x}\left(s\frac{\partial\varphi}{\partial x}\right) + 2\frac{\partial^2\varphi}{\partial t\partial x}\frac{\partial\varphi}{\partial x} \\ & + \frac{\gamma-1}{s}\frac{\partial\varphi}{\partial t}\frac{\partial}{\partial x}\left(s\frac{\partial\varphi}{\partial x}\right) + \frac{1}{3}\frac{\partial}{\partial x}\left(\frac{\partial\varphi}{\partial x}\right)^3 \\ & + \frac{\gamma-1}{2s}\left(\frac{\partial\varphi}{\partial x}\right)^2\frac{\partial}{\partial x}\left(s\frac{\partial\varphi}{\partial x}\right) - \frac{\delta}{s}\frac{\partial^2}{\partial t\partial x}\left(s\frac{\partial\varphi}{\partial x}\right) \end{aligned} \quad (2.25)$$

which is a one dimensional second order cubic partial differential equation with the only unknown variable being the velocity potential function $\varphi(x, t)$.

2.2.3 Dimensionless Variables

A set of dimensionless variables is defined as follows

$$X = \frac{x}{l}, \quad (2.26a)$$

$$T = t\omega, \quad (2.26b)$$

$$F = \frac{a}{l\omega_0^2}, \quad (2.26c)$$

$$\Phi = \frac{\varphi}{l^2\omega_0}, \quad (2.26d)$$

$$\Omega = \frac{\omega}{\omega_0}, \quad (2.26e)$$

$$D = \Omega \frac{\pi\delta\omega_0}{c_0^2}, \quad (2.26f)$$

$$\text{and } S = \frac{s}{l^2}. \quad (2.26g)$$

where ω_0 is a reference frequency chosen as the fundamental frequency of a cylindrical resonator of length l ; i.e.

$$\omega_0 = \pi \frac{c_0}{l} \quad (2.27)$$

It is also to be noticed that D is approximated to $D(\omega_0)$. The dimensionless variables defined in equations (2.26) are substituted in (2.25) to give the dimensionless form of the governing equation of the gas oscillating in the axisymmetric acoustic resonator

$$\begin{aligned}
& \frac{\partial^2 \Phi}{\partial T^2} - \frac{1}{\Omega^2 \pi^2} \left(\frac{1}{S} \frac{\partial S}{\partial X} \frac{\partial \Phi}{\partial X} + \frac{\partial^2 \Phi}{\partial X^2} \right) + \frac{2}{\Omega} \frac{\partial^2 \Phi}{\partial T \partial X} \frac{\partial \Phi}{\partial X} \\
& + \frac{\gamma - 1}{\Omega} \frac{\partial \Phi}{\partial T} \left(\frac{1}{S} \frac{\partial S}{\partial X} \frac{\partial \Phi}{\partial X} + \frac{\partial^2 \Phi}{\partial X^2} \right) - \frac{D}{\pi^3 \Omega} \left(\frac{1}{S} \frac{\partial S}{\partial X} \frac{\partial^2 \Phi}{\partial T \partial X} + \frac{\partial^3 \Phi}{\partial T \partial X^2} \right) \\
& + \frac{1}{3\Omega^2} \frac{\partial}{\partial X} \left(\frac{\partial \Phi}{\partial X} \right)^3 + \frac{\gamma - 1}{\Omega^2} \left(\frac{\partial \Phi}{\partial X} \right)^2 \left(\frac{1}{S} \frac{\partial S}{\partial X} \frac{\partial \Phi}{\partial X} + \frac{\partial^2 \Phi}{\partial X^2} \right) \\
& + \frac{F}{\Omega^2} \frac{\partial \Phi}{\partial X} - \frac{1}{\Omega} \frac{dF}{dT} X + \frac{\gamma - 1}{\Omega^2} F X \left(\frac{1}{S} \frac{\partial S}{\partial X} \frac{\partial \Phi}{\partial X} + \frac{\partial^2 \Phi}{\partial X^2} \right) = 0
\end{aligned} \tag{2.28}$$

2.2.4 Model Analysis

This section discusses solving the governing equation (2.28) by first using the linearized free oscillations together with the appropriate boundary conditions to extract the mode shapes which in turn can be used in the nonlinear model described in the previous section to find out the response of the acoustic resonator to external excitation.

Free Oscillations

The first step towards the solution is to find the natural modes of the free oscillations of the gas in the resonator which which satisfy the linearized wave equation

$$\frac{\partial^2 \Phi}{\partial T^2} - \frac{1}{\Omega^2 \pi^2} \left(\frac{1}{S} \frac{\partial S}{\partial X} \frac{\partial \Phi}{\partial X} + \frac{\partial^2 \Phi}{\partial X^2} \right) = 0 \tag{2.29}$$

The velocity potential $\Phi(X, T)$ is assumed to consist of two independent functions;

a space-dependent function $\Psi(X)$ and a time-dependent one $\eta(T)$

$$\Phi(X, T) = \eta(T) \Psi(X) \quad (2.30)$$

Equation (2.30) is substituted in the wave equation (2.29) and the variables are separated from each other

$$\frac{\Omega^2 \pi^2}{\eta} \frac{d^2 \eta}{dT^2} = \frac{1}{\Psi} \left[\left(\frac{1}{S} \frac{dS}{dX} \right) \frac{d\Psi}{dX} + \frac{d^2 \Psi}{dX^2} \right] = -k^2 \quad (2.31)$$

where $k = 1, 2, 3, \dots$ is the wave number. From equation (2.31) one can get the temporal problem

$$\frac{d^2 \eta}{dT^2} + \frac{k^2}{\Omega^2 \pi^2} \eta = 0 \quad (2.32)$$

and the spatial one

$$S \frac{d^2 \Psi}{dX^2} + \frac{dS}{dX} \frac{d\Psi}{dX} + k^2 S \Psi = 0 \quad (2.33)$$

The natural modes are all the functions $\Psi_k(X)$ that satisfy equation (2.33) for different values of k as well as the boundary conditions which will be mentioned later. It is obvious that the mode shapes are explicitly dependent on the geometry of the resonator.

Boundary Conditions

Boundary conditions are needed along with equation (2.33) to determine the mode shapes of the acoustic resonator. For the case of an entirely driven resonator closed from both sides with no flow at the boundaries the velocity is zero at both sides where

the coordinate system attached to the resonator.

$$u(0, t) = 0, \tag{2.34a}$$

$$\text{and } u(l, t) = 0. \tag{2.34b}$$

In terms of the velocity potential function defined in (2.10) the boundary conditions are

$$\frac{\partial \varphi(0, t)}{\partial x} = 0, \tag{2.35a}$$

$$\text{and } \frac{\partial \varphi(l, t)}{\partial x} = 0. \tag{2.35b}$$

and in terms of the dimensionless variables defined in (2.26d)

$$\frac{\partial \Phi(0, T)}{\partial X} = 0, \tag{2.36a}$$

$$\text{and } \frac{\partial \Phi(1, T)}{\partial X} = 0. \tag{2.36b}$$

Separating variables as in equation (2.30) and observing the time-independence of the boundary conditions one can easily deduce

$$\frac{\partial \Psi(0)}{\partial X} = 0, \tag{2.37a}$$

$$\text{and } \frac{\partial \Psi(1)}{\partial X} = 0. \tag{2.37b}$$

Forced Oscillations

The next step in solving equation (2.28) is to assume that the solution function $\Phi(X, T)$ consists of the summation of all possible spatial modes $\Psi_1, \Psi_2, \dots, \Psi_\infty$,

weighted by corresponding time dependant functions $\eta_1, \eta_2, \dots, \eta_\infty$

$$\Phi(X, T) = \sum_{n=1}^{\infty} \eta_n(T) \Psi_n(X) \quad (2.38)$$

The solution can be approximated by the first N modes

$$\Phi(X, T) \simeq \eta_n(T) \Psi_n(X) \quad (2.39)$$

Index notation, in which an index n takes all possible values in its range $1, 2, \dots, 3$ and a repeated index implies summation, is used from now on.

Equation (2.39) is substituted in the governing equation (2.28). However, the approximate Φ will yield a residual $R(\Phi(X, T))$ rather than a typical zero due to the approximation

$$\begin{aligned} R(\Phi(X, T)) &= \frac{\partial^2 \Phi}{\partial T^2} - \frac{1}{\Omega^2 \pi^2} \left(\frac{1}{S} \frac{\partial S}{\partial X} \frac{\partial \Phi}{\partial X} + \frac{\partial^2 \Phi}{\partial X^2} \right) + \frac{2}{\Omega} \frac{\partial^2 \Phi}{\partial T \partial X} \frac{\partial \Phi}{\partial X} \\ &+ \frac{\gamma - 1}{\Omega} \frac{\partial \Phi}{\partial T} \left(\frac{1}{S} \frac{\partial S}{\partial X} \frac{\partial \Phi}{\partial X} + \frac{\partial^2 \Phi}{\partial X^2} \right) - \frac{D}{\pi^3 \Omega} \left(\frac{1}{S} \frac{\partial S}{\partial X} \frac{\partial^2 \Phi}{\partial T \partial X} + \frac{\partial^3 \Phi}{\partial T \partial X^2} \right) \\ &+ \frac{1}{3\Omega^2} \frac{\partial}{\partial X} \left(\frac{\partial \Phi}{\partial X} \right)^3 + \frac{\gamma - 1}{\Omega^2} \left(\frac{\partial \Phi}{\partial X} \right)^2 \left(\frac{1}{S} \frac{\partial S}{\partial X} \frac{\partial \Phi}{\partial X} + \frac{\partial^2 \Phi}{\partial X^2} \right) + \frac{F}{\Omega^2} \frac{\partial \Phi}{\partial X} \\ &- \frac{1}{\Omega} \frac{dF}{dT} X + \frac{\gamma - 1}{\Omega^2} F X \left(\frac{1}{S} \frac{\partial S}{\partial X} \frac{\partial \Phi}{\partial X} + \frac{\partial^2 \Phi}{\partial X^2} \right) \end{aligned} \quad (2.40)$$

Assuming the mode shapes $\Psi(X)$ are known, the weighted residual form can allow us to solve for the n time dependant functions $\eta_n(T)$ by constructing a system of n equations

$$\int_0^1 R(\Phi(X, T)) \cdot W_j(X) dX = 0 \quad (2.41)$$

where $W_j(X)$ are n linearly independent admissible weight functions.

Equation (2.40) is substituted in equation (2.41) with $\Phi(X, T)$ being substituted by the approximation in (2.39) to give

$$\begin{aligned}
& \int_0^1 W_j \Psi_n \frac{d^2 \eta_m}{dT^2} dX - \frac{1}{\Omega^2 \pi^2} \int_0^1 W_j \left(\frac{1}{S} \frac{dS}{dX} \frac{d\Psi_n}{dX} + \frac{d^2 \Psi_n}{dX^2} \right) \eta_m dX \\
& + \int_0^1 W_j \left[\frac{2}{\Omega} \frac{d\Psi_n}{dX} \frac{d\Psi_m}{dX} + \frac{\gamma - 1}{\Omega} \left(\frac{1}{S} \frac{\partial S}{\partial X} \frac{d\Psi_m}{dX} + \frac{d^2 \Psi_m}{dX^2} \right) \Psi_n \right] \frac{d\eta_n}{dT} \eta_m dX \\
& - \frac{D}{\pi^3 \Omega} \int_0^1 W_j \left(\frac{1}{S} \frac{dS}{dX} \frac{d\Psi_n}{dX} + \frac{d^2 \Psi_n}{dX^2} \right) \frac{d\eta_n}{dT} dX \\
& + \frac{1}{3\Omega^2} \int_0^1 W_j \frac{d}{dX} \left(\frac{d\Psi_n}{dX} \frac{d\Psi_m}{dX} \frac{d\Psi_p}{dX} \right) \eta_n \eta_m \eta_p dX \\
& + \frac{\gamma - 1}{2\Omega^2} \int_0^1 W_j \frac{d\Psi_n}{dX} \frac{d\Psi_m}{dX} \left(\frac{1}{S} \frac{dS}{dX} \frac{d\Psi_p}{dX} + \frac{d^2 \Psi_p}{dX^2} \right) \eta_n \eta_m \eta_p dX \\
& = -\frac{F}{\Omega^2} \int_0^1 W_j \frac{d\Psi_n}{dX} \eta_m dX - \frac{\gamma - 1}{\Omega^2} F \int_0^1 W_j \left(\frac{1}{S} \frac{dS}{dX} \frac{d\Psi_n}{dX} + \frac{d^2 \Psi_n}{dX^2} \right) \eta_n X dX \\
& + \frac{1}{\Omega} \frac{dF}{dT} \int_0^1 X W_j dX
\end{aligned} \tag{2.42}$$

where the indices j, n, m , and p all take the values of $1, 2, \dots, N$.

Equation (2.42) can be assembled in a compact form as follows

$$A_{jn} \frac{d^2 \eta_n}{dT^2} + B_{jn} \eta_n + C_{jnm} \frac{d\eta_m}{dT} \eta_m + D_{jn} \frac{d\eta_n}{dT} + E_{jnmp} \eta_n \eta_m \eta_p = F_j \tag{2.43}$$

where

$$A_{jn} = \int_0^1 W_j \Psi_n dX, \quad (2.44a)$$

$$B_{jn} = -\frac{1}{\Omega^2 \pi^2} \int_0^1 W_j \left(\frac{1}{S} \frac{dS}{dX} \frac{d\Psi_n}{dX} + \frac{d^2 \Psi_n}{dX^2} \right) dX + \frac{F}{\Omega^2} \int_0^1 W_j \frac{d\Psi_n}{dX} dX \\ + \frac{\gamma - 1}{\Omega^2} F \int_0^1 W_j \left(\frac{1}{S} \frac{dS}{dX} \frac{d\Psi_n}{dX} + \frac{d^2 \Psi_n}{dX^2} \right) X dX, \quad (2.44b)$$

$$C_{jnm} = \frac{2}{\Omega} \int_0^1 W_j \frac{d\Psi_n}{dX} \frac{d\Psi_m}{dX} dX \\ + \frac{\gamma - 1}{\Omega} \int_0^1 W_j \left[\Psi_n \frac{d^2 \Psi_m}{dX^2} + \left(\frac{1}{S} \frac{\partial S}{\partial X} \right) \Psi_n \frac{d\Psi_m}{dX} \right] dX, \quad (2.44c)$$

$$D_{jn} = -\frac{D}{\pi^3 \Omega} \int_0^1 W_j \left(\frac{1}{S} \frac{dS}{dX} \frac{d\Psi_n}{dX} + \frac{d^2 \Psi_n}{dX^2} \right) dX, \quad (2.44d)$$

$$E_{jnm} = \frac{1}{3\Omega^2} \int_0^1 W_j \frac{d}{dX} \left(\frac{d\Psi_n}{dX} \frac{d\Psi_m}{dX} \frac{d\Psi_p}{dX} \right) dX \\ + \frac{\gamma - 1}{2\Omega^2} \int_0^1 W_j \frac{d\Psi_n}{dX} \frac{d\Psi_m}{dX} \left(\frac{1}{S} \frac{dS}{dX} \frac{d\Psi_p}{dX} + \frac{d^2 \Psi_p}{dX^2} \right) dX, \quad (2.44e)$$

$$\text{and } F_j = \frac{1}{\Omega} \frac{dF}{dT} \int_0^1 X W_j dX. \quad (2.44f)$$

$\Psi_n(X)$ are selected as the first N spatial mode shapes of the dimensionless velocity potential function for the gas oscillating in the resonator. Hence, equation (2.43) represents a system of N cubic, second order ordinary differential equations in the N unknown functions $\eta_n(T)$. In order to solve them, the weight functions $W_j(X)$ need to be selected

$$W_j(X) = S(X) \Psi_j(X) \quad (2.45)$$

The reason for this choice will be clarified later on in the Finite Element Model.

Initial Conditions

For an entirely driven acoustic resonator that is undergoing harmonic oscillations which can be characterized by $a(t) = a_0 \cos(\omega t)$ and since x is attached to the cavity, the initial conditions can be easily evaluated as follows

$$\frac{\partial u}{\partial t}(x, 0) = a_0 \cos(\omega t) |_{t=0} = a_0, \quad (2.46a)$$

$$\text{and } u(x, 0) = \frac{a_0}{\omega} \sin(\omega t) |_{t=0} = 0. \quad (2.46b)$$

Using the velocity potential function in equation (2.10), the initial conditions take the form

$$\frac{\partial}{\partial t} \left(\frac{\partial \varphi}{\partial x}(x, 0) \right) = a_0, \quad (2.47a)$$

$$\text{and } \frac{\partial \varphi}{\partial x}(x, 0) = 0. \quad (2.47b)$$

and using the dimensionless variables in equation (2.26) and the separation of variables in(2.39), one gets

$$\frac{d\Psi_n(X)}{dX} \frac{d\eta_n(0)}{dT} = F_0, \quad (2.48a)$$

$$\text{and } \frac{d\Psi_n(X)}{dX} \eta_n(0) = 0. \quad (2.48b)$$

If the cavity is excited at the k^{th} natural frequencies

$$\frac{d\Psi_n(X)}{dX} \frac{d\eta_n(0)}{dT} = \begin{cases} F_0 \dots n = k \\ 0 \dots n \neq k \end{cases}, \quad (2.49a)$$

$$\text{and } \eta_n(0) = 0. \quad (2.49b)$$

Equations (2.49) represent the $2N$ initial conditions just needed to solve the N second order ordinary differential equations (2.43)

2.2.5 Solution and Post Processing

Once the initial conditions are known and the basis and weight functions are selected, equation (2.43) can be solved numerically. A Runge-Kutta integration scheme can be used. The time-dependent coefficients are substituted into equation (2.39) to determine the approximate dimensionless velocity potential function, from which all other variables of interest and can be calculated. In this study, the measure of performance of an acoustic resonator is the pressure ratio. Hence, one needs to find a direct relation between the pressure ratio and the dimensionless velocity potential function. Equation (2.10) is substituted in equation (2.12) giving

$$\frac{\partial \varphi}{\partial t} + \frac{1}{2} \left(\frac{\partial \varphi}{\partial x} \right)^2 = -\frac{\gamma p_0}{(\gamma - 1) \rho_0^\gamma} \rho^{\gamma-1} - a(t)x + \frac{\delta}{s} \frac{\partial}{\partial x} \left(s \frac{\partial \varphi}{\partial x} \right) + \frac{c_0^2}{\gamma - 1} \quad (2.50)$$

and from equation (2.13) one can get

$$c_0 = c(\rho_0) = \frac{\gamma p_0}{\rho_0} \quad (2.51)$$

which can be substituted in (2.50) to give

$$\frac{\partial\varphi}{\partial t} + \frac{1}{2} \left(\frac{\partial\varphi}{\partial x} \right)^2 = -a(t)x + \frac{\delta}{s} \frac{\partial}{\partial x} \left(s \frac{\partial\varphi}{\partial x} \right) + \frac{c_0^2}{\gamma - 1} \left[1 - \left(\frac{\rho}{\rho_0} \right)^{\gamma-1} \right] \quad (2.52)$$

which in turn can be manipulated to find the density ratio

$$\frac{\rho}{\rho_0} = \left\{ 1 - \frac{\gamma - 1}{c_0^2} \left[\frac{\partial\varphi}{\partial t} + \frac{1}{2} \left(\frac{\partial\varphi}{\partial x} \right)^2 + a(t)x - \frac{\delta}{s} \frac{\partial}{\partial x} \left(s \frac{\partial\varphi}{\partial x} \right) \right] \right\}^{1/\gamma - 1} \quad (2.53)$$

The state equation (2.8) is used together with the last equation to determine the pressure ratio

$$\frac{p}{p_0} = \left\{ 1 - \frac{\gamma - 1}{c_0^2} \left[\frac{\partial\varphi}{\partial t} + \frac{1}{2} \left(\frac{\partial\varphi}{\partial x} \right)^2 + a(t)x - \frac{\delta}{s} \frac{\partial}{\partial x} \left(s \frac{\partial\varphi}{\partial x} \right) \right] \right\}^{\gamma/\gamma - 1} \quad (2.54)$$

The dimensionless variables defined in equation (2.26) can now be substituted to give

$$\frac{P}{P_0} = \left[1 - (\gamma - 1) \pi^2 \left(\Omega \frac{\partial\Phi}{\partial T} + \frac{1}{2} \left(\frac{\partial\Phi}{\partial X} \right)^2 + FX - \frac{D}{\pi^3 S} \frac{\partial}{\partial X} \left(S \frac{\partial\Phi}{\partial X} \right) \right) \right]^{\gamma/(\gamma - 1)} \quad (2.55)$$

The term which includes the damping can be expanded to

$$\frac{D}{\pi^3 S} \frac{\partial}{\partial X} \left(S \frac{\partial\Phi}{\partial X} \right) = \frac{D}{\pi^3} \left(\frac{\partial S}{\partial X} \frac{\partial\Phi}{\partial X} + \frac{\partial^2\Phi}{\partial X^2} \right) \quad (2.56)$$

where the first term of the right hand side should vanish at the boundaries of a closed resonator. Therefore the pressure ratio at the ends of an acoustic resonator can be calculated as

$$\frac{P}{P_0} = \left[1 - (\gamma - 1) \pi^2 \left(\Omega \frac{\partial\Phi}{\partial T} + \frac{1}{2} \left(\frac{\partial\Phi}{\partial X} \right)^2 + FX - \frac{D}{\pi^3} \frac{\partial^2\Phi}{\partial X^2} \right) \right]^{\gamma/(\gamma - 1)} \quad (2.57)$$

2.3 Application of the Model

In this section, the theoretical model that has been developed in the previous section will be evaluated by applying it to resonators which have simple geometries and hence their mode shapes can be determined. The model will be first applied to cylindrical resonators which can be considered as a benchmark problem for the study of acoustic resonators. The prediction of the performance of cylindrical resonators aim on one hand at demonstrating the accuracy of the model by being able to capture the dynamics of the system and on the other hand at emphasizing the drawbacks of using cylindrical (and more generally consonant) resonators. Then the model will be used to simulate the dynamics of exponential horn-shaped resonators as an example of dissonant geometries showing how much gain can be achieved in the performance. Finally, linearly varying area resonators will be discussed, their mode shapes will be extracted and its performance is predicted by the model to be compared to other geometries.

2.3.1 Cylindrical Resonators

Cylindrical resonators are characterized by a constant cross-sectional area,

$$S(X) = S_0 \tag{2.58}$$

and hence its derivative is zero. Therefore equation (2.33) yields

$$\frac{d^2\Psi}{dX^2} + k^2 S\Psi = 0 \tag{2.59}$$

with the boundary conditions as in equations (2.37). Therefore, the mode shapes of a cylindrical resonator closed from both ends are

$$\Psi_n(X) = \cos(n\pi X) \quad (2.60)$$

Substituting the basis functions in equation (2.60) and weight functions in equation (2.45) into equation (2.43) one can solve for the time-dependant coefficients η_n , then for the dimensionless velocity potential function Φ from equation (2.39) and finally for the pressure ratio from equation (2.57).

Figure 2.1 shows the pressure ratio predicted at one end ($X = 0$) of the cylindrical resonator excited at different ratios of its fundamental natural frequency ($\Omega = 0.9, 0.95, 0.98, 1, 1.02, 1.05$) at an acceleration of 100g. These results were obtained by assuming $D = 0.01$, $l = 0.165$ m, $c = 330$ m/s, with the first 20 mode shapes considered ($N = 20$). The figure shows that away from the natural frequency of the resonator, the response of the pressure is almost smooth and sinusoidal. As the excitation approaches the natural frequency of the resonator, the pressure ratio increases but other harmonics become apparent and the pressure wave gets distorted. At $\Omega = 1$, it looks like a saw tooth wave which has abrupt changes called periodic shocks. These shocks have been reported experimentally by many researchers as in Saenger and Hudson [10]. The results perfectly match those of Ilinskii *et al.* [23] and Erickson and Zinn [25].

Figure 2.2 shows the pressure ratio predicted at one end ($X = 0$) of the same cylindrical resonator excited at its fundamental frequency ($\Omega = 1$) with different

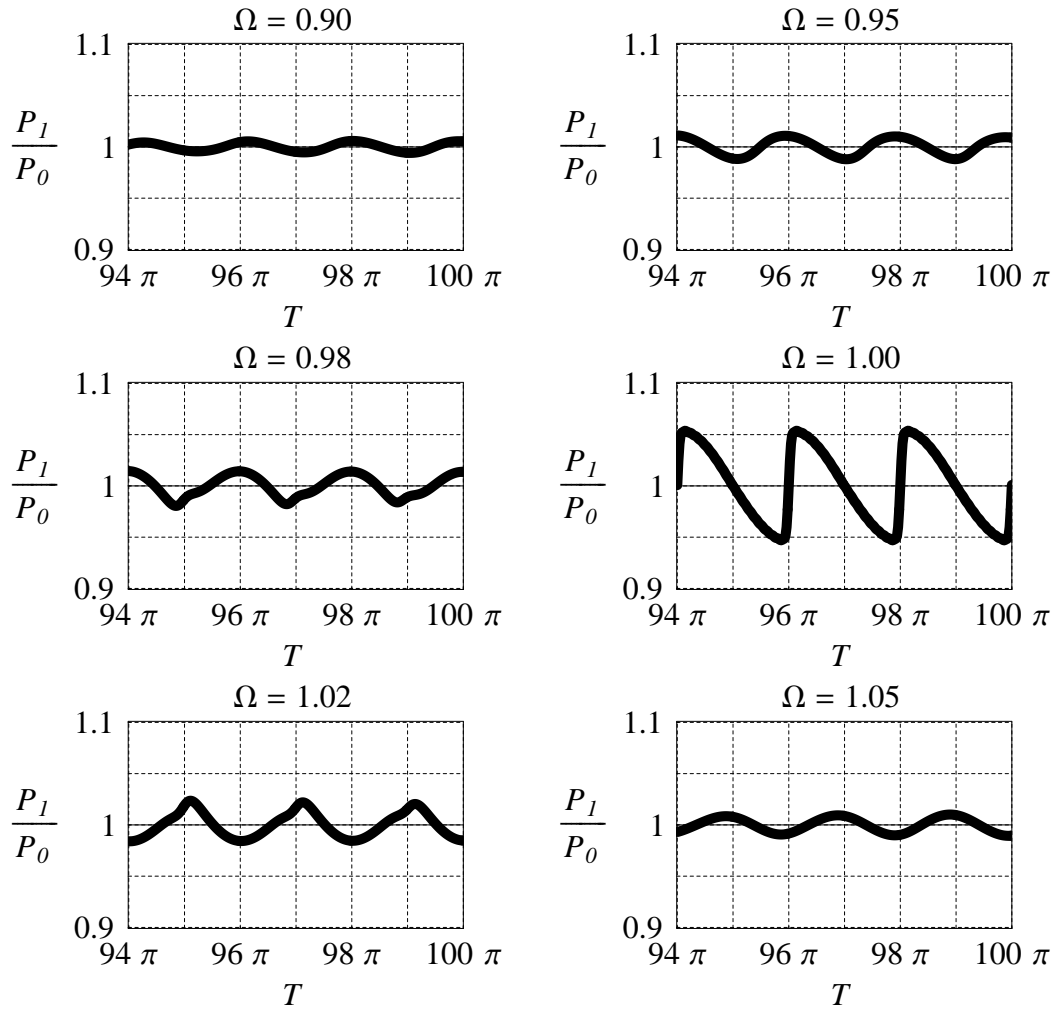


Figure 2.1: Pressure ratio predicted at one end of a cylindrical resonator excited at different frequencies $\Omega = (0.9, 0.95, 0.98, 1, 1.02, 1.05)$, with an amplitude $a_0 = 100g$. ($D = 0.01$, $l = 0.165$ m, $c_0 = 330$ m/s, $\gamma = 1.2$, $N = 20$).

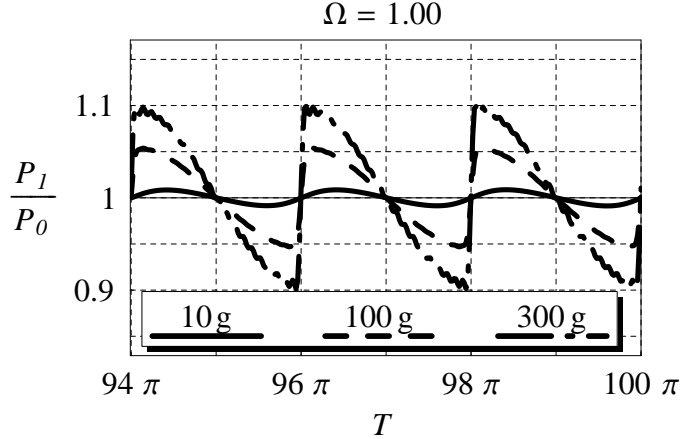


Figure 2.2: **Pressure ratio predicted at one end of a cylindrical resonator excited at $\Omega = 1$ with different acceleration amplitudes $a_0 = \{10, 100, 300\}$ g.** ($D = 0.01$, $l = 0.165$ m, $c_0 = 330$ m/s, $\gamma = 1.2$, $N = 20$).

acceleration amplitudes ($a_0 = \{10, 100, 300\}$)g. The figure indicates that as the amplitude increases, the pressure ratio increases and gets skewed until periodic shock waves are formed. Other than the periodic shocks, there also appears some micro shocks. The limit on pressure ratio in a shock free cylindrical resonator is less than 1.1. The formation of the shock waves in resonators is undesirable as it sets a limit on the maximum pressure ratio developed in this resonator. Most of the increase in the input energy after the formation of the shock waves will be lost in the form of heat.

In order to show the effect of damping Figure 2.3 shows the pressure ratio predicted at $X = 0$ of the same cylindrical resonator excited again at its fundamental frequency ($\Omega = 1$) with different acceleration amplitudes ($a_0 = \{10, 100, 300\}$)g, with D chosen as 0.04. It is clear from the figure that the higher damping definitely yields lower

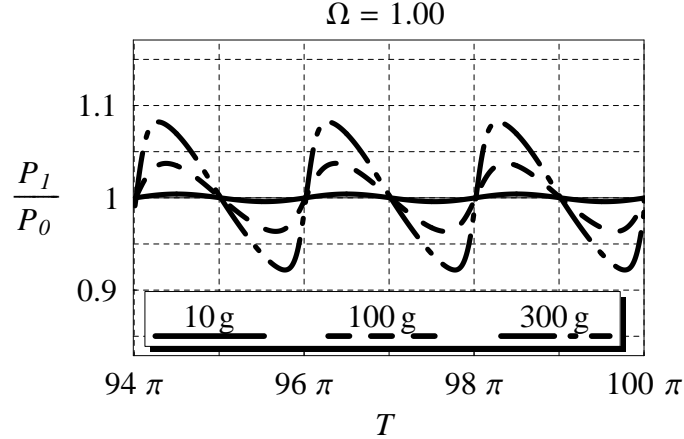


Figure 2.3: **Pressure ratio predicted at one end of a cylindrical resonator excited at $\Omega = 1$ with different acceleration amplitudes $a_0 = \{10, 100, 300\}g$.** ($D = 0.04$, $l = 0.165$ m, $c_0 = 330$ m/s, $\gamma = 1.2$, $N = 20$).

pressure ratio. At the same time, one can see that at low excitation levels, the damping effect appears in the form of reduction in pressure, while at higher levels the nonlinearities in the equation is what majorally determines the pressure ratios rather than the damping.

Figure 2.4 shows the pressure ratio predicted at different locations of the cylindrical resonator. It is noticed from the figure that each two locations symmetric about $X = 0.5$ have similar pressure waves that are 180° out of phase and also the odd mode shapes diminish as one approaches the middle of the tube.

In order to understand the underlying phenomena occurring in the resonator, we restrict our attention to two modes only. First, equation (2.43) is solved for η_1 and η_2 , when the resonator is excited at $\Omega = 1$ at a small acceleration of 1g.

Figure 2.5 shows the evolution of η_1 and η_2 with time. It is shown that the am-

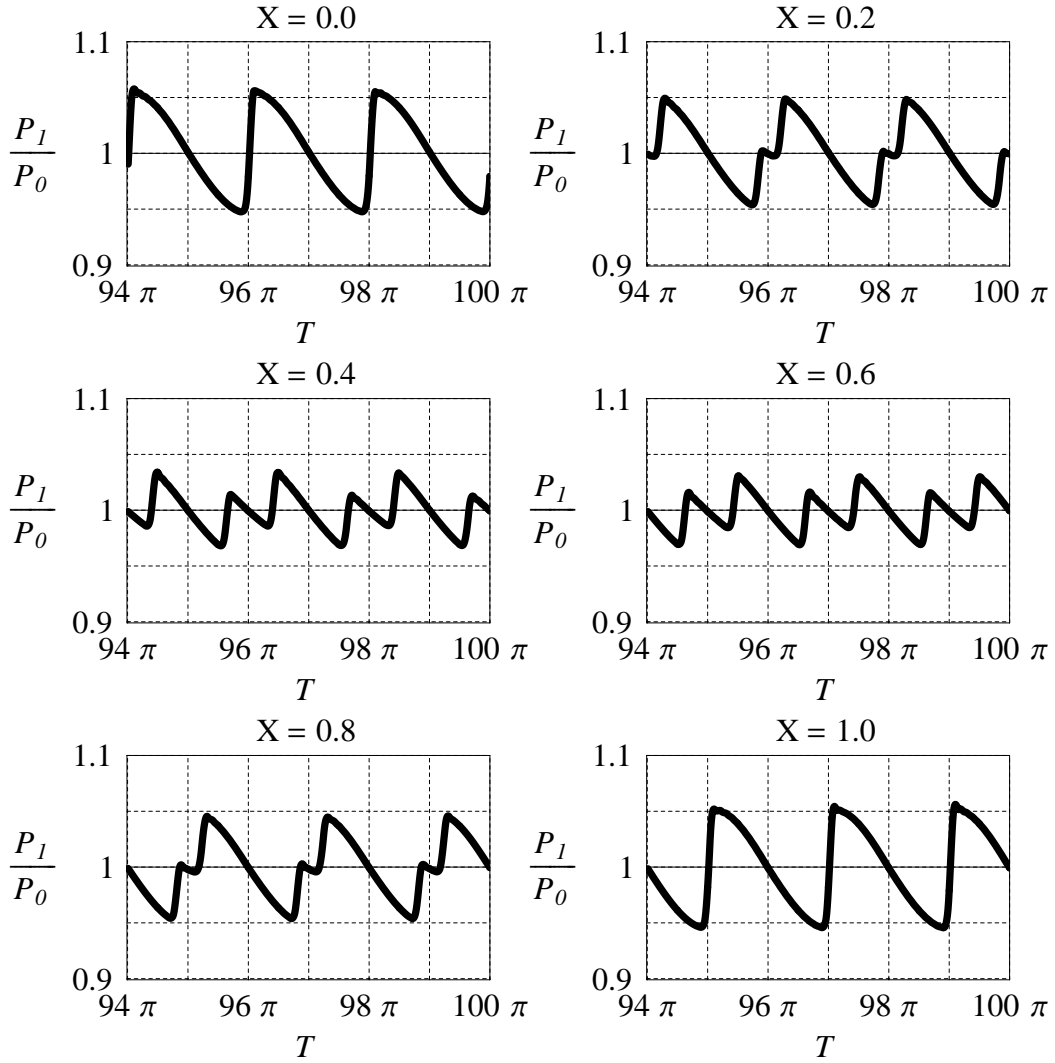


Figure 2.4: **Pressure ratio predicted at different locations of a cylindrical resonator ($X = \{0.0, 0.2, 0.4, 0.6, 0.8, 1.0\}$, excited at $\Omega = 1, a_0 = 100g$. ($D = 0.01, l = 0.165$ m, $c_0 = 330$ m/s, $\gamma = 1.2, N = 20$).**

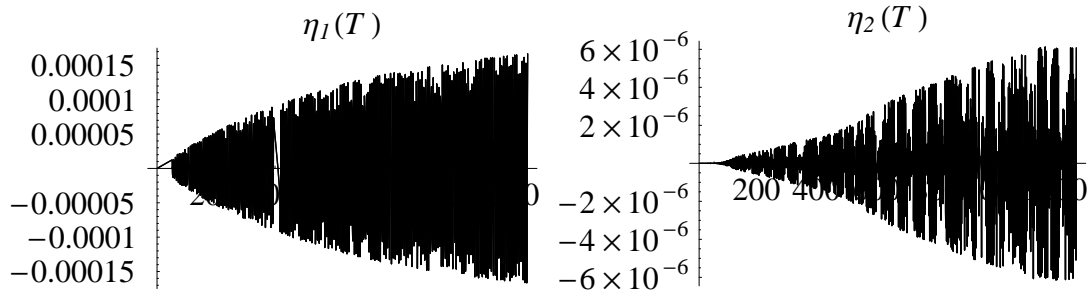


Figure 2.5: **Evolution of the time dependent coefficients $\eta_1(T)$ and $\eta_2(T)$ at 1g in a cylindrical cavity excited at $\Omega = 1$. ($D = 0.01$, $l = 0.165$ m, $c_0 = 330$ m/s, $\gamma = 1.2$, $N = 2$).**

plitude of η_2 is almost two orders of magnitude less than that of η_1 , so the pressure wave shown in Figure 2.6 is mainly dominated by the first mode and looks smooth.

On the other hand, when the excitation amplitude is increased to 100g, the amplitudes of the modes η_1 and η_2 look as shown in Figure 2.7.

It is obvious the amplitude of η_2 has increased to almost 50% of that of η_1 , and so both modes are well manifested in the pressure wave shown in Figure 2.8.

In general, when the excitation amplitude increases from small to large accelerations, the first mode of the acoustic cavity gets saturated with energy and tends to pass some of it to the higher-modes. This passing of energy is very easy in the case of consonant cavities. The combination of working modes, their amplitudes and phases is what determines the final form of the pressure wave. Periodic shock wave is just one special case of all possible combinations. This passing of energy from the lower mode to the higher ones, can only be captured within a nonlinear model because

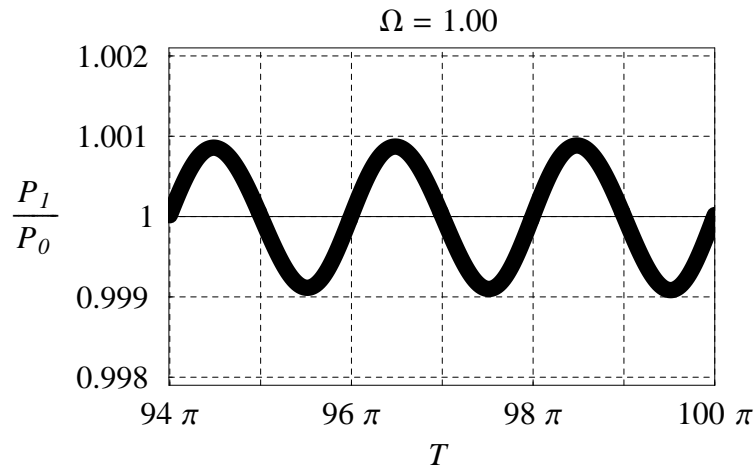


Figure 2.6: **Pressure ratio at 1g in a cylindrical cavity excited at $\Omega = 1$.**
 ($D = 0.01$, $l = 0.165$ m, $c = 330$ m/s, $\gamma = 1.2$, $N = 2$).

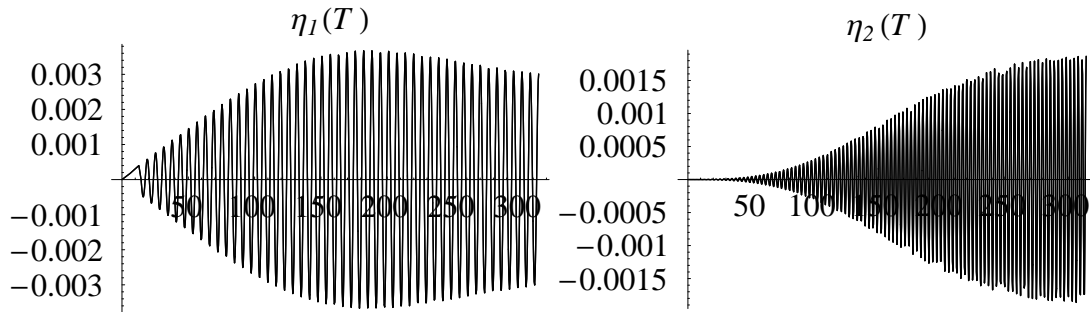


Figure 2.7: **Evolution of the time dependent coefficients $\eta_1(T)$ and $\eta_2(T)$ at 100g in a cylindrical cavity excited at $\Omega = 1$.**
 ($D = 0.01$, $l = 0.165$ m, $c_0 = 330$ m/s, $\gamma = 1.2$, $N = 2$).

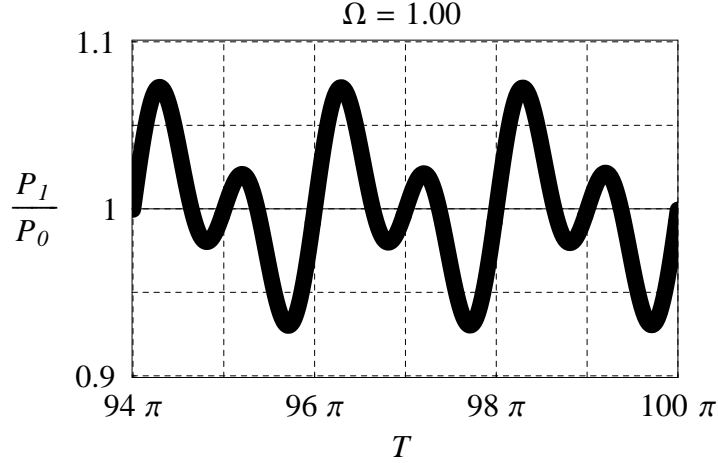


Figure 2.8: **Pressure ratio at 100g in a cylindrical cavity excited at $\Omega = 1$.**
($D = 0.01$, $l = 0.165$ m, $c_0 = 330$ m/s, $\gamma = 1.2$, $N = 2$).

of the presence of the terms including C_{jnm} and E_{jnmp} in equation (2.43). A linear model given by equation (1.4), will always fail to capture these phenomena and will always predict the pressure amplitude to be proportional to the excitation amplitude.

2.3.2 Exponential Resonator

These resonators are characterized by a cross sectional area that changes exponentially along the axis of the resonator

$$S(X) = S_0 \exp^{\alpha X} \quad (2.61)$$

where α is called the flare constant. Therefore,

$$\frac{1}{S} \frac{dS}{dX} = \alpha \quad (2.62)$$

Equation (2.62) is substituted in equation (2.31) to give

$$\frac{\Omega^2 \pi^2}{\eta} \frac{d^2 \eta}{dT^2} = \frac{1}{\Psi} \left[(\alpha) \frac{d\Psi}{dX} + \frac{d^2 \Psi}{dX^2} \right] = -k^2 \quad (2.63)$$

Equation (2.63) with the boundary conditions in equation (2.37) will yield the eigenvalues

$$k_n^2 = \left(\frac{\omega_n}{c_0} \right)^2 = \left(\frac{n\pi}{l} \right)^2 + \frac{1}{4} \left(\frac{\alpha}{l} \right)^2 \quad (2.64)$$

and the eigenfunctions

$$\Psi_n(X) = \exp^{-\left(\frac{\alpha X}{2}\right)} \left(\cos(n\pi X) + \frac{\alpha}{2n\pi} \sin(n\pi X) \right) \quad (2.65)$$

where $n = 1, 2, 3, \dots$

The mode shapes in equation (2.65) are substituted in equation (2.43) together with the weight functions in equation (2.45) to solve for the time-dependant coefficients η_n , then for the dimensionless velocity potential function Φ in equation (2.39) and finally for the pressure ratio from equation (2.57). As an example, the following assumptions are made; $l = 0.224$ m, $D = 0.01$, $c_0 = 330$ m/s, $\alpha = 5.75$ which was considered by Erickson and Zinn [25] through several trials as an optimal value for the flare constant. From equations (2.26) and (2.64) the dimensionless frequency takes the form

$$\Omega_n = \frac{\omega_n}{\omega_0} = \sqrt{1 + \frac{1}{4} \frac{\alpha^2}{n^2 \pi^2}} \quad (2.66)$$

from which the fundamental dimensionless natural frequency for $\alpha = 5.75$ is $\Omega = 1.356$.

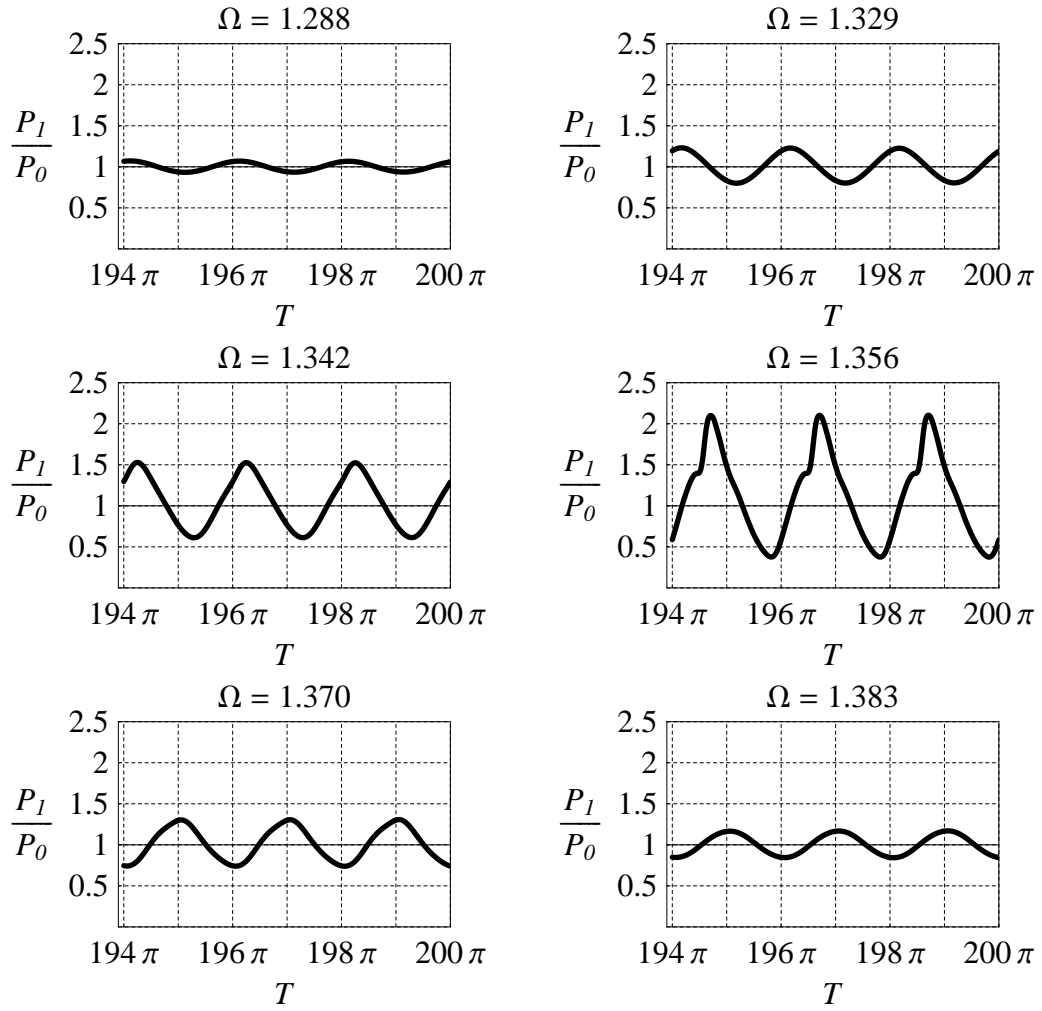


Figure 2.9: **Pressure ratio predicted at the small end of an exponential resonator ($\alpha = 5.75$) excited at different frequencies $\Omega = \{1.288, 1.329, 1.342, 1.356, 1.370, 1.383\}$ with an amplitude of $a_0 = 250\text{g}$. ($D = 0.01$, $l = 0.224$ m, $c_0 = 330$ m/s, $\gamma = 1.2$, $N = 5$).**

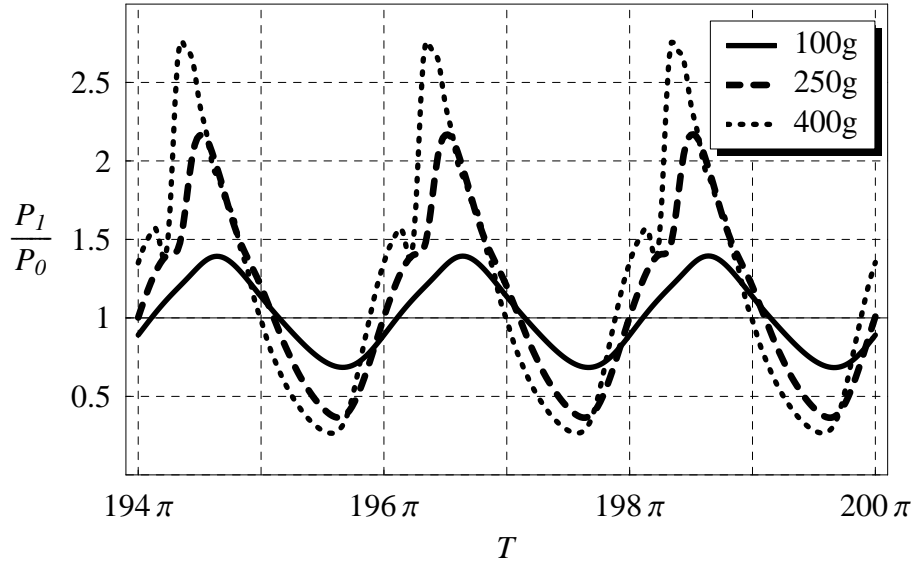


Figure 2.10: **Pressure ratio predicted at the small end of an exponential resonator ($\alpha = 5.75$) excited at $\Omega = 1$ with different amplitudes $a_0 = 100g, 250g, 400g$. ($D = 0.01$, $l = 0.224$ m, $c_0 = 330$ m/s, $\gamma = 1.2$, $N = 20$.)**

Figure 2.9 shows the pressure ratio predicted at the small end ($X = 0$) of the resonator excited at different ratios (0.95, 0.98, 0.99, 1, 1.01, 1.02) of its fundamental natural frequency. These ratios correspond to $\Omega = 1.288, 1.329, 1.342, 1.356, 1.370, 1.383$. The pressure ratios are predicted for an acceleration of 250 g. The first 5 mode shapes were considered. Again, the figure shows that away from the natural frequency of the resonator, the response of the pressure is almost smooth and sinusoidal but still small. At the natural frequency of the cavity ($\Omega = 1.356$) the pressure ratio increases and other harmonics become excited making the pressure wave distorted. Interestingly, pressure ratios up to 2.2 are achieved by this cavity. This far exceeds the ratios obtained from cylindrical resonators.

Figure 2.10 shows the pressure ratio predicted at the small end ($X = 0$) of the

same exponential resonator at different accelerations ($a_0 = 100g, 250g, 400g$). As shown in Figure 2.10, the pressure ratio increases with the increase of the excitation amplitude up to almost 250 g, and the pressure ratio at this stage is more than two. At 400 g, periodic and micro shocks are evident. Recall from Figure 2.2 that the shock waves in cylindrical resonators started occurring at accelerations less than 100 g and the pressure ratio at this frequency was about 1.05. So, the exponential resonator emphasizes the advantage of using dissonant cavities is twofold; they delay the passing of energy to higher-order modes and help to make use of the available combination of modes in a constructive way rather than a destructive one.

2.3.3 Linearly Varying Area Resonators

The cross sectional area (*area not radius*) of a linearly-varying area geometry as a function in the axial position x is shown in Figure 2.11. It can be characterized by

$$S(X) = S_0 + (S_1 - S_0) X \quad (2.67)$$

Therefore,

$$\begin{aligned} \frac{1}{S} \frac{dS}{dX} &= \frac{S_1 - S_0}{S_0 + (S_1 - S_0) X} \\ &= \frac{1}{\beta + X} \end{aligned} \quad (2.68)$$

where β denotes the linearly varying area parameter and is defined as

$$\beta = \frac{S_0}{S_1 - S_0} \quad (2.69)$$

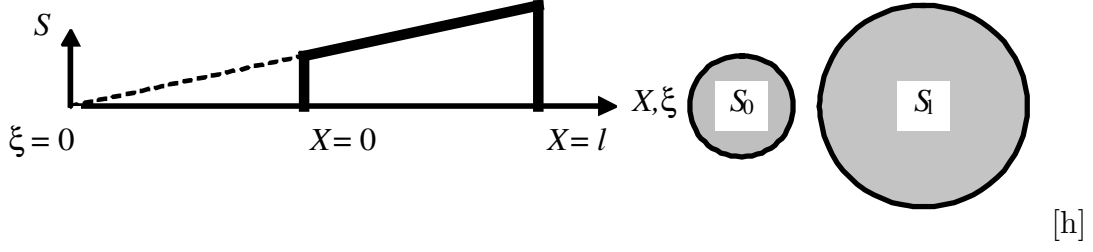


Figure 2.11: Geometry of a linearly varying area resonator.

Therefore, equation (2.31) for a linearly varying area resonator becomes

$$\frac{\Omega^2 \pi^2}{\eta} \frac{d^2 \eta}{dT^2} = \frac{1}{\Psi} \left[\left(\frac{1}{\beta + X} \right) \frac{d\Psi}{dX} + \frac{d^2 \Psi}{dX^2} \right] = -k^2 \quad (2.70)$$

from which the temporal problem is

$$\frac{d^2 \eta}{dT^2} + \frac{k^2}{\Omega^2 \pi^2} \eta = 0 \quad (2.71)$$

and the spatial one is

$$\frac{d^2 \Psi}{dX^2} + \frac{1}{\beta + X} \frac{d\Psi}{dX} + k^2 \Psi = 0 \quad (2.72)$$

In order to solve this differential equation (2.72), it is convenient to perform a coordinate transformation by using the new coordinate $\xi = X + \beta$ which is also shown in Figure 2.11 to reduce the above equation into

$$\frac{d^2 \Psi}{d\xi^2} + \frac{1}{\xi} \frac{d\Psi}{d\xi} + k^2 \Psi = 0 \quad (2.73)$$

Equation (2.73) is nothing but a Bessel equation of order zero whose solution according to Boyce [26] is

$$\Psi(\xi) = c_1 J_0(k\xi) + c_2 Y_0(k\xi) \quad (2.74)$$

and whose derivative is

$$\frac{d\Psi}{d\xi} = -k [c_1 J_1(k\xi) + c_2 Y_1(k\xi)] \quad (2.75)$$

In terms of the new coordinate ξ , the boundary conditions in equation (2.37) become

$$\frac{\partial\Psi(\beta)}{\partial\xi} = 0, \quad (2.76a)$$

$$\text{and } \frac{\partial\Psi(\beta+1)}{\partial\xi} = 0 \quad (2.76b)$$

The first boundary condition in equation (2.76a) is substituted in equation (2.75) to give a relation between c_1 and c_2

$$c_2 = -c_1 \frac{J_1(k\beta)}{Y_1(k\beta)} \quad (2.77)$$

which can be substituted in equation (2.75) to give

$$\frac{d\Psi}{d\xi} = -c_1 k \left[J_1(k\xi) - \frac{J_1(k\beta)}{Y_1(k\beta)} Y_1(k\xi) \right] \quad (2.78)$$

then the second boundary condition in equation (2.76b) is substituted to give

$$-c_1 k \left[J_1(k\beta+1) - \frac{J_1(k\beta)}{Y_1(k\beta)} Y_1(k\beta+1) \right] \quad (2.79)$$

The roots of equation (2.79) are obtained numerically, and then used to find the different values for k . These values are substituted into the temporal eigenvalue equation (2.71) to get the dimensionless natural frequencies of the linearly varying area resonator.

Table 2.1: **Natural frequencies of linearly varying area ducts with two different parameters versus a straight duct with the same length $l = 0.165$ m, with $c_0 = 330$ m/s.**

n	ω_n (Hz) of cylinder	ω_n (Hz) $\beta = 1/3$	ω_n (Hz) $\beta = 10$
1	1000	1062	1000.3
2	2000	2038	2000.2
3	3000	3027	3000.1
4	4000	4021	4000.1

As an example, two different resonators are selected, both have a length $l = 0.165$ m, $D = 0.01$, and $c_0 = 330$ m/s. However, the first one has the parameter $\beta = 1/3$ which corresponds to a resonator with the big end radius as twice as that of the small end, while the other has the parameter $\beta = 10$ which means that the difference in areas of both ends is one tenth of S_0 , i.e. it is almost straight. The natural frequencies of both resonators as compared to those of a cylindrical one with the same length are listed in Table 2.1. As expected, Table 2.1 shows that the natural frequencies of the second resonator are very close to the corresponding straight duct.

Once the natural frequencies of the cavity have been computed, the first N wave numbers can be substituted in (2.74) to find a set of N trial functions

$$\Psi_n(X) = J_0(k_n(\beta + X)) - \frac{J_1(k_n\beta)}{Y_1(k_n\beta)} Y_0(k_n(\beta + X)) \quad (2.80)$$

from which one can find the weight functions from equation (2.45) and hence the

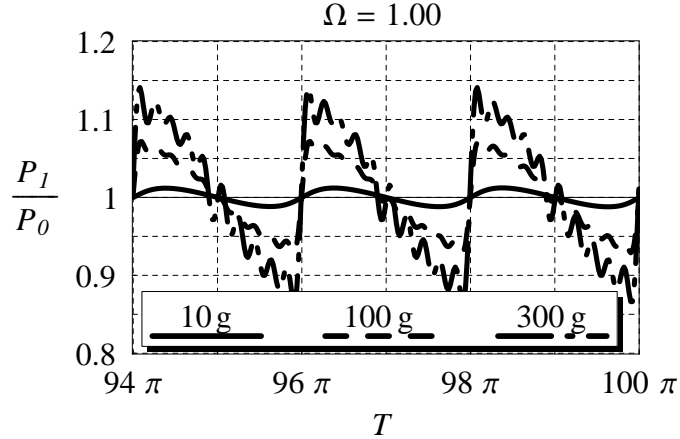


Figure 2.12: **Pressure ratio predicted at the small end of a linearly varying area resonator ($\beta = 10$) excited at $\Omega = 1$ with different amplitudes $a_0 = 10g, 100g, 300g$. ($D = 0.01, l = 0.225$ m, $c = 330$ m/s, $\gamma = 1.2, N = 10$).**

coefficient matrices according to equations (2.44). The model developed for linearly varying area cavities has been applied to a set of resonators with different parameters β and at different levels of excitation acceleration. It is worth mentioning that the Bessel functions that describe the mode shapes in the linearly-varying area resonators require extensive computational effort and hence in many cases a reduced number of modes will be used in the analysis which results in non smooth curves.

Figure 2.13 shows the pressure wave at the small end of a linearly-varying area resonator $X = 0$ for different excitation amplitudes $a_0 = 50g, 100g, 200g$ at its fundamental frequency. These results were obtained by assuming $D = 0.01, l = 0.225$ m, $c_0 = 330$ m/s, with the first 10 mode shapes used. The parameter β has been selected as 10 in order to compare the results with those obtained for straight ducts. When compared to the similar case in straight ducts, it is obvious that the shock waves have

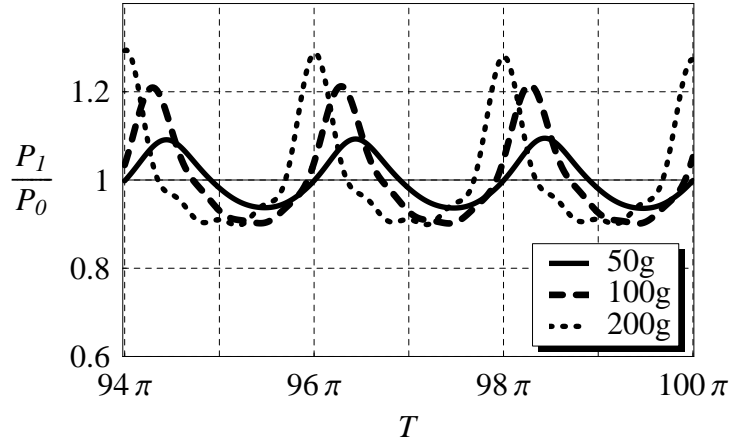


Figure 2.13: **Pressure ratio predicted at one end of a linearly varying area resonator ($\beta = \frac{1}{3}$) excited at $\Omega = 1$ with different amplitudes $a_0 = 50g, 100g, 200g$. ($D = 0.01, l = 0.225$ m, $c = 330$ m/s, $\gamma = 1.2, N = 4$).**

developed at almost the same pressure ratios.

When the parameter β is changed to $1/3$ i.e. the large end radius is as twice as the small end one, the fundamental frequency becomes 779 Hz. The pressure ratios predicted at the fundamental frequency for different excitations are shown in Figure 2.13 for the accelerations a_0 of 50g, 100g, and 200g. It is obvious that changing β allowed the cavity to have shock free waves at higher excitation amplitudes, and hence larger compression ratios up to 1.3 have been reached.

2.4 Theoretical Model of Piston Driven Resonators

In a piston driven resonator the boundaries of the cavity are held fixed except for one of the boundaries at $X = 1$ normal to the axis of the resonator which is considered

as the piston side. Entirely driven resonators have less practical applications than the piston driven ones. This fact makes the study of the latter more vital. In this section, the equations of entirely driven resonators will be modified to suit the case of piston driven ones. The differences in the theoretical model between both resonator systems will be emphasized. The difficulties that arise in the theoretical analysis of piston driven resonators due to the motion of the boundary rather than the body excitation will be focused on.

2.4.1 Equations of Piston Driven Resonators

The governing equations of the entirely driven resonators; conservation of mass (2.1), conservation of momentum (2.7) and state equation (2.8) all hold for the case of piston driven resonators except that they have the special case of $a(t) = 0$.

Therefore, the governing equation in terms of the velocity potential function becomes

$$\begin{aligned} \frac{c_0^2}{s} \frac{\partial}{\partial x} \left(s \frac{\partial \varphi}{\partial x} \right) - \frac{\partial^2 \varphi}{\partial t^2} = \frac{\partial^2 \varphi}{\partial t \partial x} \frac{\partial \varphi}{\partial x} + \frac{\gamma - 1}{s} \frac{\partial \varphi}{\partial t} \frac{\partial}{\partial x} \left(s \frac{\partial \varphi}{\partial x} \right) + \frac{1}{3} \frac{\partial}{\partial x} \left(\frac{\partial \varphi}{\partial x} \right)^3 \\ + \frac{\gamma - 1}{2s} \left(\frac{\partial \varphi}{\partial x} \right)^2 \frac{\partial}{\partial x} \left(s \frac{\partial \varphi}{\partial x} \right) - \frac{\delta}{s} \frac{\partial^2}{\partial t \partial x} \left(s \frac{\partial \varphi}{\partial x} \right) \end{aligned} \quad (2.81)$$

and in terms of the dimensionless variables

$$\begin{aligned} \frac{\partial^2 \Phi}{\partial T^2} - \frac{1}{\Omega^2 \pi^2} \left(\frac{1}{S} \frac{\partial S}{\partial X} \frac{\partial \Phi}{\partial X} + \frac{\partial^2 \Phi}{\partial X^2} \right) + \frac{2}{\Omega} \frac{\partial^2 \Phi}{\partial T \partial X} \frac{\partial \Phi}{\partial X} \\ + \frac{\gamma - 1}{\Omega} \frac{\partial \Phi}{\partial T} \left(\frac{1}{S} \frac{\partial S}{\partial X} \frac{\partial \Phi}{\partial X} + \frac{\partial^2 \Phi}{\partial X^2} \right) - \frac{D}{\pi^3 \Omega} \left(\frac{1}{S} \frac{\partial S}{\partial X} \frac{\partial^2 \Phi}{\partial T \partial X} + \frac{\partial^3 \Phi}{\partial T \partial X^2} \right) \\ + \frac{1}{3\Omega^2} \frac{\partial}{\partial X} \left(\frac{\partial \Phi}{\partial X} \right)^3 + \frac{\gamma - 1}{\Omega^2} \left(\frac{\partial \Phi}{\partial X} \right)^2 \left(\frac{1}{S} \frac{\partial S}{\partial X} \frac{\partial \Phi}{\partial X} + \frac{\partial^2 \Phi}{\partial X^2} \right) = 0 \end{aligned} \quad (2.82)$$

As before, the velocity potential can be approximated as time weighted summation of the cavity mode shapes as in equation (2.39) and then multiplied by arbitrary weighting functions W_j and then integrated over the whole domain to get the weighted residual form

$$\begin{aligned}
& \int_0^1 W_j \Psi_n \frac{d^2 \eta_m}{dT^2} dX - \frac{1}{\Omega^2 \pi^2} \int_0^1 W_j \left(\frac{1}{S} \frac{dS}{dX} \frac{d\Psi_n}{dX} + \frac{d^2 \Psi_n}{dX^2} \right) \eta_n dX \\
& + \int_0^1 W_j \left[\frac{2}{\Omega} \frac{d\Psi_n}{dX} \frac{d\Psi_m}{dX} + \frac{\gamma - 1}{\Omega} \left(\frac{1}{S} \frac{\partial S}{\partial X} \frac{d\Psi_m}{dX} + \frac{d^2 \Psi_m}{dX^2} \right) \Psi_n \right] \frac{d\eta_n}{dT} \eta_m dX \\
& - \frac{D}{\pi^3 \Omega} \int_0^1 W_j \left(\frac{1}{S} \frac{dS}{dX} \frac{d\Psi_n}{dX} + \frac{d^2 \Psi_n}{dX^2} \right) \frac{d\eta_n}{dT} dX \\
& + \frac{1}{3\Omega^2} \int_0^1 W_j \frac{d}{dX} \left(\frac{d\Psi_n}{dX} \frac{d\Psi_m}{dX} \frac{d\Psi_p}{dX} \right) \eta_n \eta_m \eta_p dX \\
& + \frac{\gamma - 1}{2\Omega^2} \int_0^1 W_j \frac{d\Psi_n}{dX} \frac{d\Psi_m}{dX} \left(\frac{1}{S} \frac{dS}{dX} \frac{d\Psi_p}{dX} + \frac{d^2 \Psi_p}{dX^2} \right) \eta_n \eta_m \eta_p dX = 0
\end{aligned} \tag{2.83}$$

where the indices $j, n, m,$ and p all take the values of $1, 2, \dots, N$. Again, equation (2.83) can be assembled in the compact form of

$$A_{jn} \frac{d^2 \eta_n}{dT^2} + B_{jn} \eta_n + C_{jnm} \frac{d\eta_n}{dT} \eta_m + D_{jn} \frac{d\eta_n}{dT} + E_{jnmp} \eta_n \eta_m \eta_p = 0 \tag{2.84}$$

where

$$A_{jn} = \int_0^1 W_j \Psi_n dX, \quad (2.85a)$$

$$B_{jn} = -\frac{1}{\Omega^2 \pi^2} \int_0^1 W_j \left(\frac{1}{S} \frac{dS}{dX} \frac{d\Psi_n}{dX} + \frac{d^2 \Psi_n}{dX^2} \right) dX, \quad (2.85b)$$

$$C_{jnm} = \frac{2}{\Omega} \int_0^1 W_j \frac{d\Psi_n}{dX} \frac{d\Psi_m}{dX} dX \\ + \frac{\gamma - 1}{\Omega} \int_0^1 W_j \left[\Psi_n \frac{d^2 \Psi_m}{dX^2} + \left(\frac{1}{S} \frac{\partial S}{\partial X} \right) \Psi_n \frac{d\Psi_m}{dX} \right] dX, \quad (2.85c)$$

$$D_{jn} = -\frac{D}{\pi^3 \Omega} \int_0^1 W_j \left(\frac{1}{S} \frac{dS}{dX} \frac{d\Psi_n}{dX} + \frac{d^2 \Psi_n}{dX^2} \right) dX, \quad (2.85d)$$

$$E_{jnmp} = \frac{1}{3\Omega^2} \int_0^1 W_j \frac{d}{dX} \left(\frac{d\Psi_n}{dX} \frac{d\Psi_m}{dX} \frac{d\Psi_p}{dX} \right) dX \\ \text{and} \\ + \frac{\gamma - 1}{2\Omega^2} \int_0^1 W_j \frac{d\Psi_n}{dX} \frac{d\Psi_m}{dX} \left(\frac{1}{S} \frac{dS}{dX} \frac{d\Psi_p}{dX} + \frac{d^2 \Psi_p}{dX^2} \right) dX. \quad (2.85e)$$

2.4.2 Boundary Conditions of Piston Driven Resonators

The boundary conditions for the piston driven resonators are

$$u(0, t) = 0, \quad (2.86a)$$

$$\text{and} \quad u(l, t) = v_p \sin(\omega t) \quad (2.86b)$$

where v_p is the amplitude of the piston velocity. In terms of the velocity potential function defined in (2.10) the boundary conditions are

$$\frac{\partial \varphi(0, t)}{\partial x} = 0, \quad (2.87a)$$

$$\text{and} \quad \frac{\partial \varphi(l, t)}{\partial x} = v_p \sin(\omega t) \quad (2.87b)$$

and in terms of the dimensionless variables defined in (2.26d)

$$\frac{\partial\Phi(0, T)}{\partial X} = 0, \quad (2.88a)$$

$$\text{and } \frac{\partial\Phi(1, T)}{\partial X} = \frac{v_p}{\pi c_0} \sin(T) \quad (2.88b)$$

Separating variables as in equation (2.30) and observing the time-independence of the boundary condition at $X = 0$ one can easily deduce

$$\frac{\partial\Psi(0)}{\partial X} = 0, \quad (2.89a)$$

$$\text{and } \frac{\partial\Psi(1)}{\partial X} \eta(T) = \frac{v_p}{\pi c_0} \sin(T) \quad (2.89b)$$

The system of equations (2.84) and (2.85) is by no means simpler than that of the entirely driven equations (2.43) and (2.44). The reason is that the forcing in the piston driven resonator is not explicitly manifested by a forcing term as in the entirely driven case. In fact, the weighted residual form made the forcing implicit in other terms which makes the selection of the basis and weight functions very tricky as they have to satisfy the excitation dependent mode shapes in equation (2.89). In other words, equations (2.84) do not have any information about the forcing because it is implicitly determined by the selection of basis functions, which puts a lot of burden on the user of the model.

2.5 Summary

In this chapter the theoretical modeling of the dynamics and acoustics of gas-filled resonators of simple geometries has been presented. The equations are derived by using the basic equations of conservation of mass, momentum, and energy. These equations are obtained for resonator cavities which are oscillating as well as for cavities that have one oscillating boundary normal to the axis. Solution of these equations is obtained using the weighted residual method. Numerical results are presented for cylindrical, exponential and linearly-varying area resonators. The results for the selected cases show that the theoretical nonlinear model is successful in capturing shock waves and other phenomena which a linear model will fail to capture. It also matches results obtained by other models available in the literature. The obtained results show that the exponentially varying cavities amongst the three discussed geometries produce the largest pressure ratios. The obtained results suggest also that there is an optimal cavity acceleration beyond which shock waves start developing in the cavity and hence energy is dissipated into heat. However, the theoretical model in this form has several drawbacks including being

- limited to very simple geometries whose mode shapes can be easily extracted from the linearized version of the model,
- computationally expensive due to the integral definitions of the coefficient tensors,
- very hard to apply to the case of piston driven resonators due to the embedding

of the boundary forcing into the selection of basis and weight functions.

The developed distributed-parameter mathematical model will be discretized in Chapter 3 using the theory of finite elements to enable the analysis be expanded for complex geometries and addressing more practical situations.

Chapter 3

Finite Element Formulation for Arbitrary Shaped Resonators

3.1 Introduction

In this chapter, a finite element model will be constructed for harmonic oscillations in axisymmetric acoustic resonators. The finite element formulation is based on the theoretical model that was developed in the previous chapter. The finite element model is based on the same governing equations with the same assumptions made. The main characteristic of the finite element model is that it puts the problem in a weak integral rather than a weighted residual form. In the weak form, the domain can be discretized into finite elements so that the solution variable is piecewise continuous over the domain of the problem. The finite element formulation makes it possible to

tackle all types of geometries and not only simple ones. Moreover, it is fast and the computational time is independent of the complexity of the geometry. Most importantly, the boundary conditions are included in the weak formulation and hence more practical cases such as piston driven resonators and resonators with external flow can be addressed.

3.2 Finite Element Model for Entirely Driven Resonators

The entirely driven resonator shown in Figure 3.1 is considered. In this case, the entire resonator is subjected to a sinusoidal excitation that oscillates both the cavity and the gas inside it. This excitation causes the gas to generate standing waves. The governing equations are the conservation of mass, momentum and state equations which all boil down to one governing equation when the velocity potential function is used. As in the mathematical model developed in the previous chapter, we start by extracting the mode shapes for the free oscillations of the gas inside and then use them as basis functions for predicting the response due external excitations.

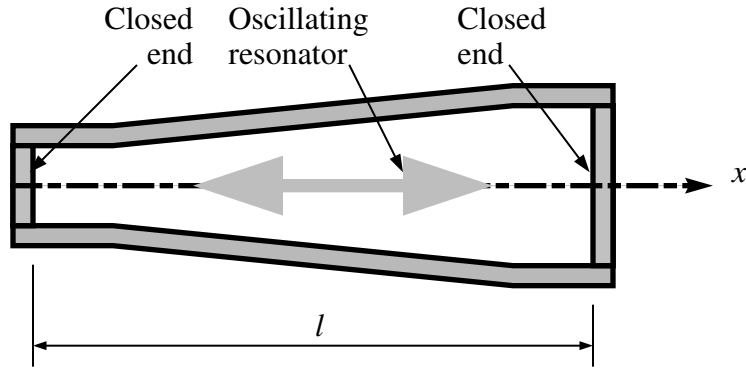


Figure 3.1: Schematic of an Entirely Driven Resonator.

3.2.1 Free Oscillations of Entirely Driven Resonators

We start by the linearized dimensionless equations for the free oscillations of the acoustic resonator. From equation (2.31), the strong form of the spatial problem is

$$S \frac{d^2 \Psi}{dX^2} + \frac{dS}{dX} \frac{d\Psi}{dX} + k^2 S \Psi = 0 \quad (3.1)$$

The strong form is multiplied by an arbitrary weight function $W(X)$ and integrated over the whole domain to obtain the weighted residual form

$$\int_0^1 W \left(S \frac{d^2 \Psi}{dX^2} + \frac{dS}{dX} \frac{d\Psi}{dX} + k^2 S \Psi \right) dX = 0 \quad (3.2)$$

Integrating the second order term of equation (3.2) by parts results in the following weak form

$$\int_0^1 \left(-S \frac{dW}{dX} \frac{d\Psi}{dX} + k^2 S W \Psi \right) dX + \left[W \frac{d\Psi}{dX} \right]_0^1 = 0 \quad (3.3)$$

For a closed resonator from both ends, the boundary conditions in equation (2.37) hold and hence both boundary terms vanish.

Equation (3.3) holds for the whole domain as well as a small element of length l^e as the one shown in Figure 3.2.

$$\int_0^{l^e} \left(-S \frac{dW^e}{dX} \frac{d\Psi^e}{dX} + k^2 S W \Psi^e \right) dX = 0 \quad (3.4)$$

One need not to worry about the boundary terms of internal elements as they will cancel out during the assembly process. Within each element, Ψ is approximated using classical interpolation functions such that

$$\Psi^e = N_s \psi_s^e \quad (3.5)$$

where N_s and ψ_s^e are the basis function and the solution for Ψ^e at the s^{th} node which belongs to the element e . Index notation has been used in which indices take all possible values in their range and a repeated index indicates summation. The weighting functions are chosen as variations of Ψ^e such that

$$W^e = \delta\Psi^e = N_r \delta\psi_r^e \quad (3.6)$$

The elements are mapped to a reference element of unit length whose first node lies at the origin as shown in Figure 3.2. The approximate Ψ^e given by equation (3.5) and the weighting functions given by equation (3.6) are substituted into equation (3.4) for each element giving

$$\delta\psi_r^e \int_0^1 \left(-\frac{1}{l^{e2}} S(\xi) \frac{dN_r}{d\xi} \frac{dN_s}{d\xi} + k^2 S(\xi) N_r N_s \right) l^e d\xi \cdot \psi_s^e = 0 \quad (3.7)$$

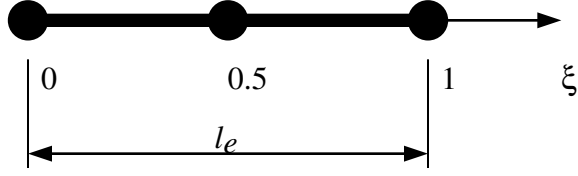


Figure 3.2: **Three-node acoustic element.**

which can be put in the following compact form

$$(K_{rs}^e + k^2 M_{rs}^e) \psi_s^e = 0 \quad (3.8)$$

where

$$K_{rs} = \frac{1}{l^e} \int_0^1 \left(-S(\xi) \frac{dN_r}{d\xi} \frac{dN_s}{d\xi} \right) d\xi \quad (3.9)$$

and

$$M_{rs} = l^e \int_0^1 (S(\xi) N_r N_s) d\xi \quad (3.10)$$

All the elements are assembled together such that the following system of equations is developed

$$(\mathbf{K} + k^2 \mathbf{M}) \mathbf{\Psi} = 0 \quad (3.11)$$

where \mathbf{K} and \mathbf{M} are the coefficient matrices of a generalized eigenvalue problem, and $\mathbf{\Psi}$ is the global solution vector for Ψ at the nodes. The eigensystem of equation (3.11) has as much eigenvalues k_n^2 and eigenvectors ψ_n as the number of free nodes in the finite element model. Eigenvalues for the first N modes can be numerically evaluated while the rest are ignored. Finally the mode shapes Ψ_n for the dimensionless velocity potential function Φ are calculated by substituting ψ_n in equation (3.5) for each element. It is crucial to notice from equations (3.9) and (3.10) that the mode

shapes are orthogonal with respect to the cross sectional area of the resonator $S(X)$. This is important for the choice of the weighting functions when solving for the time dependant functions later on.

3.2.2 Forced Oscillations of Entirely Driven Resonators

Once again, we start from the governing equation from the previous chapter. The weighted residual form is obtained by multiplying equation (2.28) by a weight function $W(X)$ and integrating over the domain. When subjected to external excitation, the response of the acoustic resonator is expected to be a combination of its normal modes. Therefore, the dimensionless velocity potential function Φ is expressed as time weighted sums of the first N modes

$$\Phi(X, T) \simeq \eta_n(T)\Psi_n(X) \tag{3.12}$$

where $n = 1, 2, \dots, N$. Therefore, the weighted residual form becomes

$$\begin{aligned}
& \int_0^1 W_j \Psi_n \frac{d^2 \eta_m}{dT^2} dX - \frac{1}{\Omega^2 \pi^2} \int_0^1 W_j \left(\frac{1}{S} \frac{dS}{dX} \frac{d\Psi_n}{dX} + \frac{d^2 \Psi_n}{dX^2} \right) \eta_m dX \\
& + \int_0^1 W_j \left[\frac{2}{\Omega} \frac{d\Psi_n}{dX} \frac{d\Psi_m}{dX} + \frac{\gamma - 1}{\Omega} \left(\frac{1}{S} \frac{\partial S}{\partial X} \frac{d\Psi_m}{dX} + \frac{d^2 \Psi_m}{dX^2} \right) \Psi_n \right] \frac{d\eta_n}{dT} \eta_m dX \\
& - \frac{D}{\pi^3 \Omega} \int_0^1 W_j \left(\frac{1}{S} \frac{dS}{dX} \frac{d\Psi_n}{dX} + \frac{d^2 \Psi_n}{dX^2} \right) \frac{d\eta_n}{dT} dX \\
& + \frac{1}{3\Omega^2} \int_0^1 W_j \frac{d}{dX} \left(\frac{d\Psi_n}{dX} \frac{d\Psi_m}{dX} \frac{d\Psi_p}{dX} \right) \eta_m \eta_n \eta_p dX \\
& + \frac{\gamma - 1}{2\Omega^2} \int_0^1 W_j \frac{d\Psi_n}{dX} \frac{d\Psi_m}{dX} \left(\frac{1}{S} \frac{dS}{dX} \frac{d\Psi_p}{dX} + \frac{d^2 \Psi_p}{dX^2} \right) \eta_m \eta_n \eta_p dX \\
& = -\frac{F}{\Omega^2} \int_0^1 W_j \frac{d\Psi_n}{dX} \eta_m dX - \frac{\gamma - 1}{\Omega^2} F \int_0^1 W_j \left(\frac{1}{S} \frac{dS}{dX} \frac{d\Psi_n}{dX} + \frac{d^2 \Psi_n}{dX^2} \right) \eta_m X dX \\
& - \frac{1}{\Omega} \frac{dF}{dT} \int_0^1 X W_j dX
\end{aligned} \tag{3.13}$$

The second order terms in X in the weighted residual form equation (3.13) are integrated by parts to obtain the weak form

$$\begin{aligned}
& \int_0^1 W_j \Psi_n dX \frac{d^2 \eta_n}{dT^2} - \frac{1}{\Omega^2 \pi^2} \int_0^1 \left(W_j \frac{1}{S} \frac{dS}{dX} - \frac{dW_j}{dX} \right) \frac{d\Psi_n}{dX} dX \cdot \eta_n \\
& + \frac{2}{\Omega} \int_0^1 W_j \frac{d\Psi_n}{dX} \frac{d\Psi_m}{dX} dX \frac{d\eta_n}{dT} \eta_m \\
& + \frac{\gamma - 1}{\Omega} \int_0^1 \left(W_j \frac{1}{S} \frac{\partial S}{\partial X} \Psi_n - \frac{dW_j}{dX} \Psi_n - W_j \frac{d\Psi_n}{dX} \right) \frac{d\Psi_m}{dX} dX \frac{d\eta_n}{dT} \eta_m \\
& - \frac{D}{\pi^3 \Omega} \int_0^1 \left(W_j \frac{1}{S} \frac{dS}{dX} - \frac{dW_j}{dX} \right) \frac{d\Psi_n}{dX} dX \frac{d\eta_n}{dT} \\
& - \frac{1}{3\Omega^2} \int_0^1 \frac{dW_j}{dX} \frac{d\Psi_n}{dX} \frac{d\Psi_m}{dX} \frac{d\Psi_p}{dX} dX \eta_n \eta_m \eta_p \\
& + \frac{\gamma - 1}{2\Omega^2} \int_0^1 W_j \frac{d\Psi_n}{dX} \frac{d\Psi_m}{dX} \left(\frac{1}{S} \frac{dS}{dX} \frac{d\Psi_p}{dX} + \frac{d^2 \Psi_p}{dX^2} \right) dX \cdot \eta_n \eta_m \eta_p \\
& - \frac{\gamma - 1}{\Omega^2} F \int_0^1 \frac{d\Psi_n}{dX} \left[W_j + X \left(\frac{dW_j}{dX} - \frac{1}{S} \frac{dS}{dX} \right) \right] dX \eta_n + \frac{F}{\Omega^2} \int_0^1 \frac{d\Psi_n}{dX} W_j dX \eta_n \\
& + \frac{1}{\Omega} \frac{dF}{dT} \int_0^1 X W_j dX - \frac{1}{\Omega^2 \pi^2} \left[W_j \frac{d\Psi_n}{dX} \right]_0^1 \eta_n + \frac{\gamma - 1}{\Omega} \left[W_j \Psi_n \frac{d\Psi_m}{dX} \right]_0^1 \frac{d\eta_n}{dT} \eta_m \\
& - \frac{D}{\pi^3 \Omega} \left[W_j \frac{d\Psi_n}{dX} \right]_0^1 \frac{d\eta_n}{dT} + \frac{3\gamma + 1}{6\Omega^2} \left[W_j \frac{d\Psi_n}{dX} \frac{d\Psi_m}{dX} \frac{d\Psi_p}{dX} \right]_0^1 \eta_n \eta_m \eta_p \\
& + \frac{\gamma - 1}{\Omega^2} F \left[X W_j \frac{d\Psi_n}{dX} \right]_0^1 \eta_n = 0
\end{aligned} \tag{3.14}$$

According to equation (2.37) all boundary terms in equation (3.14) will vanish.

Therefore, for the case of entirely driven resonators closed from both ends the weak form reduces to

$$\begin{aligned}
& \int_0^1 W_j \Psi_n dX \frac{d^2 \eta_n}{dT^2} - \frac{1}{\Omega^2 \pi^2} \int_0^1 \left(W_j \frac{1}{S} \frac{dS}{dX} - \frac{dW_j}{dX} \right) \frac{d\Psi_n}{dX} dX \cdot \eta_n \\
& - \frac{\gamma - 1}{\Omega^2} F \int_0^1 \frac{d\Psi_n}{dX} \left[W_j + X \left(\frac{dW_j}{dX} - \frac{1}{S} \frac{dS}{dX} \right) \right] dX \eta_n \\
& + \frac{F}{\Omega^2} \int_0^1 \frac{d\Psi_n}{dX} W_j dX \eta_n + \frac{2}{\Omega} \int_0^1 W_j \frac{d\Psi_n}{dX} \frac{d\Psi_m}{dX} dX \frac{d\eta_m}{dT} \eta_m \\
& + \frac{\gamma - 1}{\Omega} \int_0^1 \left(W_j \frac{1}{S} \frac{\partial S}{\partial X} \Psi_n - \frac{dW_j}{dX} \Psi_n - W_j \frac{d\Psi_n}{dX} \right) \frac{d\Psi_m}{dX} dX \frac{d\eta_m}{dT} \eta_m \\
& - \frac{D}{\pi^3 \Omega} \int_0^1 \left(W_j \frac{1}{S} \frac{dS}{dX} - \frac{dW_j}{dX} \right) \frac{d\Psi_n}{dX} dX \frac{d\eta_n}{dT} \\
& - \frac{1}{3\Omega^2} \int_0^1 \frac{dW_j}{dX} \frac{d\Psi_n}{dX} \frac{d\Psi_m}{dX} \frac{d\Psi_p}{dX} dX \eta_n \eta_m \eta_p \\
& + \frac{\gamma - 1}{2\Omega^2} \int_0^1 W_j \frac{d\Psi_n}{dX} \frac{d\Psi_m}{dX} \left(\frac{1}{S} \frac{dS}{dX} \frac{d\Psi_p}{dX} + \frac{d^2 \Psi_p}{dX^2} \right) dX \cdot \eta_n \eta_m \eta_p \\
& = -\frac{1}{\Omega} \frac{dF}{dT} \int_0^1 X W_j dX
\end{aligned} \tag{3.15}$$

The domain is divided into discrete elements of equal length l_i^e , and hence the integration of any function $f(X)$ over the whole domain can be expressed as summation of integrations over the elements domain for all the elements.

$$\int_0^1 f(X) dX = \sum_{i=1}^{nel} \int_{l_i^e} f(X) dX \tag{3.16}$$

where nel is the total number of elements. Furthermore, the integration over the element can be approximated by numerical integration. If the elements are sufficiently small, the integration can be replaced by the product of the function value at the

middle node $f^e(\xi = 0.5)$ and the length of the element.

$$\int_0^1 f(X) dX \simeq \sum_{i=1}^{nel} l_i^e f^e \quad (3.17)$$

Therefore, equation (3.15) can be assembled in the following compact form

$$A_{jn} \frac{d^2 \eta_n}{dT^2} + B_{jn} \eta_n + C_{jnm} \frac{d\eta_n}{dT} \eta_m + D_{jn} \frac{d\eta_n}{dT} + E_{jnmp} \eta_n \eta_m \eta_p = F_j \quad (3.18)$$

which is the same as equation (2.43) from the previous chapter except that the definitions for the coefficient tensors are completely altered. The new definitions are

$$A_{jn} = l_i^e W_{ji} \Psi_{ni}, \quad (3.19a)$$

$$B_{jn} = \frac{-l_i^e}{\Omega^2 \pi^2} \left[\frac{1}{S_i} \frac{dS_i}{dX} W_{ji} \frac{d\Psi_{ni}}{dX} - \frac{dW_{ji}}{dX} \frac{d\Psi_{ni}}{dX} \right] + \frac{l_i^e}{\Omega^2} F W_{ji} \frac{d\Psi_{ni}}{dX} \\ + \frac{(\gamma - 1) l_i^e}{\Omega^2} F \left[X_i \frac{1}{S_i} \frac{dS_i}{dX} W_{ji} - X_i \frac{dW_{ji}}{dX} \right] \frac{d\Psi_{ni}}{dX}, \quad (3.19b)$$

$$C_{jnm} = \frac{\gamma - 1}{\Omega} l_i^e \left[\frac{1}{S_i} \frac{dS_i}{dX} W_{ji} \Psi_{ni} - \frac{dW_{ji}}{dX} \Psi_{ni} - W_{ji} \frac{d\Psi_{ni}}{dX} \right] \frac{d\Psi_{mi}}{dX} \\ + \frac{2l_i^e}{\Omega} W_{ji} \frac{d\Psi_{ni}}{dX} \frac{d\Psi_{mi}}{dX}, \quad (3.19c)$$

$$D_{jn} = -\frac{Dl_i^e}{\pi^3 \Omega} \left[\frac{1}{S_i} \frac{dS_i}{dX} W_{ji} - \frac{dW_{ji}}{dX} \right] \frac{d\Psi_{ni}}{dX}, \quad (3.19d)$$

$$E_{jnmp} = -\frac{l_i^e}{3\Omega^2} \frac{dW_{ji}}{dX} \frac{d\Psi_{ni}}{dX} \frac{d\Psi_{mi}}{dX} \frac{d\Psi_{pi}}{dX} \\ + \frac{\gamma - 1}{2\Omega^2} l_i^e W_{ji} \left[\frac{d\Psi_{ni}}{dX} \frac{d\Psi_{mi}}{dX} \left(\frac{1}{S_i} \frac{dS_i}{dX} \frac{d\Psi_{pi}}{dX} + \frac{d\Psi_{pi}}{dX} \right) \right], \quad (3.19e)$$

$$\text{and } F_j = -\frac{l_i^e}{\Omega} \frac{dF}{dT} X_i W_{ji}. \quad (3.19f)$$

In equations (3.19) the repeated index i indicates summation of all elements. The definitions for the coefficient tensors show one important characteristic of the finite

element method where the integrations of complicated functions in equations (2.44) have been replaced by simple summations over simple functions in (3.19). This results in being able to solve any type of resonator geometry, faster in computing, and the computation time is independent of the complexity of the geometry.

The weighting functions $W_j(X)$ are arbitrary but conveniently chosen as

$$W_j(X) = S(X) \Psi(X) \quad (3.20)$$

and the reason for this choice is that equations (3.9) and (3.10) show that the mode shapes Ψ and their derivatives are both orthogonal with respect to the area $S(X)$. Hence, all the off diagonal terms in the linear terms will be zero.

As $\Psi_n(X)$ are known and $W_j(X)$ are chosen, the coefficient tensors given by equations (3.19) can be easily calculated. Substituting these coefficient tensors into equation (3.18) yields a system of N second order ordinary differential equation in N unknown $\eta_n(T)$ functions. It is worth mentioning that equation (3.18) keeps track of all terms including the quadratic and cubic ones. The system of equations is numerically solved for $\eta_n(T)$, then the dimensionless velocity potential function can be evaluated from equation (3.12). The velocity potential function can be in turn used to evaluate all other variables of interest. Most importantly the pressure ratio P/P_0 can be found from equation (2.57).

3.3 Numerical Examples for Entirely Driven Resonators

In this section the finite element model for entirely driven resonators which was developed in section 3.2 will be used to predict the performance of resonators with simple geometries for which closed-form solutions are known. This enables us to validate the finite element model and hence to have enough confidence to proceed to more advanced cases. The model can then be used to predict the performance of resonators with complex geometries.

3.3.1 Cylindrical Resonators

Figure 3.3 shows a schematic of a cylindrical resonator of total length $l = 0.165$ m and its first 2 velocity mode shapes. It is assumed that the gas inside has a speed of sound $c_0 = 330$ m/s, dissipation coefficient $D = 0.01$, and ratio of specific heats $\gamma = 1.2$.

Figure 3.4 shows the time response of the pressure ratio at one end of a cylindrical resonator as predicted by the proposed finite element model as well as the exact model developed in the previous chapter. The resonator is excited at the fundamental frequency with an excitation $F_0 = 5 \times 10^{-4}$. The first twenty modes are considered ($N = 20$). A hundred of 3-node quadratic elements as shown in Figure 3.2 were used. It is evident that the predictions of the finite element model are in perfect agreement

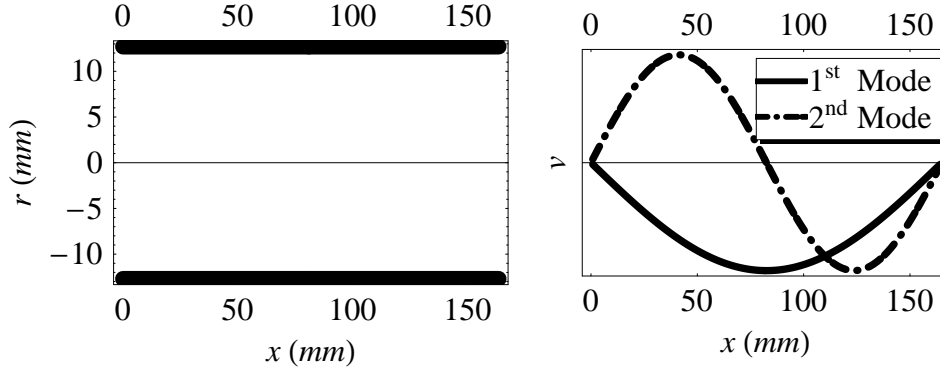


Figure 3.3: **Geometry of a cylindrical resonator (left) and its velocity mode shapes (right).**

with those obtained using the exact mode shapes. The predictions match also the results obtained by Ilinskii *et al.* [23] and Erickson and Zinn [25].

3.3.2 Exponential Resonators

Figure 3.5 shows a cylindrical resonator of total length $l = 0.224$ m and its first 2 velocity mode shapes. The flare constant $\alpha = 5.75$, $c_0 = 330$ m/s, $D = 0.01$, and $\gamma = 1.2$.

Figure 3.6 shows the time response of the pressure ratio at one end of the exponential resonator under consideration as predicted by the proposed finite element model as well as the exact model. The resonator is excited at the fundamental frequency with an excitation $F_0 = 5 \times 10^{-4}$. The first ten modes are considered ($N = 10$). A hundred of 3-node quadratic elements as the one shown in Figure 3.2 are used. It is evident that the predictions of the finite element model match those obtained using

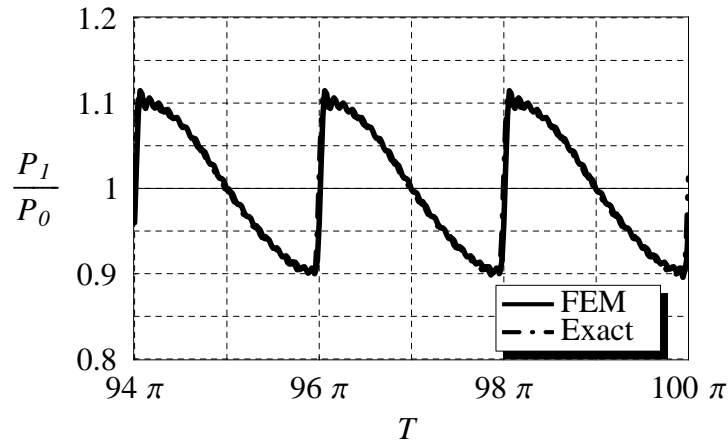


Figure 3.4: Comparison of the pressure ratio predictions carried out by the proposed finite element and the exact models for a cylindrical resonator, ($l = 0.165$ m, $c_0 = 330$ m/s, $D = 0.01$, $\gamma = 1.2$, and $N = 20$).

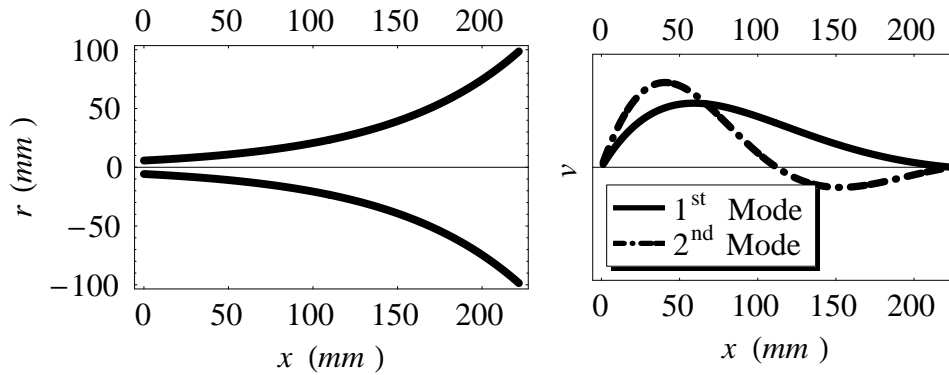


Figure 3.5: Geometry of an exponential resonator (left) with $\alpha = 5.75$ and its velocity mode shapes (right).

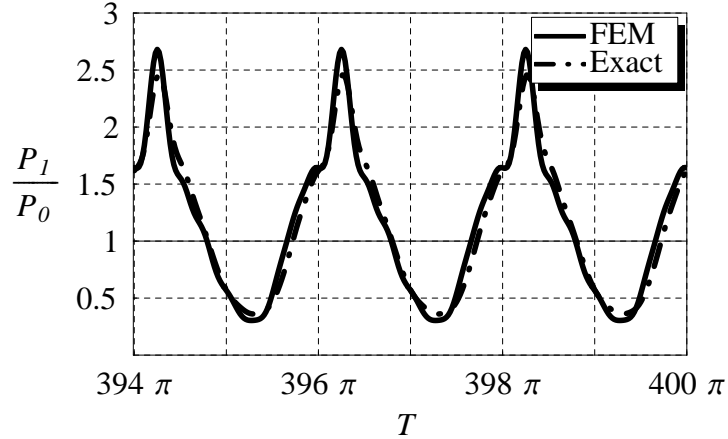


Figure 3.6: Comparison of the pressure ratio predictions carried out by the proposed finite element and the exact models for an exponential resonator ($\alpha = 5.75$, $l = 0.224$ m, $c_0 = 330$ m/s, $D = 0.01$, $\gamma = 1.2$, and $N = 10$).

the exact model with a small error due to working with a highly nonlinear geometry. An adaptive mesh is expected to perform even better by being able to capture the fast changes in the geometry. The predictions match also the results obtained by Erickson and Zinn [25].

3.3.3 Linearly Varying Area Resonators

Figure 3.7 shows a linearly-varying area cavity and the mode shapes obtained using the proposed finite element approach. The resonator characteristics are $l = 0.225$ m linear varying area parameter $\beta = 1/3$, $c_0 = 330$ m/s, $D = 0.01$, and $\gamma = 1.2$.

Figure 3.8 shows the time response of the pressure ratio at one end of the exponential resonator under consideration as predicted by the proposed finite element model

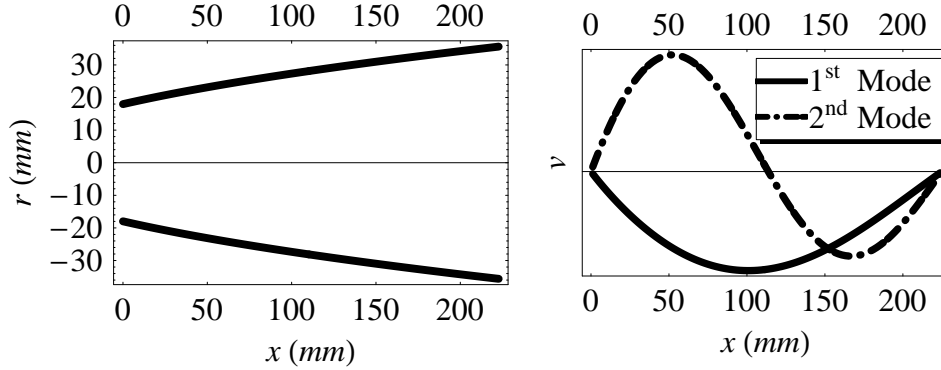


Figure 3.7: **Geometry of a linearly varying area resonator (left) with $\beta = \frac{1}{3}$ and its velocity mode shapes (right).**

as well as the exact model. The resonator is excited at the fundamental frequency with an excitation 100g. The first five modes are considered ($N = 5$). A hundred of 3-node quadratic elements as the one shown in Figure 3.2 are used. It is evident that the predictions of the finite element model match those obtained using the exact mode model. The first three natural frequencies obtained by the finite element approach are: 790.995, 1504.28, 2227.19 Hz, while the corresponding frequencies obtained by the analytical model are: 790.991, 1504.27, 2227.19 Hz. A good agreement between the predictions of the finite element and the analytical models is evident.

3.3.4 Conclusion for the Model Performance

This sections showed that the proposed finite element model is valid for the case of entirely driven resonator as its predictions match those obtained by exact models for simple geometries. This matching emphasizes that the proposed model is reliable

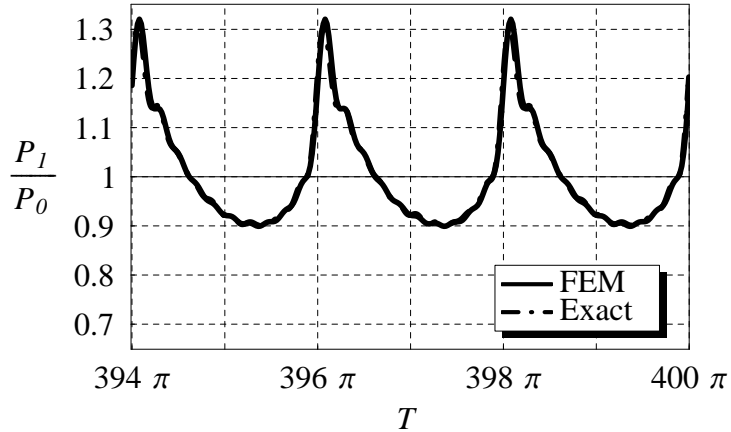


Figure 3.8: Comparison of the pressure ratio predictions carried out by the proposed finite element and the exact models for a linearly varying area resonator ($\beta = \frac{1}{3}$, $l = 0.225\text{m}$, $c_0 = 330\text{ m/s}$, $D = 0.01$, $\gamma = 1.2$, and $N = 5$).

and encourages us to proceed towards using it to more practical situations.

3.4 Finite Element Model for Piston Driven Resonators

The piston driven resonator shown in Figure 3.9 is considered. In this case, the entire resonator is held fixed except for one of the boundaries at $x = l$ or $X = 1$ normal to the axis of the resonator. This boundary excites the gas inside the cavity with a harmonic excitation which causes the gas to generate standing waves. As stated in the previous chapter, the governing equations are the same except for the forcing which arises due to the boundary excitation rather than a body force term. As usual, we study first the free oscillations of the resonator, extract the normal modes

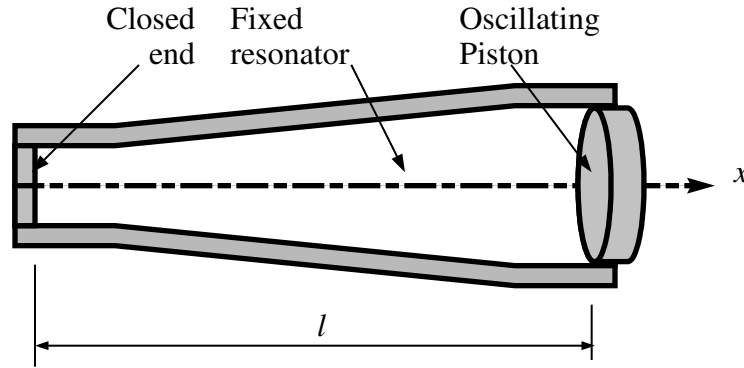


Figure 3.9: Schematic for a Piston Driven Resonator.

and use them as basis functions for the forced oscillations.

3.4.1 Free Oscillations of Piston Driven Resonators

As discussed in section 2.4.1, the equations of entirely driven resonators apply for the case of piston driven resonators except for the body force terms which are zero and the boundary conditions at the piston side. Therefore, the wave equation is the same as that of the entirely driven resonators with the boundary conditions in equation (2.88). In the free oscillations $v_p = 0$. This makes the boundary conditions for the free oscillations as well as the spatial eigenvalue problem exactly the same in both entirely and piston driven resonators. Hence, the mode shapes for both cases are exactly the same. One may impose the question of how accurate it is to use the mode shapes of the unforced case instead of the mode shapes of forced oscillations where the boundary conditions depend on the excitation amplitudes. We claim that, in most practical situations, they are accurate since the excitation amplitude is way

less than the speed of sound $v_p \ll c_0$.

3.4.2 Forced Oscillations of Piston Driven Resonators

Once again, the equations for entirely driven resonators are applicable to those of piston driven ones. Hence, the weak form of the nonlinear governing equation (3.14) applies to piston driven resonators with the first boundary condition from equation (2.89) being zero. Therefore, the weak form becomes

$$\begin{aligned}
& \int_0^1 W_j \Psi_n dX \frac{d^2 \eta_m}{dT^2} - \frac{1}{\Omega^2 \pi^2} \int_0^1 \left(W_j \frac{1}{S} \frac{dS}{dX} - \frac{dW_j}{dX} \right) \frac{d\Psi_n}{dX} dX \cdot \eta_m \\
& + \frac{2}{\Omega} \int_0^1 W_j \frac{d\Psi_n}{dX} \frac{d\Psi_m}{dX} dX \frac{d\eta_m}{dT} \eta_m \\
& + \frac{\gamma - 1}{\Omega} \int_0^1 \left(W_j \frac{1}{S} \frac{\partial S}{\partial X} \Psi_n - \frac{dW_j}{dX} \Psi_n - W_j \frac{d\Psi_n}{dX} \right) \frac{d\Psi_m}{dX} dX \frac{d\eta_m}{dT} \eta_m \\
& - \frac{D}{\pi^3 \Omega} \int_0^1 \left(W_j \frac{1}{S} \frac{dS}{dX} - \frac{dW_j}{dX} \right) \frac{d\Psi_n}{dX} dX \frac{d\eta_m}{dT} \\
& - \frac{1}{3\Omega^2} \int_0^1 \frac{dW_j}{dX} \frac{d\Psi_n}{dX} \frac{d\Psi_m}{dX} \frac{d\Psi_p}{dX} dX \eta_n \eta_m \eta_p \\
& + \frac{\gamma - 1}{2\Omega^2} \int_0^1 W_j \frac{d\Psi_n}{dX} \frac{d\Psi_m}{dX} \left(\frac{1}{S} \frac{dS}{dX} \frac{d\Psi_p}{dX} + \frac{d^2 \Psi_p}{dX^2} \right) dX \cdot \eta_n \eta_m \eta_p \\
& - \frac{1}{\Omega^2 \pi^2} \left[W_j \frac{d\Psi_n}{dX} \right]_{X=1} \eta_m + \frac{\gamma - 1}{\Omega} \left[W_j \Psi_n \frac{d\Psi_m}{dX} \right]_{X=1} \frac{d\eta_m}{dT} \eta_m \\
& - \frac{D}{\pi^3 \Omega} \left[W_j \frac{d\Psi_n}{dX} \right]_{X=1} \frac{d\eta_m}{dT} + \frac{3\gamma + 1}{6\Omega^2} \left[W_j \frac{d\Psi_n}{dX} \frac{d\Psi_m}{dX} \frac{d\Psi_p}{dX} \right]_{X=1} \eta_n \eta_m \eta_p = 0
\end{aligned} \tag{3.21}$$

The nonlinear and dissipative boundary terms are assumed insignificant although not very difficult to implement. Therefore, when the boundary condition at $X = 1$

is substituted from equation (2.89) the weak form integral equation for piston driven resonators becomes

$$\begin{aligned}
& \int_0^1 W_j \Psi_n dX \frac{d^2 \eta_n}{dT^2} - \frac{1}{\Omega^2 \pi^2} \int_0^1 \left(W_j \frac{1}{S} \frac{dS}{dX} - \frac{dW_j}{dX} \right) \frac{d\Psi_n}{dX} dX \cdot \eta_n \\
& + \frac{2}{\Omega} \int_0^1 W_j \frac{d\Psi_n}{dX} \frac{d\Psi_m}{dX} dX \frac{d\eta_n}{dT} \eta_m \\
& + \frac{\gamma - 1}{\Omega} \int_0^1 \left(W_j \frac{1}{S} \frac{\partial S}{\partial X} \Psi_n - \frac{dW_j}{dX} \Psi_n - W_j \frac{d\Psi_n}{dX} \right) \frac{d\Psi_m}{dX} dX \frac{d\eta_n}{dT} \eta_m \\
& - \frac{D}{\pi^3 \Omega} \int_0^1 \left(W_j \frac{1}{S} \frac{dS}{dX} - \frac{dW_j}{dX} \right) \frac{d\Psi_n}{dX} dX \frac{d\eta_n}{dT} \\
& - \frac{1}{3\Omega^2} \int_0^1 \frac{dW_j}{dX} \frac{d\Psi_n}{dX} \frac{d\Psi_m}{dX} \frac{d\Psi_p}{dX} dX \eta_n \eta_m \eta_p \\
& + \frac{\gamma - 1}{2\Omega^2} \int_0^1 W_j \frac{d\Psi_n}{dX} \frac{d\Psi_m}{dX} \left(\frac{1}{S} \frac{dS}{dX} \frac{d\Psi_p}{dX} + \frac{d^2 \Psi_p}{dX^2} \right) dX \cdot \eta_n \eta_m \eta_p \\
& = \frac{1}{\Omega^2 \pi^2} W_j(1) \frac{v_p}{\pi c_0} \sin(T)
\end{aligned} \tag{3.22}$$

Again, the domain is divided into finite elements of length l_e and a system of equation similar to that in equation (3.18) can be constructed with new definitions for the coefficient tensors

$$A_{jn} = l_i^e W_{ji} \Psi_{ni}, \quad (3.23a)$$

$$B_{jn} = \frac{-l_i^e}{\Omega^2 \pi^2} \left[\frac{1}{S_i} \frac{dS_i}{dX} W_{ji} \frac{d\Psi_{ni}}{dX} - \frac{dW_{ji}}{dX} \frac{d\Psi_{ni}}{dX} \right], \quad (3.23b)$$

$$C_{jnm} = \frac{\gamma - 1}{\Omega} l_i^e \left[\frac{1}{S_i} \frac{dS_i}{dX} W_{ji} \Psi_{ni} - \frac{dW_{ji}}{dX} \Psi_{ni} - W_{ji} \frac{d\Psi_{ni}}{dX} \right] \frac{d\Psi_{mi}}{dX} \\ + \frac{2l_i^e}{\Omega} W_{ji} \frac{d\Psi_{ni}}{dX} \frac{d\Psi_{mi}}{dX}, \quad (3.23c)$$

$$D_{jn} = -\frac{Dl_i^e}{\pi^3 \Omega} \left[\frac{1}{S_i} \frac{dS_i}{dX} W_{ji} - \frac{dW_{ji}}{dX} \right] \frac{d\Psi_{ni}}{dX}, \quad (3.23d)$$

$$E_{jnmp} = -\frac{l_i^e}{3\Omega^2} \frac{dW_{ji}}{dX} \frac{d\Psi_{ni}}{dX} \frac{d\Psi_{mi}}{dX} \frac{d\Psi_{pi}}{dX} \\ + \frac{\gamma - 1}{2\Omega^2} l_i^e W_{ji} \left[\frac{d\Psi_{ni}}{dX} \frac{d\Psi_{mi}}{dX} \left(\frac{1}{S_i} \frac{dS_i}{dX} \frac{d\Psi_{pi}}{dX} + \frac{d\Psi_{pi}}{dX} \right) \right], \quad (3.23e)$$

$$\text{and } F_j = \frac{l_i^e}{\Omega^2 \pi^2} W_j(1) \frac{v_p}{\pi c_0} \sin(T) \quad (3.23f)$$

Therefore, one can see from this section that the weak form integral equation allowed embedding the boundary conditions in the finite element model without being confused about the choice of admissible basis functions that satisfy the boundary conditions. The basis functions in the finite element model are the regular mode shapes that can be calculated from the linear wave equations.

3.5 Axisymmetric Resonators with External Flow

Being fast and flexible, the finite element model is capable of tackling practical real-life situations for axisymmetric resonators. Probably, the ultimate goal for an axisymmetric resonator would be to build compact gas compressors which incorporate

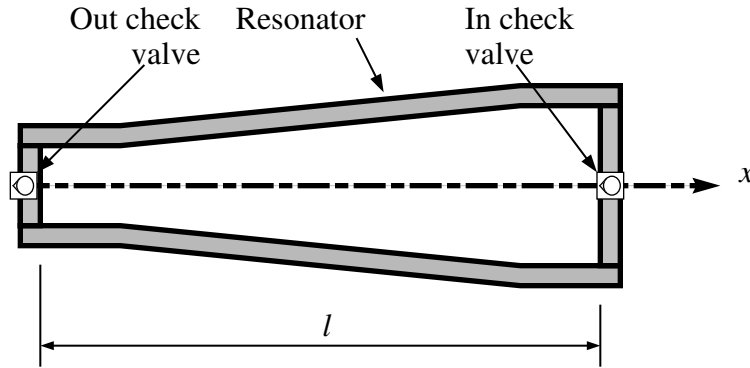


Figure 3.10: **Schematic for an axisymmetric resonator with input and output check valves mounted at the ends.**

gas flow in and out the resonator cavity. Therefore, it is important to include flow boundary conditions in the model and check its effect on the developed pressure ratios.

3.5.1 Finite Element Modeling for Flow Boundary Conditions

Figure 3.10 shows two check valves mounted to an axisymmetric resonator at the ends. The resonator can be either entirely or piston driven. The flow through the valves is assumed small and slow enough such that the mode shapes of the gas oscillations are unaltered. The flow through both ends adds a D.C. component to the velocity terms at the boundaries. Hence, the boundary conditions when the valves are open are

$$u(0, t) = -v_0, \quad (3.24a)$$

$$\text{and } u(l, t) = -v_l + v_p \sin(\omega t). \quad (3.24b)$$

where v_0 is the D.C. flow speed at $x = 0$, v_l is the D.C. flow speed at $x = l$, and v_p is the amplitude of the piston oscillations in case of piston driven resonators and is zero in case of entirely driven ones.

In terms of the velocity potential function defined in (2.10) the boundary conditions are

$$\frac{\partial \varphi(0, t)}{\partial x} = -v_0, \quad (3.25a)$$

$$\text{and } \frac{\partial \varphi(l, t)}{\partial x} = -v_l + v_p \sin(\omega t). \quad (3.25b)$$

and in terms of the dimensionless variables defined in (2.26d)

$$\frac{\partial \Phi(0, T)}{\partial X} = -\frac{v_0}{\pi c_0}, \quad (3.26a)$$

$$\text{and } \frac{\partial \Phi(1, T)}{\partial X} = -\frac{v_l}{\pi c_0} + \frac{v_p}{\pi c_0} \sin(T). \quad (3.26b)$$

Separating variables as in equation (2.30) and observing the time-independence of the boundary conditions one can easily deduce

$$\frac{\partial \Psi(0)}{\partial X} \eta(T) = -\frac{v_0}{\pi c_0}, \quad (3.27a)$$

$$\text{and } \frac{\partial \Psi(1)}{\partial X} \eta(T) = -\frac{v_l}{\pi c_0} + \frac{v_p}{\pi c_0} \sin(T). \quad (3.27b)$$

Equations (3.27) are substituted in the linear boundary terms of the weak form equation (3.14) while neglecting the nonlinear and dissipative boundary terms.

For the case of entirely driven resonators this yields the same system of equations in equation (3.18) with the same coefficient tensors in equations (3.19) except for the force terms in equation (3.19f) only at the boundary elements ($i \in \{1, nel\}$) which turn out to be

$$F_{j,1} = -\frac{l_1^e}{\Omega} \frac{dF}{dT} X_1 W_{j,1} - \frac{1}{\Omega^2 \pi^3 c_0} W_{j,1} v_0, \quad (3.28a)$$

$$\text{and } F_{j,nel} = -\frac{l_{nel}^e}{\Omega} \frac{dF}{dT} X_{nel} W_{j,nel} + \frac{1}{\Omega^2 \pi^3 c_0} W_{j,nel} v_l. \quad (3.28b)$$

For the case of piston driven resonators this yields the same system of equations in equation (3.18) with the same coefficient tensors in equations (3.23) except for the force terms in equation (3.23f) only at the boundary elements ($i \in \{1, nel\}$) which turn out to be

$$F_{j,1} = -\frac{1}{\Omega^2 \pi^3 c_0} W_{j,1} v_0, \quad (3.29a)$$

$$\text{and } F_{j,nel} = \frac{l_{nel}^e}{\Omega^2 \pi^3 c_0} W_{j,nel} (v_p \sin(T) + v_l). \quad (3.29b)$$

Furthermore, if the flow occurs from the whole boundary then in order to enforce continuity of the flow

$$v_l = \frac{S(0)}{S(1)} v_0 \quad (3.30)$$

which can be substituted in equation (3.28) to give the modified forcing for the boundary elements in entirely driven resonators

$$F_{j,1} \simeq -\frac{l_1^e}{\Omega} \frac{dF}{dT} X_1 W_{j,1} - \frac{1}{\Omega^2 \pi^3 c_0} W_{j,1} v_0, \quad (3.31a)$$

$$\text{and } F_{j,nel} \simeq -\frac{l_{nel}^e}{\Omega} \frac{dF}{dT} X_{nel} W_{j,nel} + \frac{1}{\Omega^2 \pi^3 c_0} W_{j,nel} \frac{S_1}{S_{nel}} v_0. \quad (3.31b)$$

and in equation (3.29) to give the modified forcing for the boundary elements in piston driven resonators

$$F_{j,1} \simeq -\frac{1}{\Omega^2 \pi^3 c_0} W_{j,1} v_0, \quad (3.32a)$$

$$\text{and } F_{j,nel} \simeq \frac{l_{nel}^e}{\Omega^2 \pi^3 c_0} W_{j,nel} \left(v_p \sin(T) + \frac{S_1}{S_{nel}} v_0 \right). \quad (3.32b)$$

3.5.2 Numerical Examples for Resonators with Flow

The effect of flow boundary conditions on pressure ratio is illustrated by two examples. In the first example, an exponential resonator is entirely driven with gas flowing at both ends. The resonator has a length of 0.224 m, $c = 330$ m/s, $D = 0.01$, $\gamma = 1.4$, with 10 modes under consideration $N = 10$. Gas is assumed to flow from both ends at different speeds, $v_0 = 0.001c_0$, $0.005c_0$, and $0.02c_0$. Figure 3.11 shows the predicted time history of the pressure ratio for each case. As expected, the pressure ratio decreases as the flow speed increases.

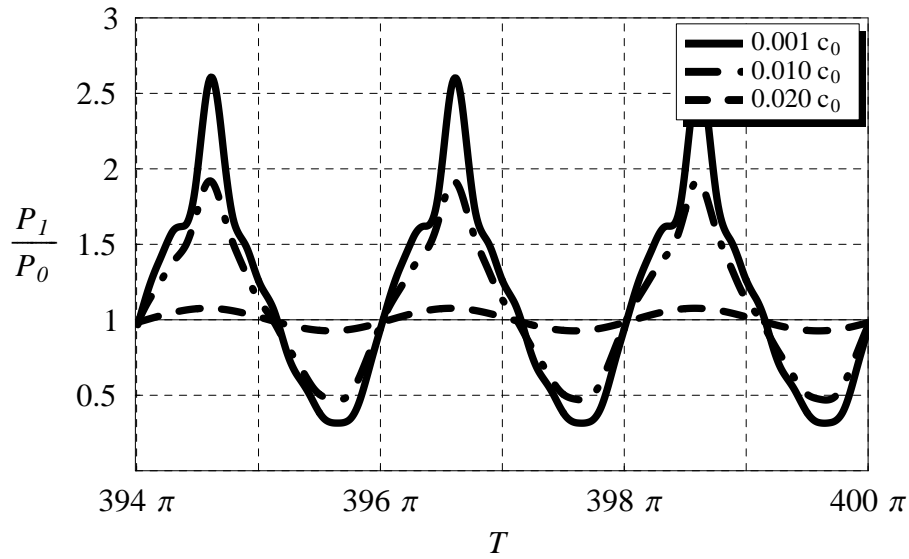


Figure 3.11: Pressure ratio predicted by the proposed finite element for an entirely driven exponential resonator, $\alpha = 5.75$, $l = 0.224$ m, $c = 330$ m/s, $D = 0.01$, $\gamma = 1.4$, and $N = 10$, under different flow boundary conditions, $v_0 = 0.001c_0, 0.010c_0$, and $0.020c_0$.

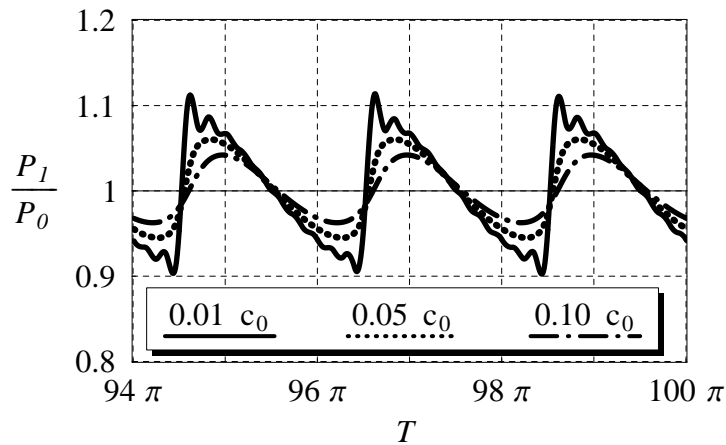


Figure 3.12: Pressure ratio predicted by the proposed finite element for a cylindrical resonator, $l = 0.165$ m, $c = 330$ m/s, $D = 0.01$, $\gamma = 1.4$, and $N = 10$, under different flow boundary conditions, $v_0 = 0.01c_0, 0.05c_0$, and $0.10c_0$.

In the second example, a cylindrical resonator is driven by an oscillating piston. Gas is allowed to flow at both ends. The resonator has a length of 0.165 m, $c = 330$ m/s, $D = 0.01$, $\gamma = 1.4$, with 10 modes under consideration $N = 10$. Gas is assumed to flow from both ends at different speeds, $v_0 = 0.01c_0, 0.05c_0$, and $0.10c_0$. Figure 3.12 shows the predicted time history of the pressure ratio for each case. Again, the pressure ratio decreases as the flow speed increases. It is noticed that higher flow speeds annihilate the formation of shock waves.

3.6 Summary

This chapter has presented the formulation of a finite element model of two types of acoustic resonators; the entirely and the piston driven resonators based on a weak integral form of the mathematical model developed in the previous chapter. The predictions of the finite element model for entirely driven resonators are compared to the corresponding predictions of analytical models for simple resonator geometries whose mode shapes are analytically known. The comparisons are established for cylindrical, exponential and linearly-varying area resonators. Excellent agreement is obtained between the predictions of the developed finite element and the analytical models. Such perfect match emphasizes the accuracy of the developed finite element model and its excellent potential in providing a reliable means for predicting the performance of resonators with more complex geometries. The developed finite element model has several advantages as compared to the analytical model. These advantages include

- being able to model resonators with any axisymmetric geometry including multi-segmented cavities in which each segment has an independent geometrical description and hence its ability of dealing with complicated resonator designs is increased,
- having a low computational cost since all integrals have been converted to discretized summations of simple functions over the elements. The computation time is independent of the complexity of the resonator geometry and is only a function in the number of elements and used modes,
- being based on the weak integral form which allowed incorporating the boundary conditions into the governing equations. Thus, being able to solve both entirely and piston driven resonators in a standard way without the need for selecting tricky basis and weight functions in which forcing is embedded,
- being able to model other cases of practical interest; namely axisymmetric resonators with flow across the boundaries.

External gas flow in both entirely and piston driven resonators has also been investigated. Modifications have been included in the finite element model to suit this type of boundary conditions. Numerical examples have also been presented for this case showing the dependence of the amplitude of the pressure ratio and its wave form on the amount of external flow.

Chapter 4

FEM of a Coupled Nonlinear

Model for Acoustic Resonators

Driven by Piezoelectric Bimorphs

4.1 Introduction

As mentioned in the literature survey, many researchers tried to build acoustic resonators to achieve high pressure ratios. While doing this they used powerful sources of excitations for their resonators; electromagnetic vibrators were used by Coppens and Sanders [5] and Temkin [6, 7], motor cycle engines by Lettau [4], Sturtevant [8] and Zaripov and Ilgamov [9], electrodynamic shakers by Saenger and Hudson [10], Cruikshank [11] and Lawrenson *et al.* [12], and mechanical generators by Merkli

and Thomann [13] and Althaus and Thomann [14]. The resulting resonators had to be too long to let the fundamental frequency fall into the range of the low operating frequencies of these drives. Lettau [4] for instance has used a 12 m long tube operated at 15 Hz.

One of the objectives of the study in hand is to replace the powerful sources of excitation that have been extensively used by previous researchers with compact, efficient, environment friendly drives. Piezoelectric bimorphs are excellent example of this category. Smits *et al.* [37] surveyed the applications of piezoelectric bimorphs. Recently, there has been some effort to study the sound radiation and mechanical-acoustic coupling for piezoelectric actuated beams as done by Chong *et al.* [38], and Nguyen and Pietrzko [39]. The implementation of axisymmetric piezoelectric bimorphs necessitates the integration of their dynamics into the cavity finite element model while retaining the nonlinearity of the gas equations. A good understanding of the interaction between the fluid and piezoelectric systems is also crucial to correctly predict the response of the system.

In this chapter, the model for the fluid oscillations in piston driven acoustic resonators will be quickly revisited and put in terms of the dimensional variables to construct the dimensional finite element model for the fluid system. Another model will be built for the piezoelectric bimorph to simulate its response to harmonic input voltage excitation. Both systems; fluid and piezoelectric will be collected in one global system. Discussing the mutual interaction of both systems determines how they are coupled together.

4.2 Basic Model of the Fluid System

The piston driven resonator shown in Figure 3.9 is considered. The gas inside is governed by the nonlinear second order cubic equation (2.25). First, the system modes are determined from the linearized unforced system.

4.2.1 Free Oscillations of the Fluid System

The free undamped linearized equation of the fluid system is

$$c_0^2 \left(\frac{1}{s} \frac{ds}{dx} \frac{\partial \varphi}{\partial x} + \frac{\partial^2 \varphi}{\partial x^2} \right) - \frac{\partial^2 \varphi}{\partial t^2} = 0 \quad (4.1)$$

where $\varphi(x, t)$ is the velocity function defined in equation (2.10). It can be sought of as a combination of two independent functions

$$\varphi(x, t) = \psi(x) \eta(t) \quad (4.2)$$

Equation (4.2) is substituted into equation (4.1), and then multiplied by an arbitrary weight function $W(x)$, integrated over the spatial domain to obtain the weighted residual form

$$\int_0^l W \left[c_0^2 \left(\frac{1}{s} \frac{ds}{dx} \frac{d\psi}{dx} \eta + \frac{d^2 \psi}{dx^2} \eta \right) - \psi \frac{d^2 \eta}{dt^2} \right] dx = 0 \quad (4.3)$$

The second order term is integrated by parts so that equation (4.3) yields the weak form of the free undamped linear system

$$\int_0^l \left[c_0^2 \left(W \frac{1}{s} \frac{ds}{dx} \frac{d\psi}{dx} \eta - \frac{dW}{dx} \frac{d\psi}{dx} \eta \right) - W \psi \frac{d^2 \eta}{dt^2} \right] dx + c_0^2 \left[W \frac{d\psi}{dx} \eta \right]_0^l = 0 \quad (4.4)$$

In order to simplify equation (4.4), the weighting function is chosen as weighted variations of the solution

$$W(x) = s(x)\delta\psi(x) \quad (4.5)$$

Therefore the weak form reduces to

$$\int_0^l \left(-c_0^2 s \frac{d\delta\psi}{dx} \frac{d\psi}{dx} \eta - s \delta\psi \psi \frac{d^2\eta}{dt^2} \right) dx + c_0^2 \left[s \delta\psi \frac{d\psi}{dx} \eta \right]_0^l = 0 \quad (4.6)$$

where $[\eta d\psi/dx]_0^l$ are the speeds at the boundaries which are zero at one side and some harmonic function with amplitude v_p at the other side

$$\frac{d\psi(0)}{dx} \eta = u(0) = 0, \quad (4.7a)$$

$$\text{and } \frac{d\psi(l)}{dx} \eta = u(l) = v_p \sin(\omega t). \quad (4.7b)$$

It is worth mentioning that for the basic fluid unforced system, the boundary term in equation (4.7b) should also vanish. However, it is kept in the equations such that when the fluid system gets coupled in a later stage with the piezoelectric system, this will be no more an external force and it has to be considered even in the free oscillations of the coupled system. Otherwise, the interaction between both systems will not be properly tracked.

For harmonic oscillations

$$\frac{d^2\eta}{dt^2} = -\omega^2\eta \quad (4.8)$$

which can be substituted in equation (4.6) to give

$$\int_0^l s \left(c_0^2 \frac{d\delta\psi}{dx} \frac{d\psi}{dx} - \omega^2 \delta\psi \psi \right) dx - c_0^2 s(l) \delta\psi(l) v_p = 0 \quad (4.9)$$

Equation (4.9) applies for the whole domain as well as a finite element of length l_f^e of a local coordinate ξ as shown in Figure (3.2). Within the element, ψ^e is approximated as

$$\psi^e = \mathbf{N}_f \cdot \mathbf{\Psi}^e \quad (4.10)$$

where \mathbf{N}_f are quadratic interpolation functions

$$\mathbf{N}_f(\xi) = \left\{ 1 - 3\xi + 2\xi^2 \quad 4\xi - 4\xi^2 \quad -\xi + 2\xi^2 \right\} \quad (4.11)$$

and $\mathbf{\Psi}^e$ are the nodal values of the mode within the element

$$\mathbf{\Psi}^e = \left\{ \psi_1^e \quad \psi_2^e \quad \psi_3^e \right\}^{\mathbf{T}} \quad (4.12)$$

where \mathbf{T} denotes the transpose of a vector or a matrix. The boundary terms within the elements need not to be worried about as they cancel out during the assembly. Therefore, using the approximation in equation (3.5) yields the following governing equation for the element

$$\delta \mathbf{\Psi}^e \cdot \int_0^1 s(\xi) \left(\frac{c_0^2}{l_f^e} \frac{d\mathbf{N}_f^{\mathbf{T}}}{d\xi} \frac{d\mathbf{N}_f}{d\xi} - \omega^2 \mathbf{N}_f^{\mathbf{T}} \mathbf{N}_f \right) (l_f^e d\xi) \cdot \mathbf{\Psi}^e = 0 \quad (4.13)$$

The weighting functions are arbitrary, and hence a system of equations is obtained for each element

$$(\mathbf{K}_f^e - \omega^2 \mathbf{M}_f^e) \cdot \mathbf{\Psi}^e = 0 \quad (4.14)$$

where \mathbf{K}_f^e is the fluid stiffness matrix

$$\mathbf{K}_f^e = \frac{1}{l_f^e} c_0^2 \int_0^1 s(\xi) \frac{d\mathbf{N}_f^{\mathbf{T}}}{d\xi} \frac{d\mathbf{N}_f}{d\xi} d\xi \quad (4.15)$$

and \mathbf{M}_f^e is the fluid mass matrix

$$\mathbf{M}_f^e = l_f^e \int_0^1 s(\xi) \mathbf{N}_f^T \mathbf{N}_f d\xi \quad (4.16)$$

The element mass and stiffness matrices are assembled in a global system of equations to be solved for the natural frequencies ω_n and mode shapes Ψ_n of the fluid system. Only the first N modes are of concern while the higher ones are truncated.

4.2.2 Nonlinear Forced Oscillations of the Fluid System

The velocity potential can now be approximated as the sum of N mode shapes, with corresponding time-dependant amplitudes.

$$\varphi(x, t) = \psi_n(x) \eta_n(t) \quad (4.17)$$

where index notation is being used again with $n = 1, 2, \dots, N$. Equation (4.17) is substituted in equation (2.25) which fully describes the nonlinear behavior of the gas oscillations in the resonator to give

$$\begin{aligned} & \psi_n \frac{d^2 \eta_n}{dt^2} - \frac{c_0^2}{s} \frac{d}{dx} \left(s \frac{d\psi_n}{dx} \right) \eta_n - \frac{\delta}{s} \frac{d}{dx} \left(s \frac{d\psi_n}{dx} \right) \frac{d\eta_n}{dt} + 2 \frac{d\psi_n}{dx} \frac{d\psi_m}{dx} \frac{d\eta_n}{dt} \eta_m \\ & + \frac{\gamma - 1}{s} \psi_n \frac{d\eta_n}{dt} \frac{d}{dx} \left(s \frac{d\psi_m}{dx} \right) \eta_m + \frac{1}{3} \frac{d}{dx} \left(\frac{d\psi_n}{dx} \frac{d\psi_m}{dx} \frac{d\psi_p}{dx} \right) \eta_n \eta_m \eta_p \\ & + \frac{\gamma - 1}{2s} \left(\frac{d\psi_n}{dx} \frac{d\psi_m}{dx} \right) \frac{d}{dx} \left(s \frac{d\psi_n}{dx} \right) \eta_n \eta_m \eta_p = 0 \end{aligned} \quad (4.18)$$

where the body driving acceleration $a(t)$ is substituted by zero. The weighted residual form is obtained by multiplying equation (4.18) by a weighting function $W(x)$ and

integrating over the whole length

$$\begin{aligned}
& \int_0^l W_j \psi_n dx \frac{d^2 \eta_n}{dt^2} - \int_0^l \frac{c_0^2}{s} W_j \frac{d}{dx} \left(s \frac{d\psi_n}{dx} \right) dx \cdot \eta_n - \int_0^l \frac{\delta}{s} W_j \frac{d}{dx} \left(s \frac{d\psi_n}{dx} \right) dx \frac{d\eta_n}{dt} \\
& + 2 \int_0^l W_j \frac{d\psi_n}{dx} \frac{d\psi_m}{dx} dx \frac{d\eta_n}{dt} \eta_m + \int_0^l \frac{\gamma - 1}{s} W_j \psi_n \frac{d}{dx} \left(s \frac{d\psi_m}{dx} \right) dx \cdot \frac{d\eta_n}{dt} \eta_m + \\
& \int_0^l W_j \left[\frac{1}{3} \frac{d}{dx} \left(\frac{d\psi_n}{dx} \frac{d\psi_m}{dx} \frac{d\psi_p}{dx} \right) + \frac{\gamma - 1}{2s} \frac{d\psi_n}{dx} \frac{d\psi_m}{dx} \frac{d}{dx} \left(s \frac{d\psi_p}{dx} \right) \right] dx \cdot \eta_n \eta_m \eta_p = 0
\end{aligned} \tag{4.19}$$

The weighting functions are chosen as

$$W_j(x) = s(x)\psi_j(x) \tag{4.20}$$

Integration by parts is carried out for second order derivatives to give the weighted residual form for the nonlinear oscillations of the fluid system

$$\begin{aligned}
& \int_0^l s \psi_j \psi_n dx \frac{d^2 \eta_n}{dt^2} + c_0^2 \int_0^l s \frac{d\psi_j}{dx} \frac{d\psi_n}{dx} dx \cdot \eta_n + 2 \int_0^l s \psi_j \frac{d\psi_n}{dx} \frac{d\psi_m}{dx} dx \frac{d\eta_n}{dt} \eta_m \\
& - (\gamma - 1) \int_0^l s \frac{d}{dx} (\psi_j \psi_n) \frac{d\psi_m}{dx} dx \frac{d\eta_n}{dt} \eta_m + \delta \int_0^l s \frac{d\psi_j}{dx} \frac{d\psi_n}{dx} dx \frac{d\eta_n}{dt} + \\
& \int_0^l \left[\frac{1}{3} \frac{d}{dx} (s \psi_j) \frac{d\psi_n}{dx} \frac{d\psi_m}{dx} \frac{d\psi_p}{dx} + \frac{\gamma - 1}{2} s \frac{d}{dx} \left(\psi_j \frac{d\psi_n}{dx} \frac{d\psi_m}{dx} \right) \frac{d\psi_p}{dx} \right] dx \cdot \eta_n \eta_m \eta_p \\
& - c_0^2 s(l) \psi_j(l) v_p \sin(\omega t) = 0
\end{aligned} \tag{4.21}$$

where the boundary terms that arise from the dissipative, quadratic and cubic terms are neglected. The only significant boundary term is the linear one which is directly substituted by zero speed at $x = 0$, and the piston speed at $x = l$.

Again, the domain is divided into finite elements as the one shown in Figure 3.2 so that the integrations can be replaced by simple summations over the elements.

Hence equation (4.21) can be put in the following compact form

$$A_{jn} \frac{d^2 \eta_n}{dT^2} + B_{jn} \eta_n + C_{jnm} \frac{d\eta_n}{dT} \eta_m + D_{jn} \frac{d\eta_n}{dT} + E_{jnmp} \eta_n \eta_m \eta_p = F_j \quad (4.22)$$

where

$$A_{jn} = l_f^e s_i \Psi_{ji} \Psi_{ni} = \mathbf{\Psi}_j^T \cdot \mathbf{M}_f \cdot \mathbf{\Psi}_n, \quad (4.23a)$$

$$B_{jn} = c_0^2 l_f^e s_i \frac{d\Psi_{ji}}{dx} \frac{d\Psi_{ni}}{dx} = \mathbf{\Psi}_j^T \cdot \mathbf{K}_f \cdot \mathbf{\Psi}_n, \quad (4.23b)$$

$$C_{jnm} = l_f^e s_i \left[(3 - \gamma) \Psi_{ji} \frac{d\Psi_{ni}}{dx} - (\gamma - 1) \frac{d\Psi_{ji}}{dx} \Psi_{ni} \right] \frac{d\Psi_{mi}}{dx}, \quad (4.23c)$$

$$D_{jn} = \delta l_f^e s_i \frac{d\Psi_{ji}}{dx} \frac{d\Psi_{ni}}{dx} = \frac{\delta}{c_0^2} B_{jn}, \quad (4.23d)$$

$$E_{jnmp} = \frac{1}{3} l_f^e \frac{d}{dx} (s_i \Psi_{ji}) \frac{d\Psi_{ni}}{dx} \frac{d\Psi_{mi}}{dx} \frac{d\Psi_{pi}}{dx} + \frac{\gamma - 1}{2} l_f^e s_i \frac{d}{dx} \left(\Psi_{ji} \frac{d\Psi_{ni}}{dx} \frac{d\Psi_{mi}}{dx} \right) \frac{d\Psi_{pi}}{dx}, \quad (4.23e)$$

$$\text{and } F_j = c_0^2 s(l) \psi_j(l) v_p \sin(\omega t). \quad (4.23f)$$

Equation (4.22) represents a system of N second order ordinary differential equations with linear, quadratic and cubic terms, besides the harmonic excitation. The N unknown functions $\eta_n(t)$ are evaluated by numerical integration and hence can be substituted in equation (4.17) to find the velocity potential function which in turn can be used to evaluate other variables of interest and most importantly the pressure ratio

$$\frac{p}{p_0} = \left[1 - \frac{(\gamma - 1)}{c_0^2} \left(\frac{\partial \varphi}{\partial t} + \frac{1}{2} \left(\frac{\partial \varphi}{\partial x} \right)^2 - \delta \frac{\partial^2 \varphi}{\partial x^2} \right) \right]^{\gamma/(\gamma - 1)} \quad (4.24)$$

4.2.3 Fluid Flow Across the Boundaries of the Resonator

Figure 3.10 shows two valves mounted to the ends of the resonator. The boundary conditions for this case are those shown in equation (3.25). These can be substituted in the weak form boundary terms to yield the same coefficient tensors as in equations (4.23) except for (4.23f) which turns out to be

$$F_j = c_0^2 s(l) \psi_j(l) (v_p \sin(\omega t) - v_l) + c_0^2 s(0) \psi_j(0) v_0 \quad (4.25)$$

If the density variations between the ends are neglected, then the continuity of flow necessitates that $v_0 s(0) = v_l s(l)$ yielding

$$F_j = c_0^2 s(l) [\psi_j(l) v_p \sin(\omega t) - (\psi_j(l) - \psi_j(0)) v_l] \quad (4.26)$$

4.3 Piezoelectric Bimorph Actuators

The theory of piezoelectric axisymmetric bimorphs is well presented by Dobrucki and Pruchnicki [40]. Based on their theory, the equations for a flat axisymmetric piezoelectric bimorph which is shown in Figure 4.1 will be developed. The bimorph is aligned to the x -axis and consists of nl layers. $h_i, \rho_i, E_i, \nu_i, r_i^{in}, r_i^{out}$, and U_i denote the axial location, density, modulus of elasticity, poisson's ratio, inner radius, outer radius and the electric potential of the i^{th} layer, respectively.

Figure 4.2 shows a two-node element extending from r_1^e to r_2^e in the physical coordinate or 0 and 1 in the local χ coordinate. The element length is $l_p^e = r_2^e - r_1^e$.

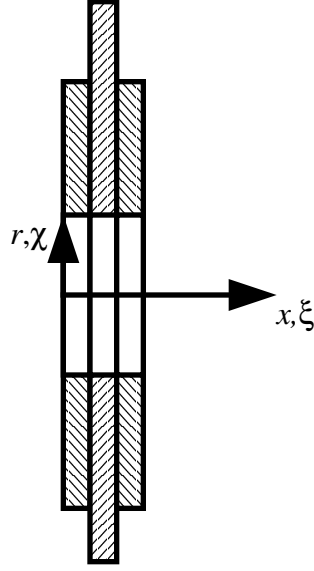


Figure 4.1: **Schematic for a three layer piezoelectric bimorph**

The vector of element degrees of freedom is

$$\mathbf{u}^e = \left\{ u_{r_1} \quad \frac{du_r}{dr} \Big|_{r_1} \quad u_{x_1} \quad \frac{du_x}{dr} \Big|_{r_1} \quad u_{r_2} \quad \frac{du_r}{dr} \Big|_{r_2} \quad u_{x_2} \quad \frac{du_x}{dr} \Big|_{r_2} \right\}^T \quad (4.27)$$

The radial and axial displacements within the element can be approximated by using the vector of element degrees of freedom and Hermite interpolation functions

$$\begin{Bmatrix} u_r \\ u_x \end{Bmatrix} = \mathbf{N}^e \mathbf{u}^e \quad (4.28)$$

where

$$\mathbf{N}^e = \begin{bmatrix} N_1 & l_p^e N_3 & 0 & 0 & N_2 & l_p^e N_4 & 0 & 0 \\ 0 & 0 & N_1 & l_p^e N_3 & 0 & 0 & N_2 & l_p^e N_4 \end{bmatrix} \quad (4.29)$$

and

$$\{N_i\} = \left\{ 2\chi^3 - 3\chi^2 + 1 \quad -2\chi^3 + 3\chi^2 \quad \chi^3 - 2\chi^2 + \chi \quad \chi^3 - 3\chi^2 \right\} \quad (4.30)$$

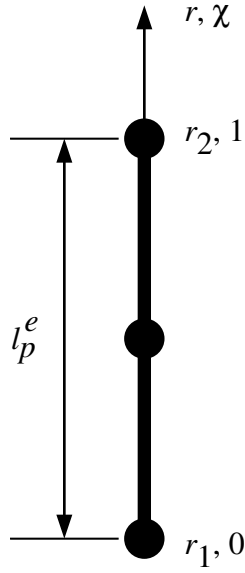


Figure 4.2: **Schematic for a two-node piezoelectric element**

Within the element, the radial and axial positions can be expressed as

$$r(\chi) = r_1^e + l_p^e \chi \quad (4.31)$$

The extensional and flexural stress and strain vectors within the element are denoted by σ and ε . The stress-strain relationship is

$$\sigma = \begin{bmatrix} d_{11} & d_{12} & k_{11} & k_{12} \\ d_{21} & d_{22} & k_{21} & k_{22} \\ k_{11} & k_{12} & b_{11} & b_{12} \\ k_{21} & k_{22} & b_{21} & b_{22} \end{bmatrix} \varepsilon = \mathbf{D}^e \varepsilon \quad (4.32)$$

The extensional stiffnesses d_{ij} are evaluated as

$$\begin{aligned} d_{11} = d_{22} &= \sum_{i=1}^{nl} \frac{E_i}{1-\nu_i^2} (h_i - h_{i-1}), \\ d_{12} = d_{21} &= \sum_{i=1}^{nl} \frac{\nu_i E_i}{1-\nu_i^2} (h_i - h_{i-1}) \end{aligned} \quad (4.33)$$

while the coupling stiffnesses k_{ij} are evaluated as

$$\begin{aligned} k_{11} = k_{22} &= \sum_{i=1}^{nl} \frac{E_i}{1-\nu_i^2} \left(\frac{h_i^2 - h_{i-1}^2}{2} - \zeta_0 \frac{h_i - h_{i-1}}{2} \right), \\ k_{12} = k_{21} &= \sum_{i=1}^{nl} \frac{\nu_i E_i}{1-\nu_i^2} \left(\frac{h_i^2 - h_{i-1}^2}{2} - \zeta_0 \frac{h_i - h_{i-1}}{2} \right) \end{aligned} \quad (4.34)$$

and the flexural stiffnesses b_{ij} are evaluated as

$$\begin{aligned} b_{11} = b_{22} &= \sum_{i=1}^{nl} \frac{E_i}{1-\nu_i^2} \left(\frac{h_i^3 - h_{i-1}^3}{3} - \zeta_0 (h_i^2 - h_{i-1}^2) + \zeta_0^2 (h_i - h_{i-1}) \right), \\ b_{12} = b_{21} &= \sum_{i=1}^{nl} \frac{\nu_i E_i}{1-\nu_i^2} \left[\frac{h_i^3 - h_{i-1}^3}{3} - \zeta_0 (h_i^2 - h_{i-1}^2) + \zeta_0^2 (h_i - h_{i-1}) \right] \end{aligned} \quad (4.35)$$

where $h_0 = 0$ and

$$\zeta_0 = \frac{1}{2} \frac{\sum_{i=1}^{nl} \frac{E_i}{1-\nu_i^2} (h_i^2 - h_{i-1}^2)}{\sum_{i=1}^{nl} \frac{E_i}{1-\nu_i^2} (h_i - h_{i-1})} \quad (4.36)$$

The strain-displacement relationship as defined in Flügge [41]

$$\varepsilon = \mathbf{W}^e \begin{Bmatrix} u_r \\ u_x \end{Bmatrix} \quad (4.37)$$

where

$$\mathbf{W}^e = \begin{bmatrix} \frac{1}{l_p^e} \frac{\partial}{\partial \chi} & 0 \\ \frac{1}{r} & 0 \\ 0 & \frac{1}{l_p^e} \frac{\partial^2}{\partial \chi^2} \\ 0 & \frac{1}{l_p^e r} \frac{\partial}{\partial \chi} \end{bmatrix} \quad (4.38)$$

The free $\frac{\partial}{\partial \chi}$ is a differential operator that operates on whatever gets multiplied to the term including it. The radial and axial displacements are approximated as in

equation (4.28). Therefore

$$\varepsilon = \mathbf{W}^e \cdot \mathbf{N}^e \mathbf{u}^e = \mathbf{B}^e \mathbf{u}^e \quad (4.39)$$

where

$$\mathbf{B}^e = \begin{bmatrix} \frac{1}{l_p^e} \frac{dN_1}{d\chi} & \frac{dN_3}{d\chi} & 0 & 0 & \frac{1}{l_p^e} \frac{dN_2}{d\chi} & \frac{dN_4}{d\chi} & 0 & 0 \\ \frac{N_1}{r} & l_p^e \frac{N_3}{r} & 0 & 0 & \frac{N_2}{r} & l_p^e \frac{N_4}{r} & 0 & 0 \\ 0 & 0 & \frac{1}{l_p^{e2}} \frac{d^2 N_1}{d\chi^2} & \frac{1}{l_e} \frac{d^2 N_3}{d\chi^2} & 0 & 0 & \frac{1}{l_p^{e2}} \frac{d^2 N_2}{d\chi^2} & \frac{1}{l_p^e} \frac{d^2 N_4}{d\chi^2} \\ 0 & 0 & \frac{1}{l_p^e r} \frac{dN_1}{d\chi} & \frac{1}{r} \frac{dN_3}{d\chi} & 0 & 0 & \frac{1}{l_p^e r} \frac{dN_2}{d\chi} & \frac{1}{r} \frac{dN_4}{d\chi} \end{bmatrix} \quad (4.40)$$

The potential energy U^e of an element is

$$U^e = \frac{1}{2} \int_{s^e} \varepsilon^{\mathbf{T}} \cdot \sigma ds^e = \pi l^e \int_{s^e} r(\chi) \varepsilon^{\mathbf{T}} \cdot \sigma d\chi \quad (4.41)$$

The stress-strain relationship in equation (4.32) and strain-displacement relationship in equation (4.37) are substituted in the potential energy equation (4.41) to give

$$U^e = \pi l_p^e \mathbf{u}^{e\mathbf{T}} \int_0^1 r(\chi) \mathbf{B}^{e\mathbf{T}} \mathbf{D}^e \mathbf{B}^e d\chi \cdot \mathbf{u}^e \quad (4.42)$$

or

$$U^e = \frac{1}{2} \mathbf{u}^{e\mathbf{T}} \mathbf{K}_p^e \mathbf{u}^e \quad (4.43)$$

where \mathbf{K}_p^e is the 8×8 piezoelectric element stiffness matrix defined by

$$\mathbf{K}_p^e = 2\pi \cdot l_p^e \int_0^1 r(\chi) \mathbf{B}^{e\mathbf{T}} \mathbf{D}^e \mathbf{B}^e d\chi \quad (4.44)$$

The kinetic energy T^e of the same element is calculated as

$$T^e = \frac{1}{2} \rho_e \int_{s^e} \left[\left(\frac{\partial u_r}{\partial t} \right)^2 + \left(\frac{\partial u_x}{\partial t} \right)^2 \right] \cdot ds^e \quad (4.45)$$

where

$$\rho_e = \sum_{i=1}^{nl} \rho_i (h_i - h_{i-1}) \quad (4.46)$$

is the mass per unit area of the element. Equation (4.28) is substituted in the element kinetic energy in equation (4.45) to give

$$T^e = \pi \cdot l_p^e \rho_e \frac{\partial \mathbf{u}^e \mathbf{T}}{\partial t} \int_0^1 r(\chi) \mathbf{N}^{e\mathbf{T}} \mathbf{N}^e d\chi \cdot \frac{\partial \mathbf{u}^e}{\partial t} \quad (4.47)$$

or

$$T^e = \frac{1}{2} \frac{\partial \mathbf{u}^e \mathbf{T}}{\partial t} \mathbf{M}_p^e \frac{\partial \mathbf{u}^e}{\partial t} \quad (4.48)$$

where \mathbf{M}_p^e is the 8×8 piezoelectric element mass matrix defined by

$$\mathbf{M}_p^e = 2\pi l_p^e \rho_e \int_0^1 r(\chi) \mathbf{N}^{e\mathbf{T}} \mathbf{N}^e d\chi \quad (4.49)$$

The work done by the external acoustic pressure on an element is

$$L^e = \int_{s^e} p \left\{ \begin{array}{cc} 1 & 1 \end{array} \right\} \cdot \left\{ \begin{array}{c} u_r \\ u_x \end{array} \right\} ds^e \quad (4.50)$$

where the acoustic pressure is assumed uniform all over the element. Substituting the approximation in equation (4.28), one gets the element force vector due to acoustic pressure

$$\mathbf{F}_{p1}^e = 2\pi p \int_0^1 \left\{ \begin{array}{cc} 1 & 1 \end{array} \right\} \cdot \mathbf{N}^e r(\chi) d\chi \quad (4.51)$$

The element matrices are assembled in global matrices and substituted in the equation of motion.

$$\mathbf{K}_p \mathbf{u} + \mathbf{M}_p \frac{\partial^2 \mathbf{u}}{\partial t^2} = \mathbf{F}_{p1} \quad (4.52)$$

For a harmonic motion

$$\frac{\partial^2 \mathbf{u}}{\partial t^2} = -\omega^2 \mathbf{u} \quad (4.53)$$

Therefore

$$\mathbf{K}_p \mathbf{u} - \omega^2 \mathbf{M}_p \mathbf{u} = \mathbf{F}_{p1} \quad (4.54)$$

The effect of piezoelectricity comes within another force vector F_{p2} at the nodes corresponding to the inner and outer radii, r^{in} and r^{out} of the bimorph.

$$\mathbf{F}_{p2}^e = 2\pi r^e \left\{ \begin{array}{c} \sum_{i=1}^{nl} e_{31i} U_i \\ 0 \\ 0 \\ - \sum_{i=1}^{nl} e_{31i} U_i \left(\frac{h_i + h_{i-1}}{2} - \zeta_0 \right) \end{array} \right\} \quad (4.55)$$

where e_{31i} is the piezoelectric constant of the i^{th} layer as defined in Kalinichev et al [42], and e is either for the innermost element (element number 1) or outermost one (element number nel_p). For a bimorph that is symmetric about its mid plane, the first element of will always vanish.

The governing equation for the forced piezoelectric system is

$$\mathbf{K}_p \mathbf{u} - \omega^2 \mathbf{M}_p \mathbf{u} = \mathbf{F}_{p1} + \mathbf{F}_{p2} \quad (4.56)$$

4.4 Combining and Coupling the Fluid and Piezoelectric Actuator Models

The piezoelectric bimorph is used to excite the gas inside an axisymmetric resonator like the one shown in Figure 3.9. The acoustic pressure that is developed due to the formation of the standing wave certainly affects the dynamics of the actuator and vice versa. In this section, this interaction will be investigated on two steps. In the first both the fluid and the piezoelectric models will be combined in one global model, while in the second the coupling will be included by analyzing the effect of one system on the other.

4.4.1 Combined System

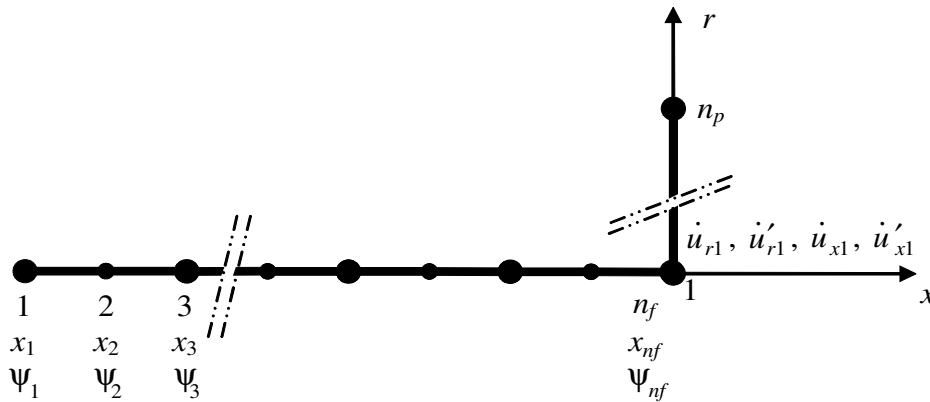


Figure 4.3: Schematic of a finite element mesh combining both the piezoelectric and acoustic finite element meshes.

The finite element mesh for the combined system is shown in Figure 4.3. The system consists of nel_f three-node acoustic elements aligned to the x -axis with one degree of freedom per node, and nel_p two-node piezoelectric elements aligned to the r -axis with four degrees of freedom per node; two velocity components and their spatial derivatives. Velocity degrees of freedom are chosen instead of the displacement ones that were used in developing the finite element model for piezoelectric bimorphs in section 4.3 to be compatible with the degrees of freedom of the velocity potential functions in the fluid system. There are n_f fluid nodes and n_p piezoelectric nodes. The first node of the piezoelectric elements coincides to the last one of the acoustic elements. Having this combined mesh, one can search for the natural modes of the combined system. In order to do so, it is desired to have a system of equations of the following format

$$(\mathbf{K} - \omega^2 \mathbf{M}) \mathbf{q} = \mathbf{0} \quad (4.57)$$

where \mathbf{K} is the global stiffness matrix

$$\mathbf{K} = \begin{bmatrix} \mathbf{K}_f & \mathbf{0} \\ \mathbf{0} & \mathbf{K}_p \end{bmatrix} \quad (4.58)$$

and \mathbf{M} is the global mass matrices

$$\mathbf{M} = \begin{bmatrix} \mathbf{M}_f & \mathbf{0} \\ \mathbf{0} & \mathbf{M}_p \end{bmatrix} \quad (4.59)$$

and \mathbf{q} is the vector of all degrees of freedom in the system, i.e.

$$\mathbf{q} = \begin{Bmatrix} \Phi(\mathbf{x}, t) \\ \dot{\mathbf{u}}(\mathbf{x}, t) \end{Bmatrix} = \begin{Bmatrix} \Psi(\mathbf{x})\eta(t) \\ \mathbf{U}(\mathbf{x})\eta(t) \end{Bmatrix} = \begin{Bmatrix} \Psi(\mathbf{x}) \\ \mathbf{U}(\mathbf{x}) \end{Bmatrix} \eta(t) \quad (4.60)$$

where Ψ again is the vector of nodal values of the space dependent function of the fluid velocity potential function and \mathbf{U} is the vector of nodal values of the space dependent function of the piezoelectric velocity and its spatial derivative.

In the definitions for the global stiffness and mass matrices in equations (4.58) and (4.59), \mathbf{K}_f and \mathbf{M}_f are themselves to be populated with the individual fluid element stiffness and mass matrices as defined in equations (4.15) and (4.16), while \mathbf{K}_p and \mathbf{M}_p are to be populated with piezoelectric element stiffness and mass matrices as defined in equations (4.44) and (4.49). In the previous definitions, the coupling has not yet been added.

4.4.2 Coupled System

Equation (4.9) shows the effect of the piston speed on the mode shapes. The piston speed is nothing but the \dot{u}_x component of the first piezoelectric node. Therefore,

$$v_p = \dot{u}_{x_1} \quad (4.61)$$

In order to show the effect of the fluid system on the actuator we first differentiate the force vector in equation (4.51) and the equation of motion (4.54) with respect to

time. The former gives

$$\frac{\partial \mathbf{F}_{p1}}{\partial t} = 2\pi \frac{\partial p}{\partial t} \int_0^1 \left\{ \begin{array}{cc} 1 & 1 \end{array} \right\} \cdot \mathbf{N}^e r(\chi) d\chi \quad (4.62)$$

while the latter yields

$$(\mathbf{K}_p - \omega^2 \mathbf{M}_p) \frac{\partial \mathbf{u}}{\partial t} = \frac{\partial \mathbf{F}_{p1}}{\partial t} \quad (4.63)$$

Then, equation (4.62) is substituted in (4.63) to give

$$(\mathbf{K}_p - \omega^2 \mathbf{M}_p) \frac{\partial \mathbf{u}}{\partial t} - 2\pi \frac{\partial p}{\partial t} \int_0^1 \left\{ \begin{array}{cc} 1 & 1 \end{array} \right\} \cdot \mathbf{N}^e r(\chi) d\chi = 0 \quad (4.64)$$

At this point, we borrow the following relation from the linear acoustic theory

$$\frac{\partial p}{\partial t} + \rho_0 c_0^2 \varphi = 0 \quad (4.65)$$

which can be substituted in (4.64) to yield

$$(\mathbf{K}_p^e - \omega^2 \mathbf{M}_p^e) \frac{\partial \mathbf{u}}{\partial t} - 2\pi \rho_0 c_0^2 \varphi_{nf} \int_0^1 \left\{ \begin{array}{cc} 1 & 1 \end{array} \right\} \cdot \mathbf{N}^e r(\chi) d\chi = 0 \quad (4.66)$$

Therefore, the coupled system has a global system of equations which looks like

$$\left(\left[\begin{array}{cc} \mathbf{K}_f & \mathbf{C}_f \\ \mathbf{C}_p & \mathbf{K}_p \end{array} \right] - \omega^2 \left[\begin{array}{cc} \mathbf{M}_f & \mathbf{0} \\ \mathbf{0} & \mathbf{M}_p \end{array} \right] \right) \cdot \left\{ \begin{array}{c} \Psi \\ \mathbf{U} \end{array} \right\} = \left\{ \begin{array}{c} \mathbf{0} \\ \mathbf{0} \end{array} \right\} \quad (4.67)$$

where \mathbf{C}_f and \mathbf{C}_p are the coupling matrices. The former is a null matrix except for the entry corresponding to the Ψ_{nf} and \dot{u}_{x_1} degrees of freedom which is filled according

to equation (4.9)

$$\mathbf{C}_f = -c_0^2 * s(l)\psi_j(l) \begin{bmatrix} 0 & 0 & 0 & 0 & 0 \\ \vdots & \vdots & \vdots & \ddots & 0 \\ 0 & 0 & 0 & \dots & 0 \\ 0 & 0 & 0 & \dots & 0 \\ 0 & 0 & 1 & \dots & 0 \end{bmatrix} \quad (4.68)$$

while the latter is also a null matrix except for the column corresponding to the Ψ_{nf} degree of freedom which is evaluated from the integral term in equation (4.63)

$$\mathbf{C}_p = 2\pi\rho_0c_0^2 \begin{bmatrix} 0 & 0 & 0 & 0 & \int_0^1 \left\{ \begin{matrix} 1 & 1 \end{matrix} \right\} \cdot \mathbf{N}^{1r}(\chi) d\chi \\ \vdots & \vdots & \vdots & \vdots & \vdots \\ \vdots & \vdots & \vdots & \vdots & \vdots \\ \vdots & \vdots & \vdots & \vdots & \vdots \\ 0 & 0 & 0 & 0 & \int_0^1 \left\{ \begin{matrix} 1 & 1 \end{matrix} \right\} \cdot \mathbf{N}^{nelp_r}(\chi) d\chi \end{bmatrix} \quad (4.69)$$

Equation (4.67) can now be used to extract the eigenvalues and eigenvectors of the coupled system which can be used later on to express the response of the system to external excitations in terms of the system mode shapes.

4.4.3 Forced Oscillations of the Coupled System

The coupled system includes two governing equations; equation (4.21) for the fluid system, and equation (4.56) for the piezoelectric system. The boundary term in the former contributes to the coupling between both systems. In the latter the first

forcing vector \mathbf{F}_{p1} also contributes to the coupling, while the second forcing term \mathbf{F}_{p2} is the source of external excitation. The coupled system equations are again written in the compact form of equation (4.22). Since the piezoelectric bimorph is assumed to behave in a linear fashion, its inertia and stiffness contribute only to the coefficient tensors of the linear terms. Therefore the definitions of the coefficient tensors for the case of axisymmetric acoustic resonators driven by piezoelectric bimorphs is as follows

$$A_{jn} = \Psi_j^T \mathbf{M}_f \Psi_n + \mathbf{U}_j^T \mathbf{M}_p \mathbf{U}_n, \quad (4.70a)$$

$$B_{jn} = \Psi_j^T \mathbf{K}_f \Psi_n + \mathbf{U}_j^T \mathbf{K}_p \mathbf{U}_n \quad (4.70b)$$

$$+ \Psi_j^T \mathbf{C}_f \mathbf{U}_n + \mathbf{U}_j^T \mathbf{C}_p \Psi_n,$$

$$C_{jnm} = l_f^e s_i \left[(3 - \gamma) \Psi_{ji} \frac{d\Psi_{ni}}{dx} - (\gamma - 1) \frac{d\Psi_{ji}}{dx} \Psi_{ni} \right] \frac{d\Psi_{mi}}{dx}, \quad (4.70c)$$

$$D_{jn} = \delta l_f^e s_i \frac{d\Psi_{ji}}{dx} \frac{d\Psi_{ni}}{dx} = \frac{\delta}{c_0^2} B_{jn}, \quad (4.70d)$$

$$E_{jnmp} = \frac{1}{3} l_f^e \frac{d}{dx} (s_i \Psi_{ji}) \frac{d\Psi_{ni}}{dx} \frac{d\Psi_{mi}}{dx} \frac{d\Psi_{pi}}{dx} \quad (4.70e)$$

$$+ \frac{\gamma - 1}{2} l_f^e s_i \frac{d}{dx} \left(\Psi_{ji} \frac{d\Psi_{ni}}{dx} \frac{d\Psi_{mi}}{dx} \right) \frac{d\Psi_{pi}}{dx},$$

$$\text{and } F_j = \mathbf{U}_j^T \cdot \frac{\partial}{\partial t} (\mathbf{F}_{p2}^e). \quad (4.70f)$$

4.5 Evaluation of the Coupled System Model

The equations developed in section 4.4 are used to model the coupled behavior of axisymmetric resonators driven by piezoelectric bimorphs. The boundary conditions for the coupled system include zero velocity potential far from the piston side, zero displacement of the node at the rim of the piezoelectric bimorph, besides zero radial displacement and its derivative at the inner radius of the bimorph due to symmetry.

4.5.1 Uncoupled Vs. Coupled Systems

Figure 4.4 shows an example of an axisymmetric resonator of total length 0.25 m. The resonator is filled with air, $\rho_0 = 1.25 \text{ kg/m}^3$, $\gamma = 1.4$, $\delta/c_0^2 = 0.05\text{s}$, and excited with a piezoelectric bimorph whose dimensions and properties are given in Table 4.1.

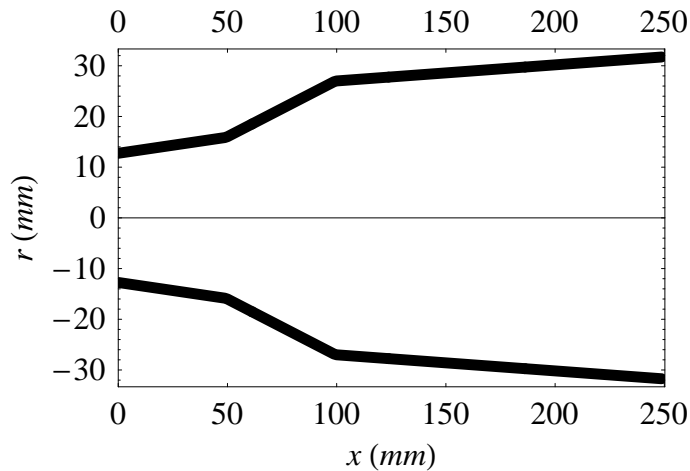


Figure 4.4: **Schematic of the axisymmetric resonator used in evaluating the coupled system model.**

Figure 4.5 shows the first four mode shapes of the uncoupled model in which

Table 4.1: **Physical, mechanical and electrical properties of a 2.5” piezoelectric bimorph.**

	Piezoelectric	Shim
No. of layers	2	1
Diameter (mm)	63.5	63.5
Thickness (mm)	0.19	0.03
Material	PZT-5A	Brass
Density (Kg/m ³)	7750	8500
Elasticity Modulus (GPa)	52	100
Poisson’s ratio	0.3	0.34
Piezoelectric constant (N/V/m)	15.8	–
Dielectric Relative Permittivity	3300	–

the first and fourth are structural modes while the second and third are acoustic ones. Figure 4.6 shows the same model with the coupling activated. All four modes are coupled, and the natural frequencies are quite far from those predicted without coupling which shows the importance of using a coupled system model for the accurate prediction of the system performance.

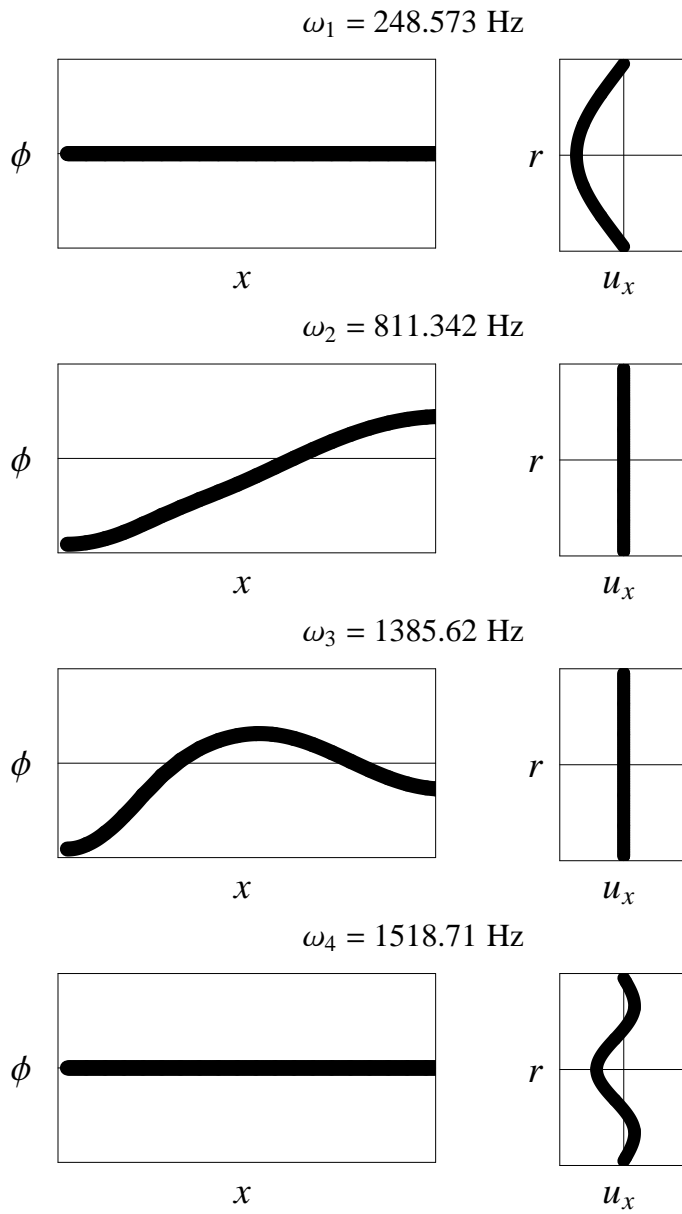


Figure 4.5: Mode shapes of the uncoupled system model.

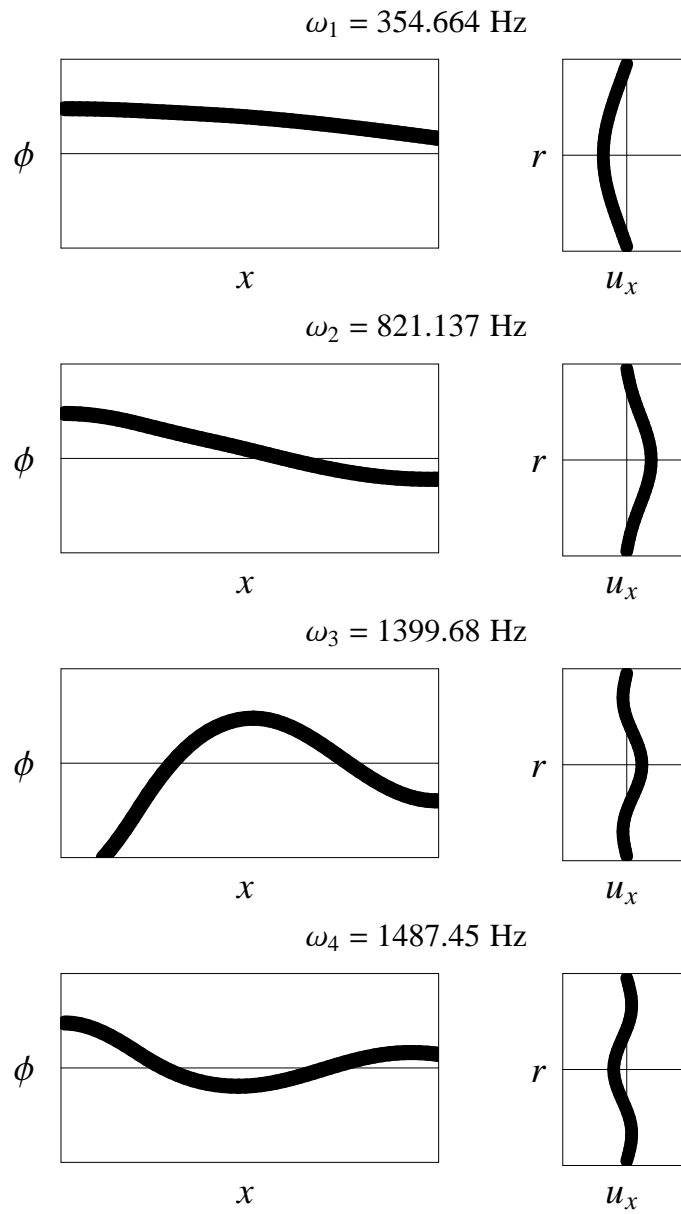


Figure 4.6: Mode shapes of the coupled system model.

4.5.2 Actuated Piezoelectric Driven Resonators and Geometry Optimization

Figure 4.7 shows a 0.5 m long axisymmetric resonator filled with air, $\rho_0 = 1.25$ kg/m³, $\gamma = 1.4$, $\delta/c_0^2 = 0.05$ s, and excited with a piezoelectric bimorph whose dimensions and properties are given in Table 4.1. The mode shapes are extracted and then substituted in the proposed model to calculate the response of the system to external excitation as described in section 4.4.

Figure 4.8 shows the pressure wave expected at the small end when the bimorph is subject to different excitations; 100, 200, and 300 V asymmetric sinusoidal signals on both sides. Up to 15% increase in pressure are expected to be achieved with a commercially available compact piezoelectric bimorph. Much higher pressure ratios can be obtained by optimizing the cavity/actuator design.

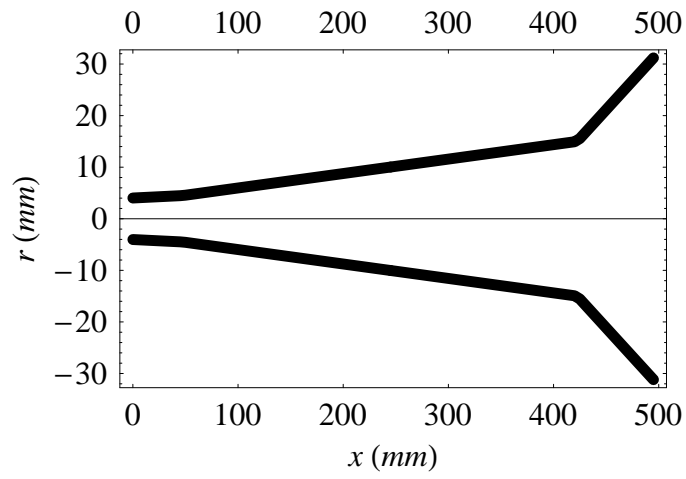


Figure 4.7: A 0.5 m length resonator geometry.

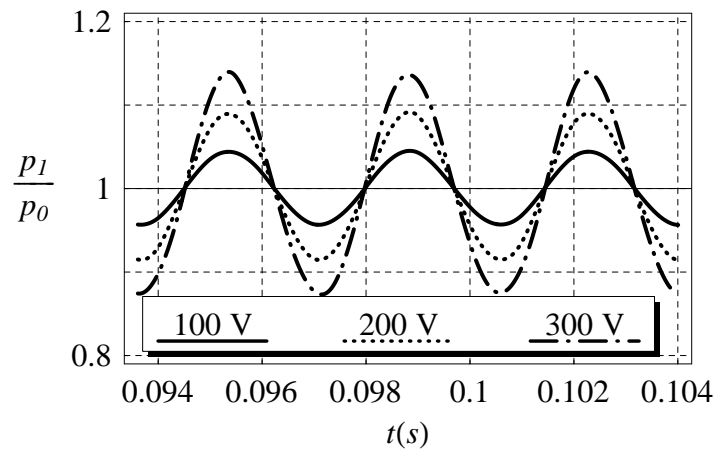


Figure 4.8: Pressure ratio predicted by the proposed model at the small end of the 0.5 m resonator shown in Figure 4.7.

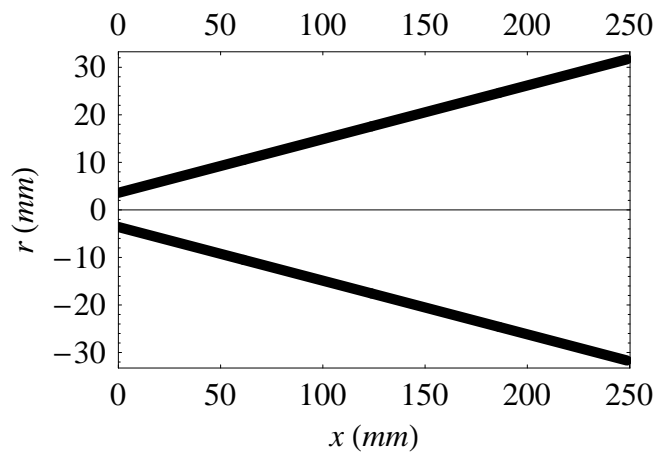
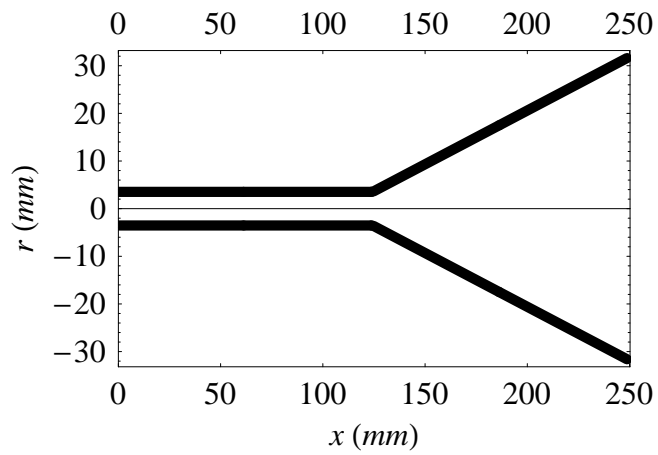
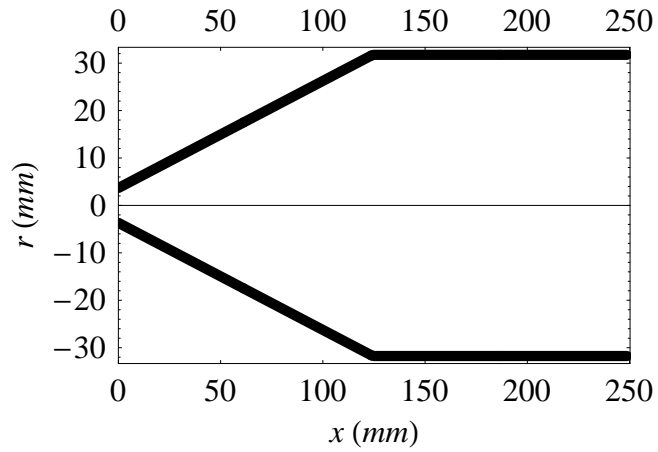


Figure 4.9: Different resonator geometries; bottle, funnel, and cone used in cavity optimization.

An optimization process which yields the most efficient resonators should involve setting up the overall length, appropriate design of the geometry of the cavity, configuring the piezoelectric bimorph and most importantly deciding the optimal cavity/actuator combination. As an example, we consider a 0.25 m long cavity which is actuated by the bimorph whose properties are in Table 4.1. The diameter of one end is 9 times larger than the other one. We try three options; the bottle, the funnel and the cone as shown in Figure 4.9.

The resonator is filled with air, $\rho_0 = 1.25 \text{ kg/m}^3$, $\gamma = 1.4$, $\delta/c_0^2 = 0.05 \text{ s}$, and excited at 100 V. The fundamental frequencies are 322, 268, and 292 Hz respectively. Figure 4.10 shows the predicted pressure wave for each of them. The funnel yields pressure ratios 5 times more than those of the other configurations. This shows the importance of an optimized resonator geometry to achieve high pressures with the same actuator.

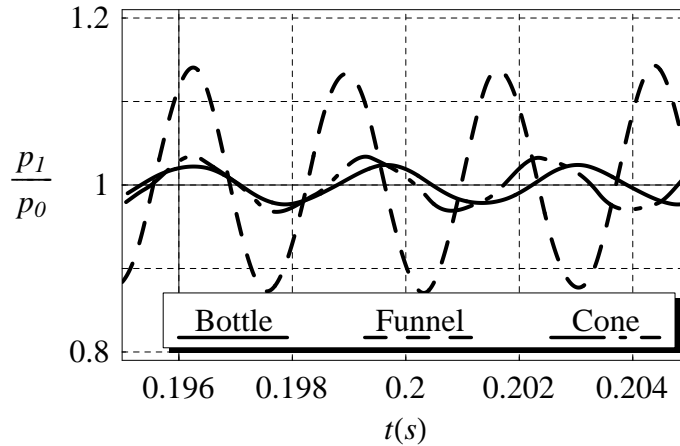


Figure 4.10: **Different resonator geometries; bottle, funnel, and cone used in cavity optimization.**

4.6 Intermediate Diaphragm Excitation

Figure 4.11 shows a schematic of an acoustic resonator driven by a rigid diaphragm that is connected to a piezoelectric bimorph through a spring element. This design will allow driving the gas at a constant speed throughout the whole cross-section as well as providing more control on the driving frequencies by tuning the mass m_d and the stiffness k_d of the diaphragm.

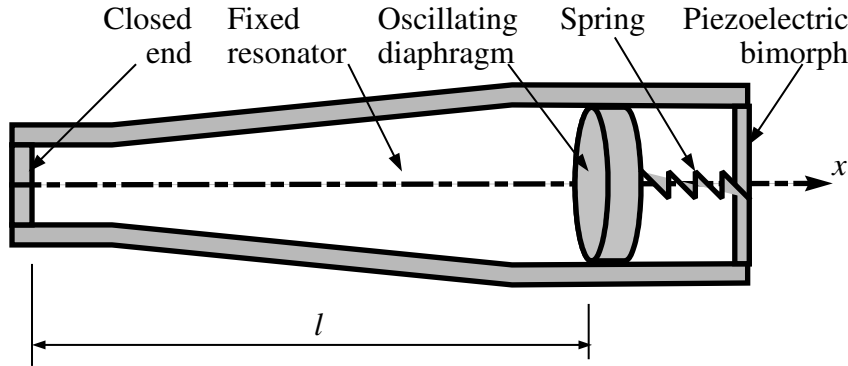


Figure 4.11: A schematic of a diaphragm driven resonator excited by a piezoelectric bimorph.

The diaphragm is subject to the force in the spring, acoustic pressure, as well as its own inertia forces. Therefore, the equation of motion for the diaphragm is

$$m_d \frac{\partial^2 u_d}{\partial t^2} + k_d(u_d - u_p) + p(l, t)s(l) = 0 \quad (4.71)$$

where u_d is the displacement of the diaphragm. Equation (4.71) is differentiated once with respect to time to give

$$m_d \frac{\partial^2 v_d}{\partial t^2} + k_d(v_d - v_p) + s(l) \frac{\partial p}{\partial t} = 0 \quad (4.72)$$

where v_d is the velocity of the diaphragm. The motion is assumed harmonic with frequency ω and the pressure is substituted by the velocity potential in equation (4.65).

$$(k_d - \omega^2 m_d) v_d - k_d v_p - \rho_0 c_0^2 s(l) \varphi_{nf} = 0 \quad (4.73)$$

Also, the equation of the first element of the piezoelectric bimorph will be affected by the diaphragm displacements as follows

$$\left(\mathbf{K}_{p3j}^1 - \omega^2 \mathbf{M}_{p3j}^1 \right) u_j^1 = k_d (v_d - u_3^1) \quad (4.74)$$

The vector of all degrees of freedom includes one extra degree for the diaphragm velocity.

$$\mathbf{q} = \left\{ \begin{array}{c} \boldsymbol{\Psi}(x) \\ U_d(x) \\ \mathbf{U}(x) \end{array} \right\} \eta(t) \quad (4.75)$$

The fluid system is not altered except for being excited by the displacement of the diaphragm rather than that of the bimorph. While the piezoelectric bimorph is subject to the spring force instead of the acoustic pressure. Therefore, the global equation of motion of the unforced system with the diaphragm is

$$\left(\left[\begin{array}{ccc} \mathbf{K}_f & \mathbf{C}_{fd} & \mathbf{O} \\ \mathbf{C}_{df} & k_d & \mathbf{C}_{dp} \\ \mathbf{O} & \mathbf{C}_{pd} & \mathbf{K}_p' \end{array} \right] - \omega^2 \left[\begin{array}{ccc} \mathbf{M}_f & \mathbf{0} & \mathbf{0} \\ \mathbf{0} & m_d & \mathbf{0} \\ \mathbf{0} & \mathbf{0} & \mathbf{M}_p \end{array} \right] \right) \cdot \left\{ \begin{array}{c} \boldsymbol{\Psi} \\ U_d \\ \mathbf{U} \end{array} \right\} = \left\{ \begin{array}{c} \mathbf{0} \\ \mathbf{0} \\ \mathbf{0} \end{array} \right\} \quad (4.76)$$

where \mathbf{K}'_p is nothing but the piezoelectric stiffness matrix with a single modification in the \mathbf{K}_{p33}^1 element due to equation (4.74) which makes $\mathbf{K}'_{p33} = \mathbf{K}_{p33} + k_d$

The coupling between fluid, piezoelectric and diaphragm shows up in four coupling vectors; the effect of the diaphragm on the fluid comes in

$$\mathbf{C}_{fd} = -c_0^2 * s(l) \left\{ \begin{array}{c} 0 \\ \vdots \\ 0 \\ 1 \end{array} \right\} \quad (4.77)$$

while the effect of the fluid on the diaphragm

$$\mathbf{C}_{df} = -\rho_0 c_0^2 * s(l) \left\{ 0 \quad \dots \quad 0 \quad 1 \right\} \quad (4.78)$$

as well as the effect of the piezoelectric bimorph on the diaphragm

$$\mathbf{C}_{df} = -k_d \left\{ 0 \quad 0 \quad 1 \quad 0 \quad \dots \quad 0 \right\} \quad (4.79)$$

and finally, the effect of the diaphragm on the piezoelectric bimorph

$$\mathbf{C}_{fd} = -k_d \left\{ \begin{array}{c} 0 \\ 0 \\ 1 \\ 0 \\ \vdots \\ 0 \end{array} \right\} \quad (4.80)$$

As an example, the model of the acoustic resonator driven by a diaphragm that is connected to a piezoelectric bimorph through a spring element is applied to the resonator whose dimensions are shown in Figure 4.4, while the properties of the driving piezoelectric bimorph are available in Table 4.1. The diaphragm is assumed

to have a mass of 2g and a stiffness of 5000 N/m, i.e. the diaphragm system alone has a natural frequency of 252 Hz. Using these values in the new coupled model will make the first natural frequency of the coupled system be 108 Hz, while the second one is at 338 Hz.

4.7 Summary

In this chapter, axisymmetric resonators driven by piezoelectric bimorphs are modeled using the finite element method after developing the weak form of the gas and piezoelectric dimensional equations. The two systems are discussed separately and then coupled at the points of interaction. The mode shapes of the coupled system are extracted and then used in studying the forced oscillations of the system. Forcing arises from the applied voltage to the piezoelectric bimorph. The proposed model fully accounts for the nonlinear behavior of the gas oscillations close to resonance conditions, while the piezoelectric bimorph is assumed to behave in linear fashion. The advantages of the proposed model include being able to deal with arbitrary shaped resonators including complicated geometries at a low computational cost, besides being flexible to account for different scenarios including gas flow through boundaries. The study of the coupled system is proven crucial to fairly estimate the behavior of acoustic resonators driven by piezoelectric bimorph. It has also been shown that there are many design variables in the acoustic resonator which needs a lot of optimization effort. A better control of the characteristics of the system can

be achieved by adding a diaphragm between the piezoelectric and fluid systems. The model is modified to accommodate for the diaphragm properties which can be simply included in a mass and stiffness. The proposed model represents an invaluable tool in the design of piston driven axisymmetric acoustic resonators, and is a step towards the use of compact sized, low power, clean and environment friendly actuators in smart structures.

Chapter 5

Experimental Validation

5.1 Introduction

This chapter aims at evaluating the performance of resonators of different configurations in an attempt to demonstrate their merits and limitations. The experimental results are used to validate the predictions of the finite element models developed in the previous chapters for the different cases; resonators driven entirely by electro-mechanical shakers, piston driven resonators, resonators with external flow, piezoelectric bimorphs, and piezoelectric bimorph actuated resonators. It is envisioned that the second class of resonators with piezoelectric drive presents a practical and viable approach to the development of acoustic compressors which is suitable for various applications such as refrigeration and vibration control. Furthermore, the predictions of the developed model will be compared to the predictions of a commercial finite

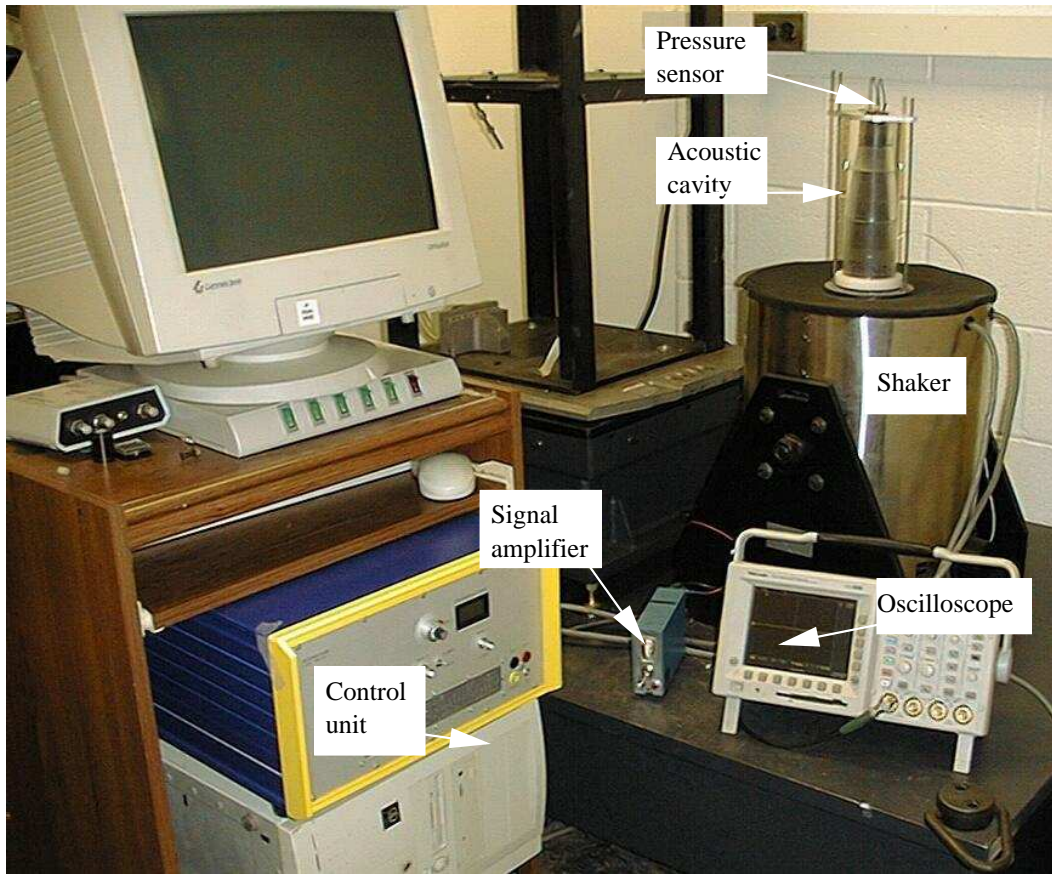


Figure 5.1: **Experimental setup used for entirely driven resonators.**

element software (ANSYS) in order to demonstrate the advantages of the developed model and the limitations of the commercial software.

5.2 Entirely Driven Resonators

The experimental setup used to validate the entirely driven resonators model is shown in Figure 5.1. The acoustic cavity is placed right on top of a 500 pound VTS electromechanical shaker. The shaker is actuated by a function generator and an amplifier. A pressure sensor is mounted at the end of the resonator and the sensor

output signal is sent to a 100 MHz Tektronix oscilloscope. Two pressure sensors were used; Omega dynamic pressure sensor model number PX 181 and PCB Piezotronics model number 113A26. The former is not suitable for the case of entirely driven resonators as the inertial forces affects the output signal.



Figure 5.2: **The resonator used in entirely driven resonator experiments.**

Figure 5.2 shows the acoustic cavity which consists of an acrylic cylindrical thick shell that surrounds the main PVC smooth cavity to add rigidity to it. At one end of the cavity, there is a check valve to allow charging the cavity with high pressure gas and on the other end there is a threaded hole to allow the mounting of the pressure sensor or an output check valve.

Figure 5.3 shows the dimensions in inches of the acoustic cavity which consists of three sections; two straight sections with different diameters and a conical section in between. Unless otherwise mentioned, this cavity is used in all different tests presented in this chapter.

Figures 5.4 and 5.5 show the time histories of the pressure ratios as predicted by the finite element model and as monitored experimentally for the cavity shown in 5.3

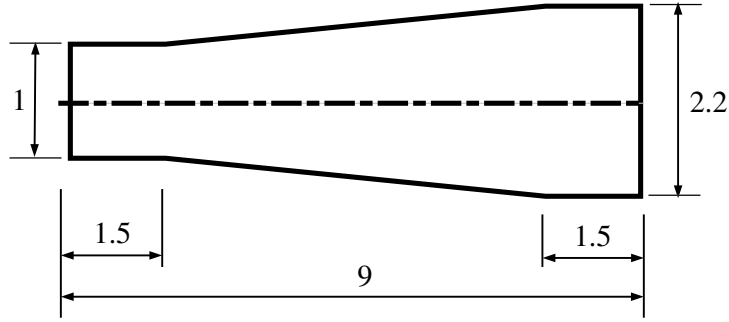


Figure 5.3: **Schematic of the dimensions in inch of the resonator used in entirely driven resonator experiments.**

when excited at accelerations of 40g and 60g, respectively. Good agreement is evident between the experimental and theoretical results at both excitation amplitudes.

Using the same setup, the frequency response of the cavity was obtained by sweeping the excitation frequency up and down at a rate of $\pm 1\text{Hz/s}$ around the fundamental frequency of the cavity at a constant acceleration. The maximum pressure ratios are recorded and plotted against the excitation frequencies. The frequency response can be numerically predicted by the proposed finite element model using the method described in Nayfeh and Balachandran [43]. Figures 5.6 and 5.7 show the frequency response of the pressure ratios as predicted by the finite element model and as measured experimentally for the same cavity when excited at accelerations of 40g and 60g, respectively. Good agreement is evident between the experimental and theoretical results at the lower excitation amplitude, and a considerable deviation is observed at the higher one. It is also evident that the nonlinear physical phenomena of air stiffness hardening and frequency shift were captured by the finite element model.

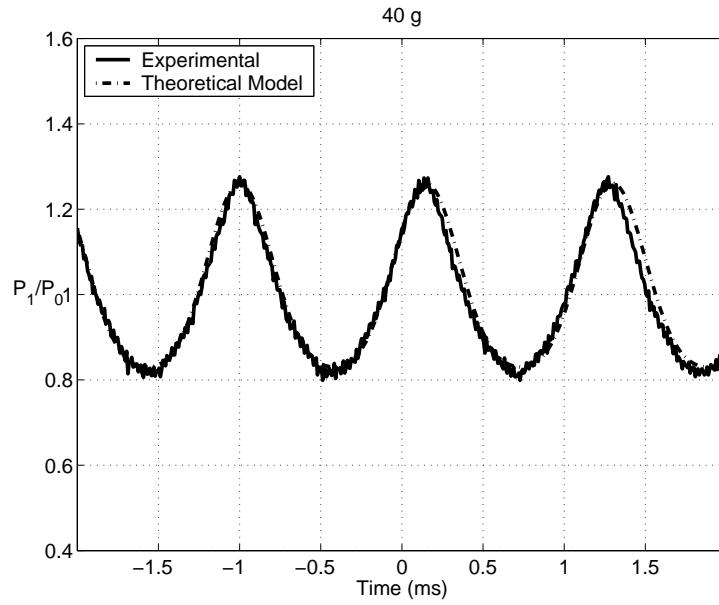


Figure 5.4: Comparison between the experimental and theoretical time histories of the pressure ratio of the entirely driven resonator at 40 g in time domain.

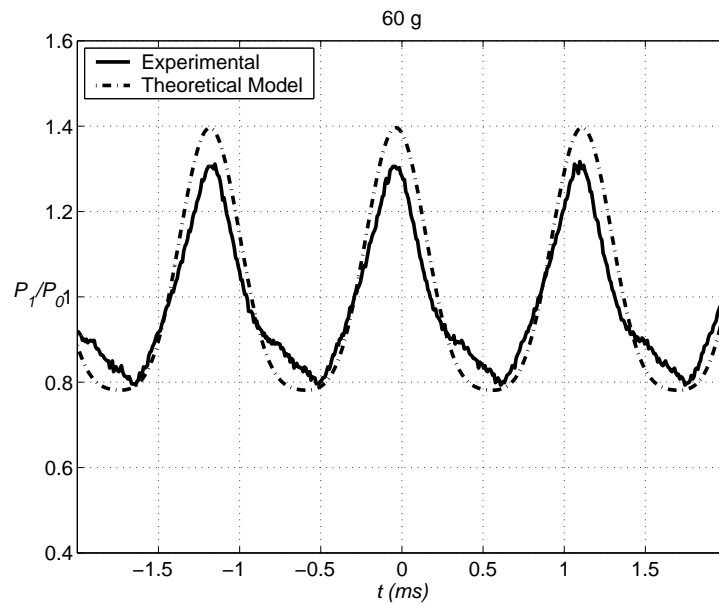


Figure 5.5: Comparison between the experimental and theoretical time histories of the pressure ratio of the entirely driven resonator at 60 g in time domain.

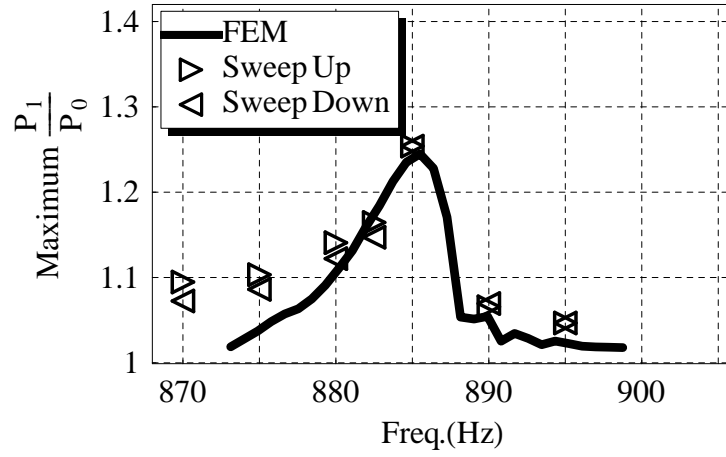


Figure 5.6: Comparison between the theoretical and experimental frequency responses of the entirely driven resonator at 40 g.

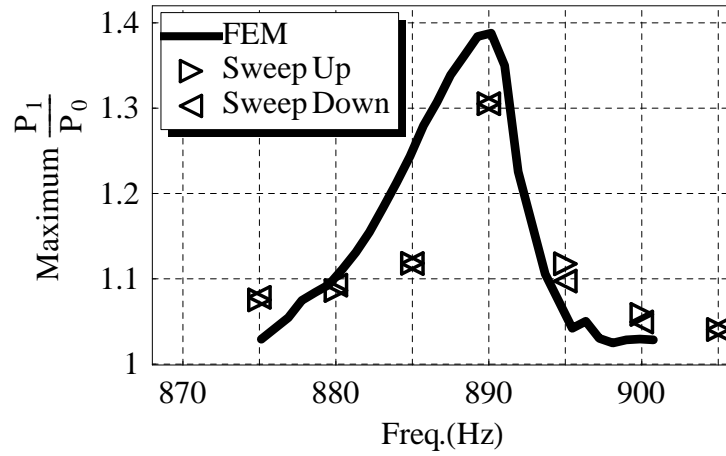


Figure 5.7: Comparison between the theoretical and experimental frequency responses of the entirely driven resonator at 60 g.

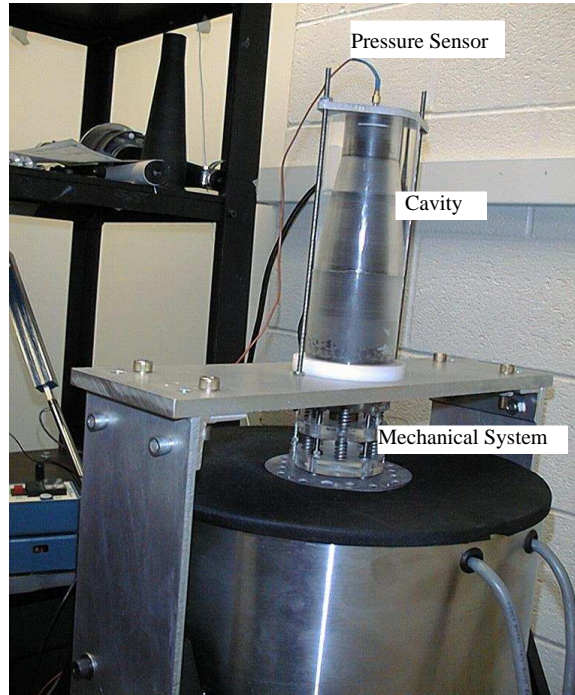


Figure 5.8: **Experimental setup used for piston driven resonators using an electromechanical shaker as the drive.**

5.3 Piston Driven Resonators

Figure 5.8 shows the piston driven arrangement in which the resonator is placed on a fixed base and the shaker is used as the actuating piston to move the lower boundary of the resonator. Also shown in the figure, the mass-spring system that is represented by the schematic in Figure 4.11.

Figure 5.9 shows another piston driven arrangement in which the piston is actuated by a stack piezoelectric actuator, Burleigh PZ100, Fisher, NY.

Figure 5.10 shows a comparison between the predictions of the finite element model (left) as compared to the experimental pressure ratios (right). A close agreement



Figure 5.9: **Experimental setup used for piston driven resonators using a Piezoelectric Stack as the drive**

between the theory and experiment is evident.

The predictions of the proposed model are compared to the experimental results obtained by Galiev *et al.* [22] who had conducted their experiments on a 3.4 m long cylindrical tube excited by a car engine oscillating near the fundamental frequency of the air column with an amplitude of 55 mm. With a simple calculation, this corresponds to an excitation of almost 550 g. The maximum recorded pressure ratio was 0.36. The first column of Figure 5.11 shows the pressure wave obtained experimentally at several excitation frequencies, while the second column shows the predictions of the proposed model at the same frequencies assuming $c_0 = 340$ m/s, $\gamma = 1.4$, $\delta/c_0^2 = 0.2s$ with 20 modes considered. It is obvious from the figure that there is a very good match between the wave forms in both cases which proves that the proposed nonlinear model is able to capture the dynamics of the system to a good extent even at such high excitations. Also, the maximum pressure ratio predicted by the model is 0.4 which is quite comparable to the value obtained experimentally.

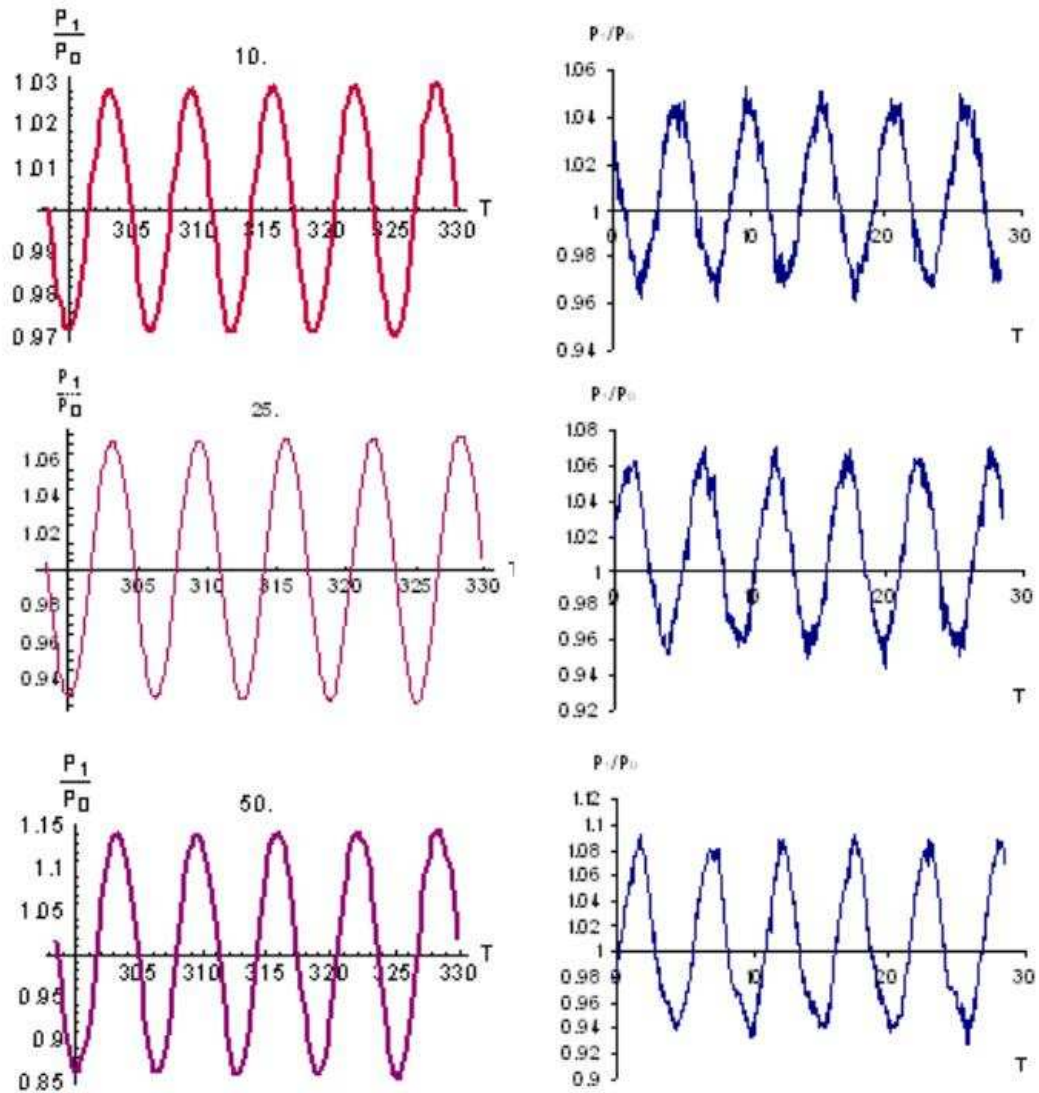


Figure 5.10: Comparison of theoretical (left) to experimental (right) results for piston driven resonators.

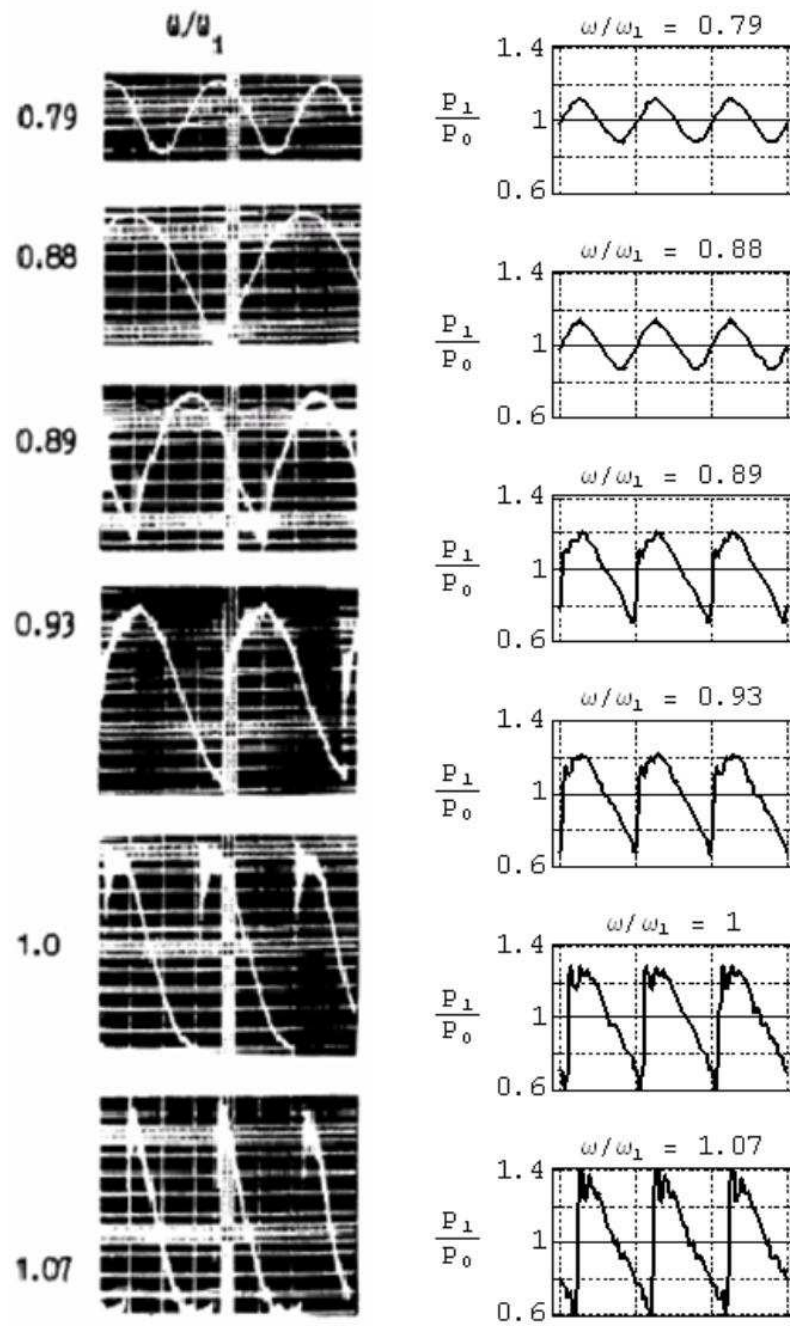


Figure 5.11: Comparison between the predictions of the proposed model and the experimental results of Galiev *et al.* [22] for a 3.4 m long cylindrical resonator excited at 550g.

5.4 Resonators with Flow

An essential part that would make the resonator of practical importance as a compressor is the suction and delivery of the gas into and from the resonator. This is a real challenge in the case of acoustic compressors. The reason for that is the relatively high frequencies at which the resonator should be operated at. These conditions make the use of conventional mechanically operated check valves impractical. Therefore, piezoelectric valves have been selected in order to regulate the suction and delivery processes.

Figure 5.12 shows an LFPX 0500500B piezoelectric 2-Way air valve manufactured by The Lee Company [44]. It has a response time of 0.5 ms which makes it good for almost 1kHz operation.

The valve is driven by an 80V square control signal that can be developed from the circuit shown in Figure 5.13.

The valve is first tested on the test rig shown in Figure 5.14 which can be represented by the schematic in Figure 5.15. The test rig consists of an accumulator



Figure 5.12: **LFPX 0500500B Piezoelectric valve, from The LEE Company.**

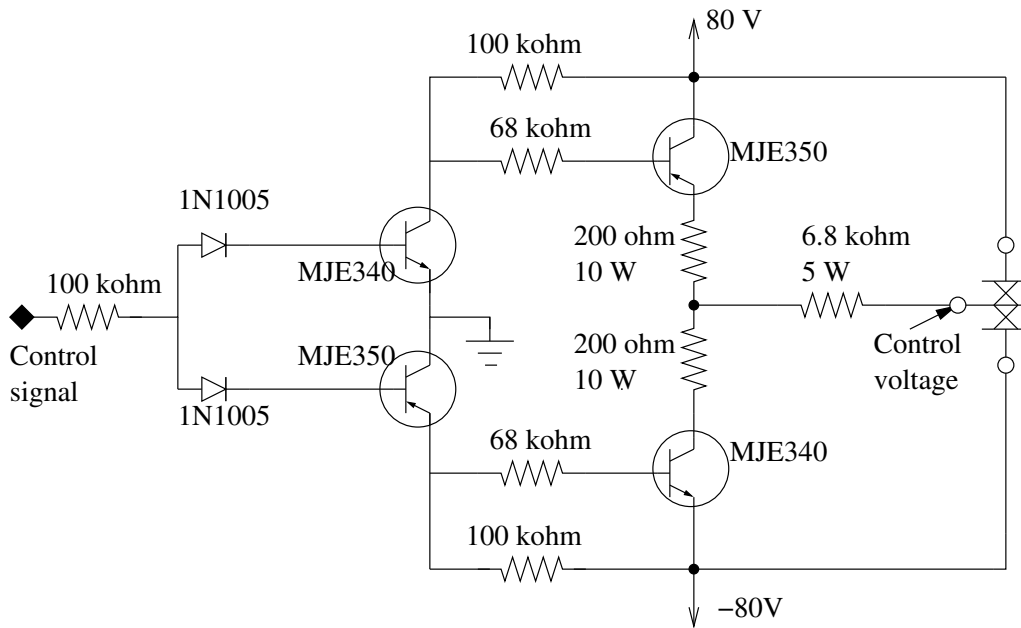


Figure 5.13: **LFPX 0500500B Piezoelectric valve control circuit.**

for the input air whose pressure is measured using an electrical pressure gage. Air is then passed through the valve which is actuated by a square 80V signal and then the air pressure is being measured again in the output accumulator. The flow of air is controlled by a fine regulator and the flow is being measure with an Omega electrical flow meter with a capacity of 1 liter/min.

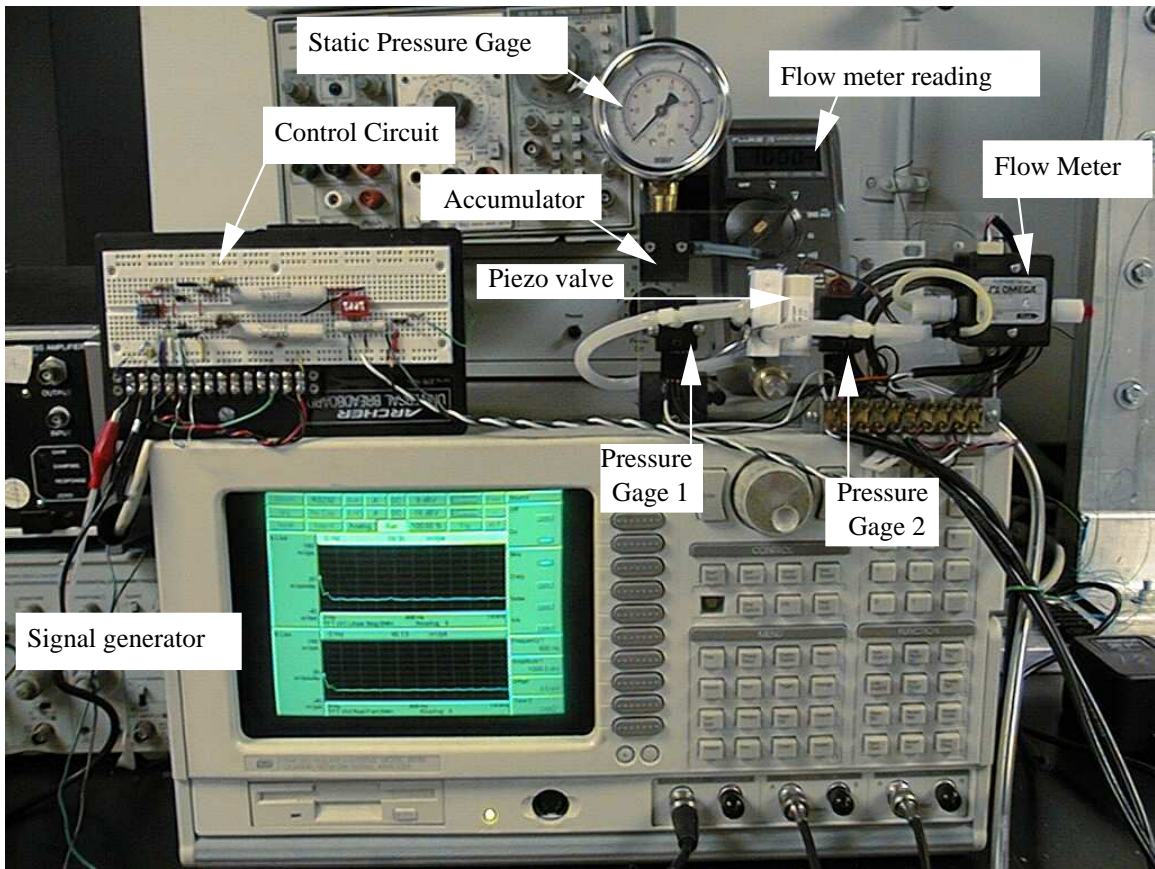


Figure 5.14: Testing of the piezoelectric valve.

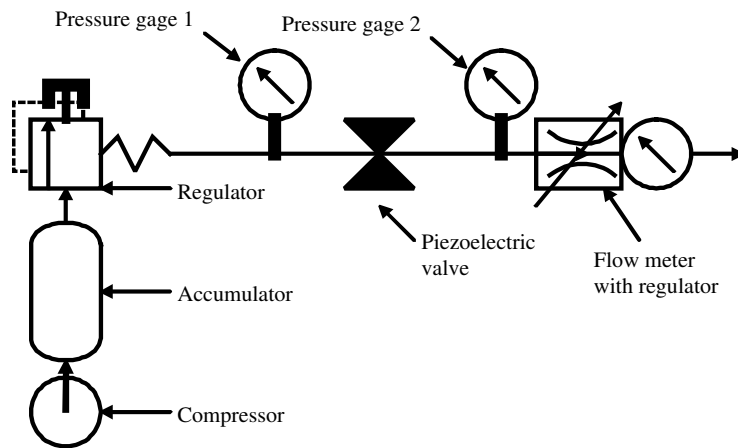


Figure 5.15: Schematic for the testing of the piezoelectric valve.

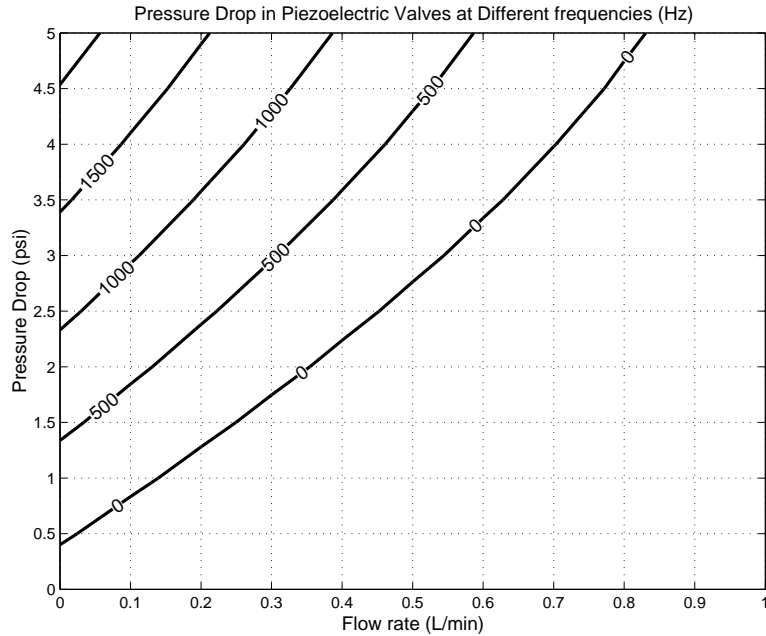


Figure 5.16: **Pressure drop in the piezoelectric valve.**

Figure 5.16 shows the pressure drop through the valve when actuated with an 80 V signal at different frequencies and contours of different flow rates.

The tested valve is connected to an acoustic resonator as shown in Figure 5.17. The resonator is either entirely driven by the shaker as in Figure 5.18 or driven by a piezoelectric stack as in Figure 5.19. In both figures, a control panel is shown with its switches, pressure and flow gages, and most importantly a phase shifter. These components control an electrical circuit in order to synchronize the opening and closing of the valves in response to the pressure sensor signal. The phase shifter is intended for controlling the phase between both signals and can be tuned to ensure that the resonator is able to deliver its high pressure gas. This experimental setup was able to deliver a D.C. flow of up to 0.2 liters/min. At such high flow rates, the gage pressure dropped to almost zero.

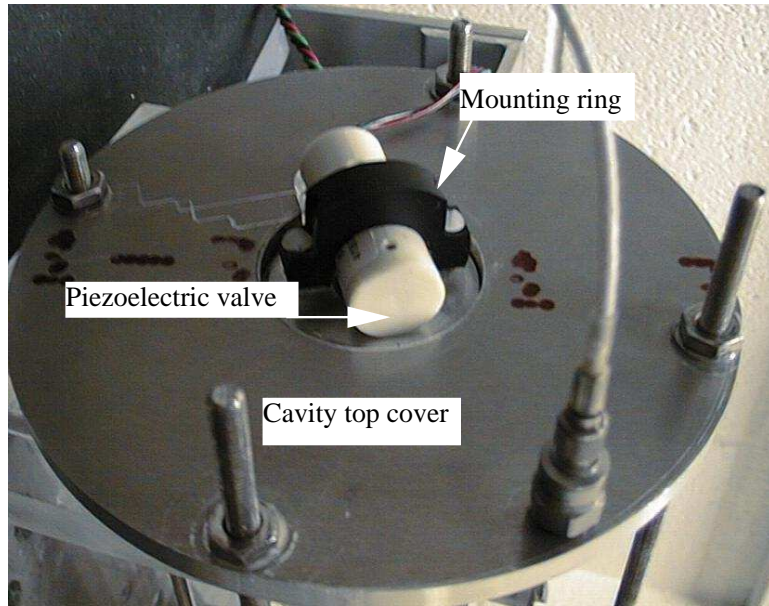


Figure 5.17: Piezoelectric valve mounting on an acoustic resonator.

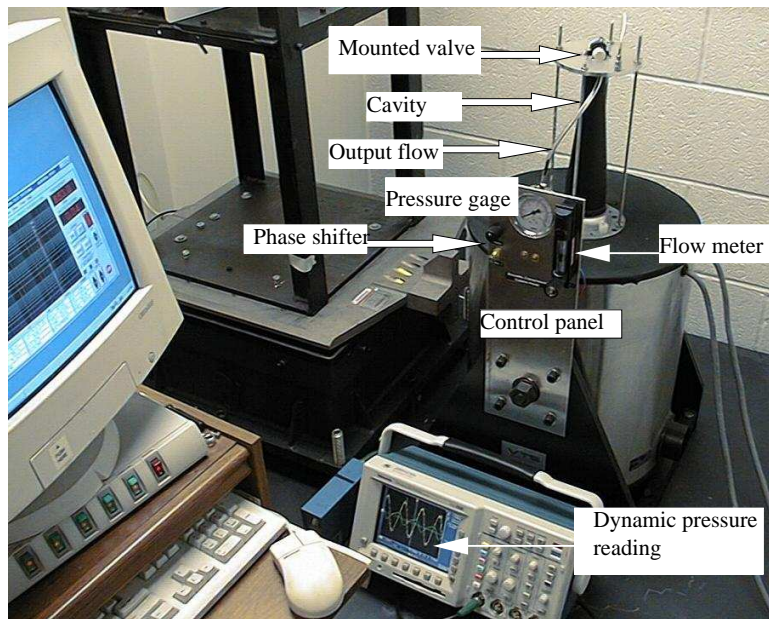


Figure 5.18: Entirely driven resonator with flow experimental setup.

5.5 Axisymmetric Resonators Driven by Piezoelectric Bimorphs

Figures 5.20-5.24 show the response of a piezoelectric bimorph to sinusoidal voltage excitations at 100, 200, 250, 300, and 400 Hz. The piezoelectric bimorph whose properties are listed in Table 5.1 is manufactured by Piezomechanik, GMBH. The measurements are taken using a laser vibrometer PSV-200, Polytec Inc. The experimental results indicate that the natural frequency (0,1) of the piezoelectric bimorph is approximately equal to 250 Hz. The finite element model predicts the natural frequency to be 254 Hz, which proves the validity of the finite element model for piezoelectric axisymmetric bimorphs.

Figure 5.25 shows a 3.25 inch long glass resonator that takes the shape of a funnel. A 2.5 inch piezoelectric bimorph is mounted to its big end and a pressure sensor is mounted to the small end.

Figure 5.26 shows the frequency response of the 3.25 inch funnel resonator when excited by a 50 V asymmetric control signal. It is clear that the fundamental frequency of the system is at 475 Hz. The model predicts it to be 490 Hz. It is worth mentioning that the bimorph alone without the cavity has its natural frequency at 248 Hz. This proves that the model is quite accurate in predicting the large shifts in natural frequency due to the fluid loading on the piezoelectric bimorph. However the pressure ratio obtained experimentally was less than that predicted theoretically.

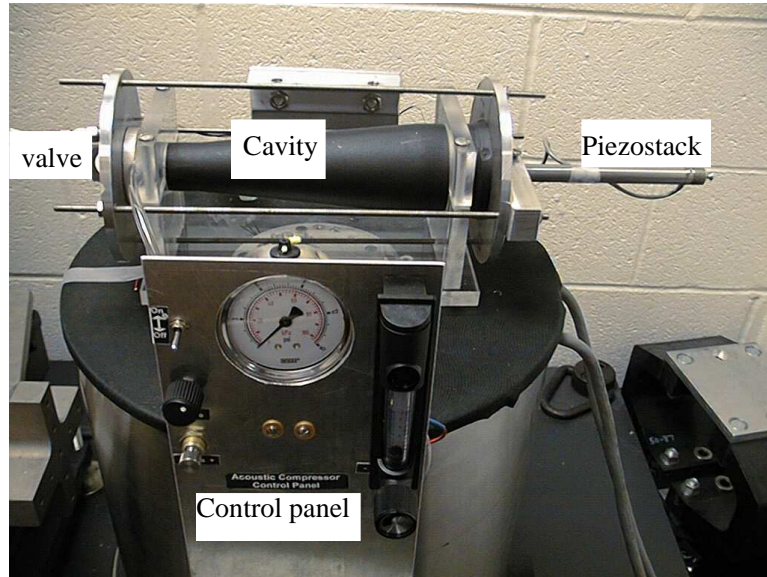


Figure 5.19: **Piston driven resonator with flow experimental setup.**

Table 5.1: **Physical, mechanical and electrical properties of a 3” piezoelectric bimorph.**

	Piezoelectric	Shim
No. of layers	2	1
Outer Diameter (mm)	75	75
Inner Diameter (mm)	15	15
Thickness (mm)	0.275	0.03
Material	PZT-5A	Nickel
Density (Kg/m ³)	7750	7800
Elasticity Modulus (GPa)	52	207
Poisson’s ratio	0.3	0.3
Piezoelectric constant (N/V/m)	15.8	–
Dielectric Relative Permittivity	3300	–

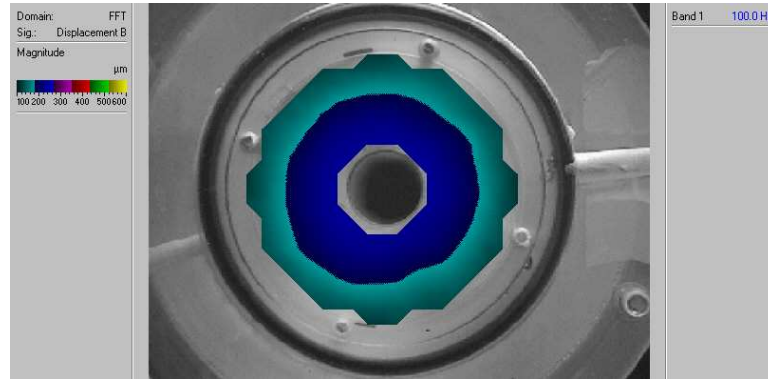


Figure 5.20: Displacements of the piezoelectric bimorph excited at 100 Hz.

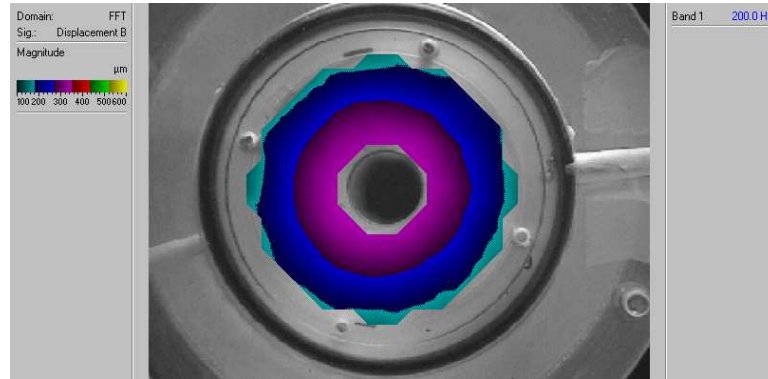


Figure 5.21: Displacements of the piezoelectric bimorph excited at 200 Hz.

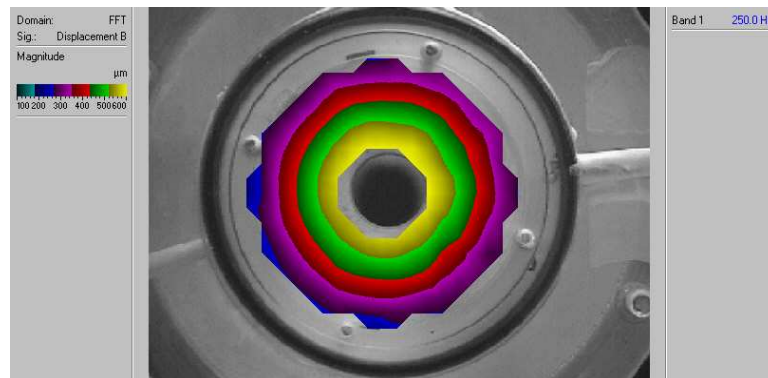


Figure 5.22: Displacements of the piezoelectric bimorph excited at 250 Hz.

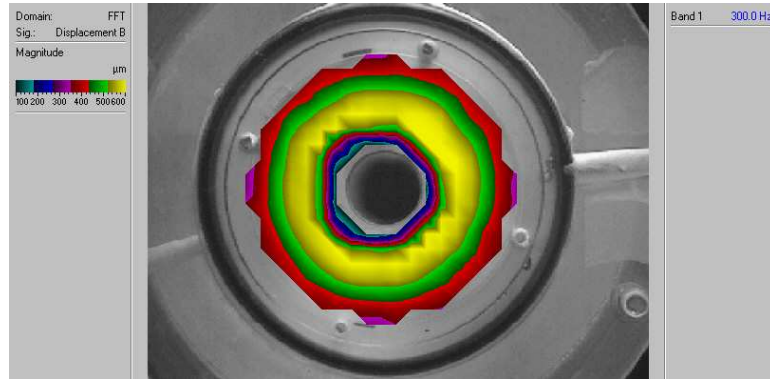


Figure 5.23: Displacements of the piezoelectric bimorph excited at 300 Hz.

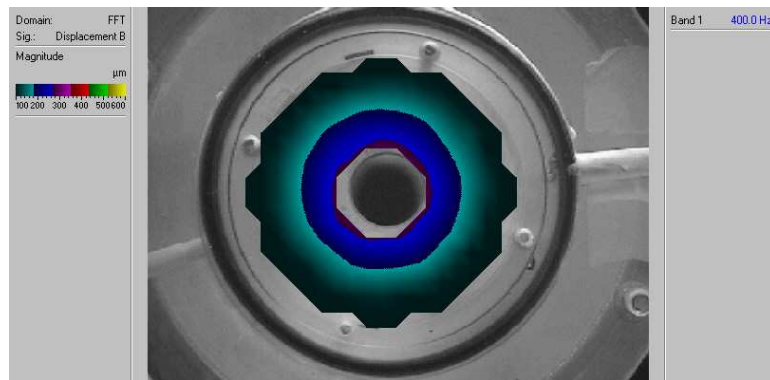


Figure 5.24: Displacements of the piezoelectric bimorph excited at 400 Hz.

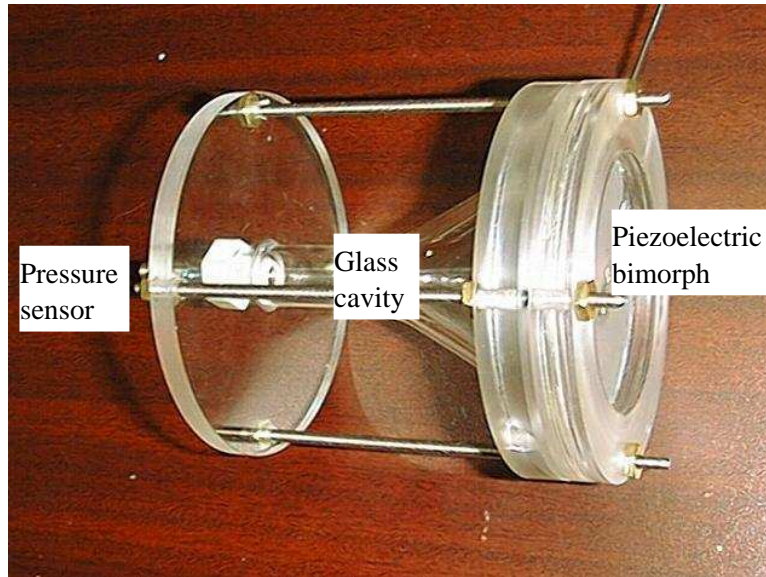


Figure 5.25: Piezoelectric bimorph driven resonator.

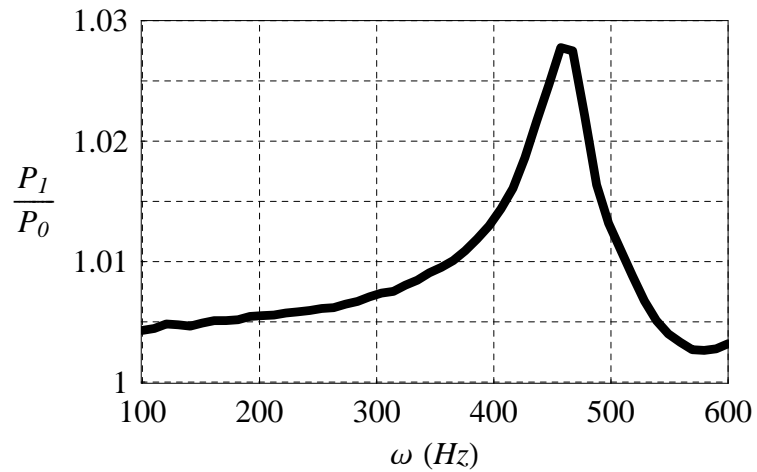


Figure 5.26: Frequency response of the funnel resonator driven by a piezoelectric bimorph.

The reason may be due to the drastic changes in the resonator geometry or the piezoelectric bimorph is not well designed for this type of application.

Figure 5.27 shows the time time response for a 6 inch horn resonator excited at {200,250,300} V. The actuator consists of an aluminum shim layer with 2 inch diameter and 0.1 mm thickness. On both sides of the shim layer are two piezoelectric discs of 1.25 inch diameter and 0.4 mm thickness. This configuration yielded pressure ratios up to 1.125. The resonance frequency predicted by the theoretical model is 1075 Hz which is again close to that obtained experimentally.

5.6 Resonators Driven by Piezoelectric Bimorphs with Intermediate Diaphragm

Figure 5.28 shows a 3 inch Piezomechanik piezoelectric bimorph on which is mounted a speaker diaphragm. Mounting is done through a central stud and two 11 kN/m Century compression 0.25” springs with ground ends. The properties of the piezoelectric bimorph are listed in Table 5.1.

Figure 5.29 shows the experimental setup in which a function generator supplies a sinusoidal signal to the amplifier whose output is passed to the bimorph which excites the diaphragm and consequently the gas inside the resonator. The pressure oscillations at the small end are measured by the PCB piezoelectric pressure sensor.

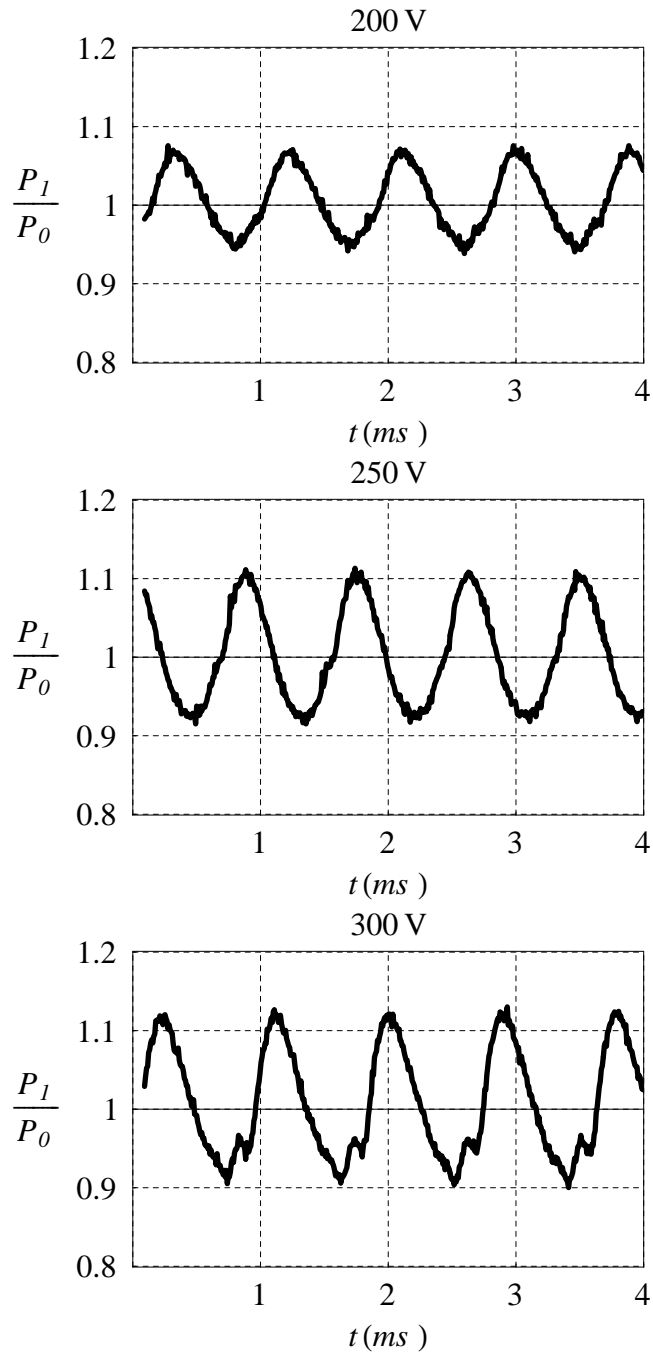


Figure 5.27: Time response of the 6 inch resonator driven by a piezoelectric bimorph at {200,250,300} V.

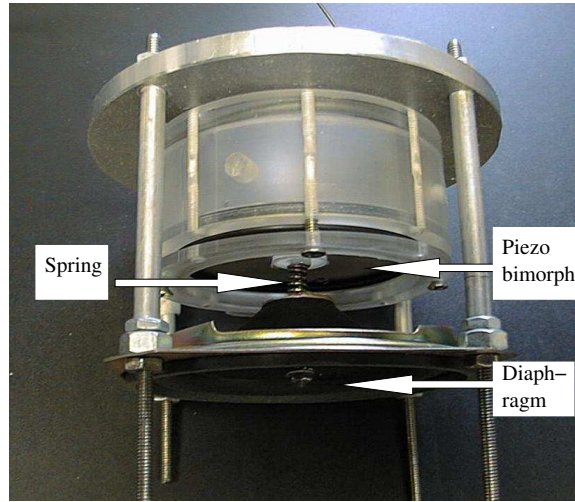


Figure 5.28: A diaphragm is mounted through springs to a piezoelectric bimorph .

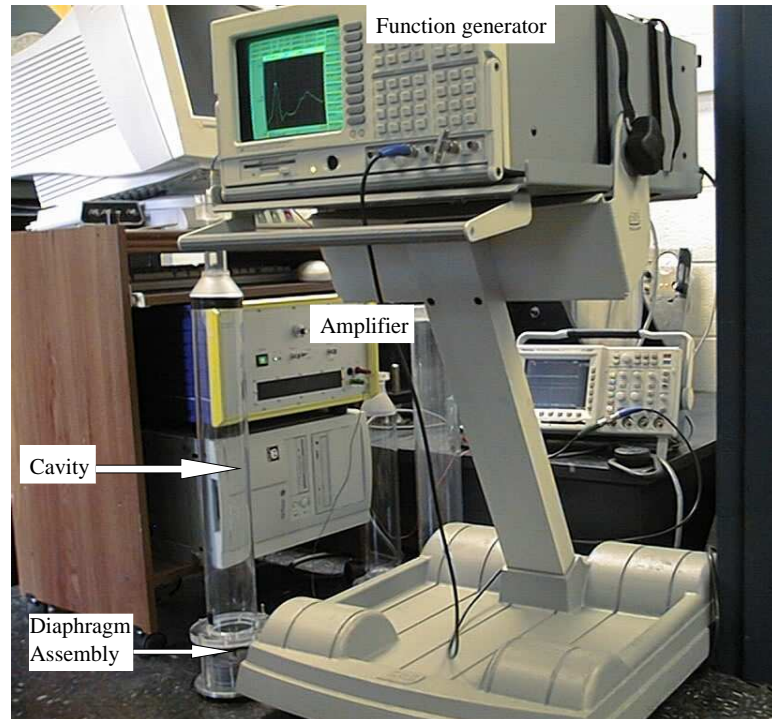


Figure 5.29: Experimental setup for an axisymmetric resonator driven by a piezoelectric bimorph through an intermediate diaphragm.

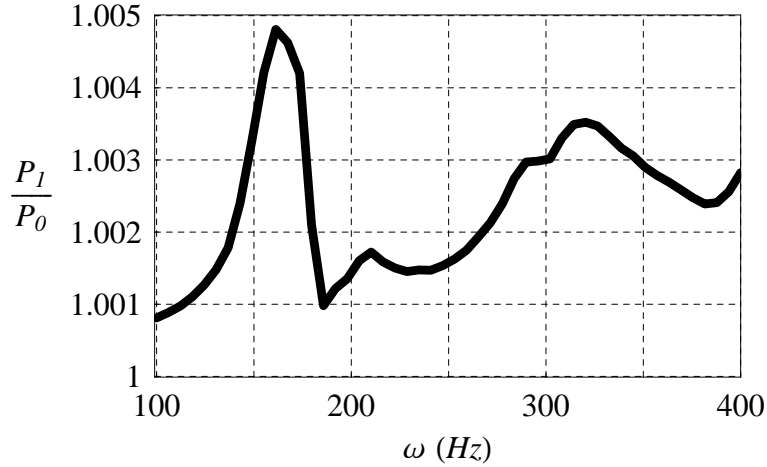


Figure 5.30: **Frequency response of the axisymmetric resonator driven by a piezoelectric bimorph through an intermediate diaphragm.**

Figure 5.30 shows the frequency response of the resonator. The figure shows that the first two natural frequencies are at 160 and 320 Hz. While the corresponding frequencies predicted by the proposed model are at 174 and 353 Hz.

A comparison between the performance of a piezoelectric bimorph actuator without and with the intermediate diaphragm is shown in Figures 5.31 and 5.31. The bimorph is actuated with a sinusoidal signal sweeping around the first natural frequency of the system and the voltage, current, and phase angle of the electric signal flowing from the amplifier to the actuator are measured. This is sufficient to calculate the power input. The displacements of the piezoelectric bimorph and the diaphragm are also measured when applicable. The figure demonstrates that the diaphragm can double the displacements of the system, with a lower power input.

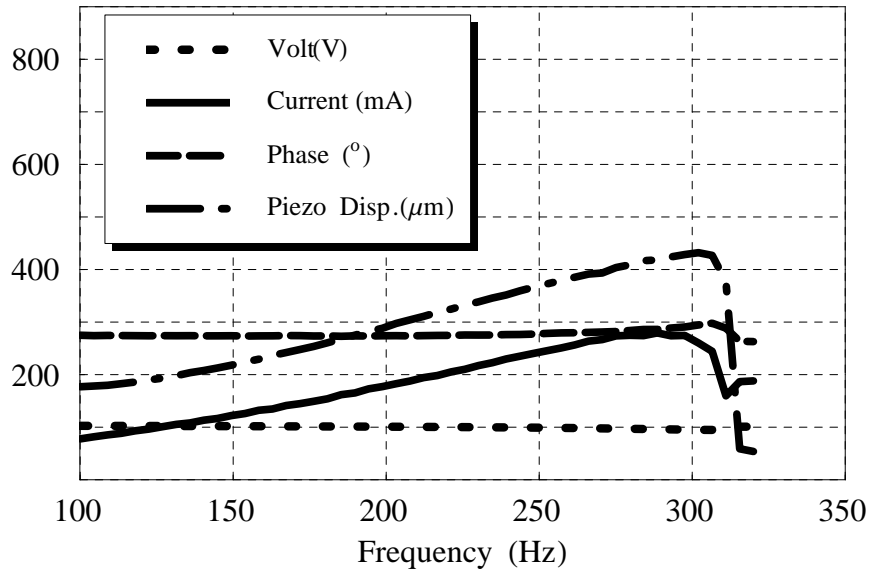


Figure 5.31: Frequency response of the actuator without the diaphragm.

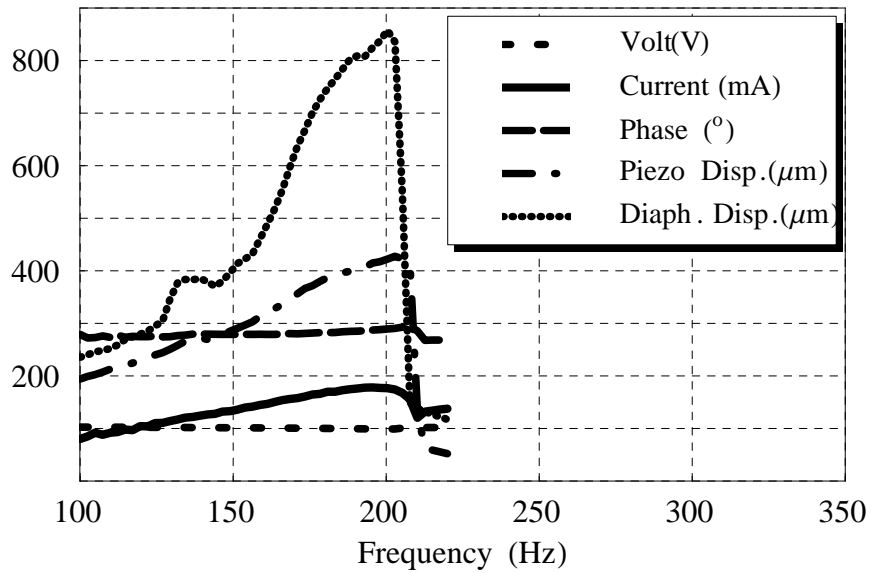


Figure 5.32: Frequency response of the actuator with the diaphragm.

5.7 Commercial Finite Element Software Validation

In this section the predictions of the proposed models are compared with the predictions obtained by building different models using the commercial finite element software ANSYS as well as the experimental results.

5.7.1 Axisymmetric Acoustic Resonators

An ANSYS model is built for axisymmetric acoustic resonators. The model is built using 2D axisymmetric acoustic elements Fluid29, with a solid-fluid interface at the boundaries. Figure 5.33 shows the acoustic elements which when rotated axisymmetrically will develop the 20 inch resonator shown in Figure 5.34. The bottom half of Figure 5.33 shows the first mode shape of the pressure wave predicted by the ANSYS model which occurs at 418.5 Hz. This is very close to the 418.9 Hz predicted by the proposed finite element model developed in the previous chapters. This matching is reasonable as both models are based on the linear acoustic equations.

5.7.2 Piezoelectric Bimorph Actuators

The predictions of the finite element model developed for the piezoelectric bimorphs is compared against that of ANSYS. Figure 5.35 shows the finite element

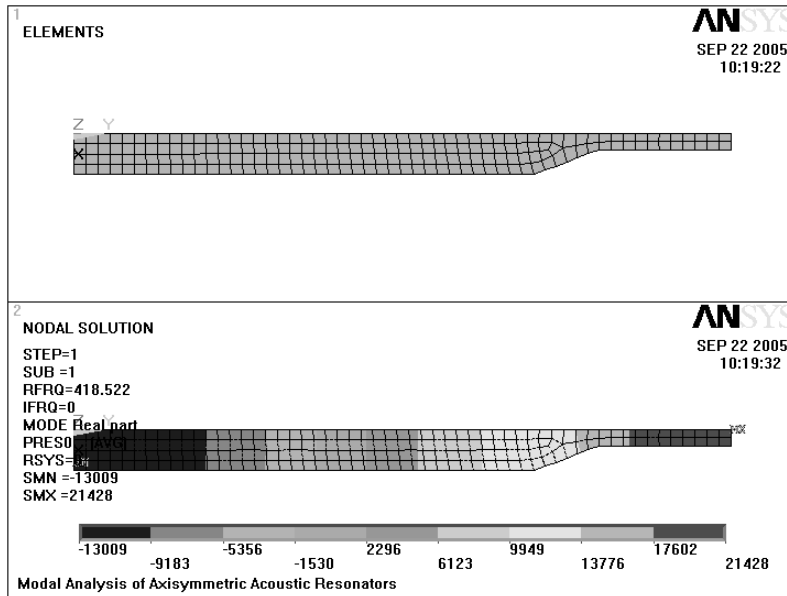


Figure 5.33: Elements and first mode shape of the acoustic resonator built by the ANSYS model.

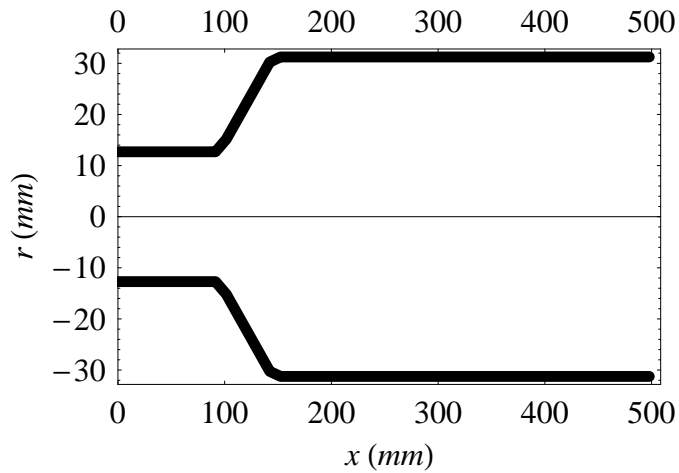


Figure 5.34: Schematic of a 20 inch resonator.

mesh built for the piezoelectric bimorph whose properties are listed in Table 5.1 as well as the first mode shape for the same bimorph. Axisymmetric PLANE223 with piezoelectric effects and PLANE82 are used for the piezoelectric and shim layers, respectively. More than 300 elements are needed to keep the length to width ratio of the 2-D elements reasonable. The fundamental frequency predicted by the ANSYS model is 289 Hz. The corresponding prediction of the finite element model developed in the previous chapter is 254 Hz using 5 cubic elements. Figure 5.36 shows the first mode (0,1) predicted by the model. As shown in Figure 5.20 to Figure 5.24 the experimentally measured fundamental frequency of this same bimorph is close to 250 Hz. Close agreement is evident between the theoretical predictions and the experimental results.

5.7.3 Piston Driven Acoustic Resonators

Figure 5.37 shows the pressure distribution as predicted by the ANSYS model for a 3.4 m long cylindrical resonator excited at the fundamental frequency (50 Hz) with a 1 mm base excitation. The predicted pressure amplitudes are excessively large. This is no surprise as the ANSYS model is linear running at resonance conditions. Not only does the pressure grows very large in the positive (compression) sense but it grows to the same level in the negative (vacuum) sense allowing for subzero pressures in the cavity. Adding damping will not help as it will decrease the pressure oscillations without making any difference between the positive and negative pressure variations.

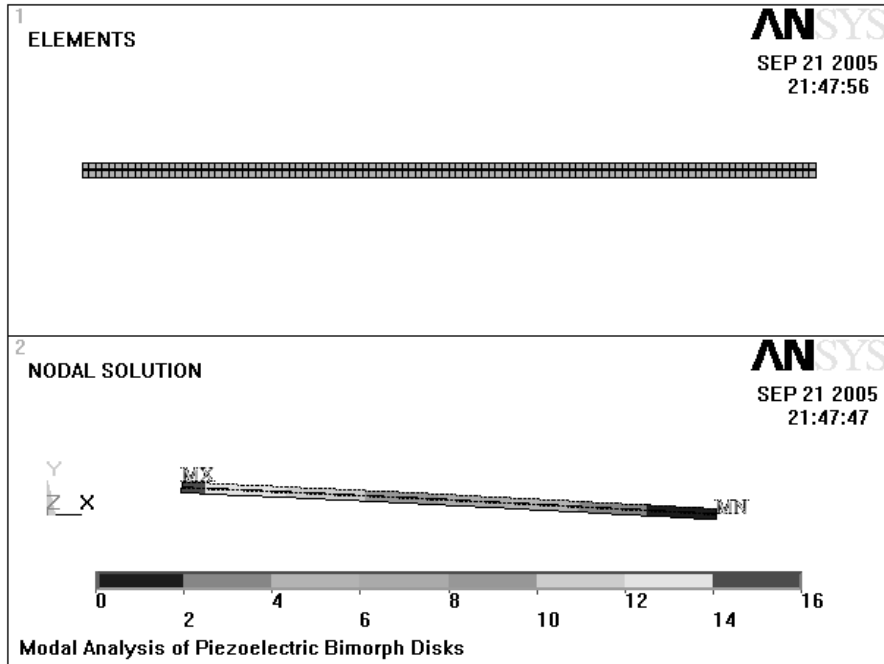


Figure 5.35: Elements and first mode shape of the 3” piezoelectric bimorph built by the ANSYS model.

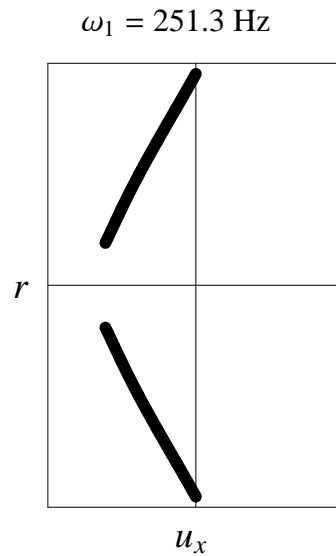


Figure 5.36: First mode shape of the 3” piezoelectric bimorph predicted by the proposed model.

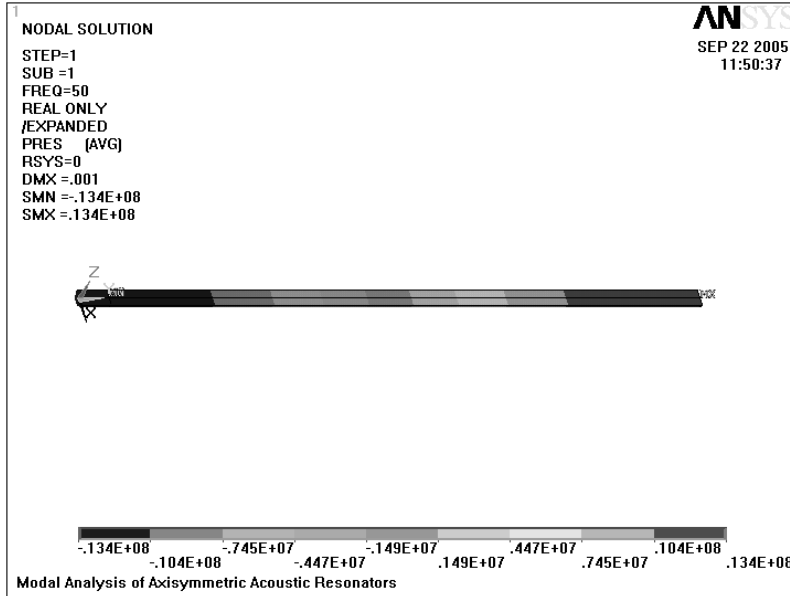


Figure 5.37: Pressure distribution predicted by the ANSYS model for a 3.4 m long cylindrical resonator.

When this is compared with the proposed nonlinear model and how it matches the results of Galiev *et al.* [22], one should appreciate the importance of the nonlinear model in predicting the performance of acoustic resonators near resonance conditions.

5.7.4 Coupled Acoustic-Piezoelectric Models

ANSYS is used to build a coupled model containing both piezoelectric and acoustic elements for the acoustic resonators driven by piezoelectric bimorphs. Figure 5.38 shows the first pressure mode shape predicted by the ANSYS model for the acoustic resonator shown in Figure 5.34) which is driven by a 3” piezoelectric bimorph whose properties are listed in Table 5.1. The first natural frequency predicted by the coupled

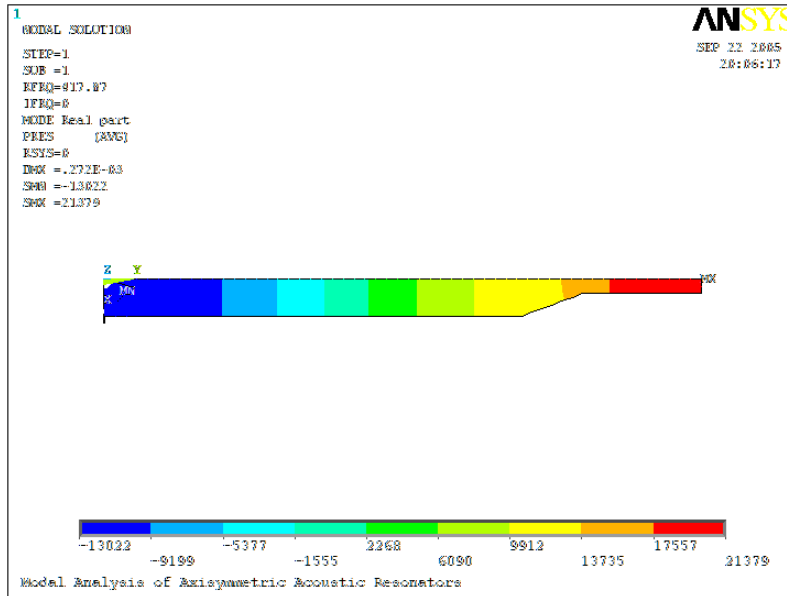


Figure 5.38: **First mode of a 20” acoustic resonator driven by a 3” piezoelectric bimorph.**

ANSYS model is 417 Hz which is very close to the fundamental frequency of the acoustic resonator in the uncoupled model. This suggests that the coupling between both models in ANSYS is weak.

5.7.5 Resonators with Intermediate Diaphragm

Figure 5.39 shows the pressure distribution as predicted by the ANSYS model for a 0.5 m long resonator without (a) and with (b) a diaphragm. Ansys predicts higher pressure ratios to be achieved using the diaphragm.

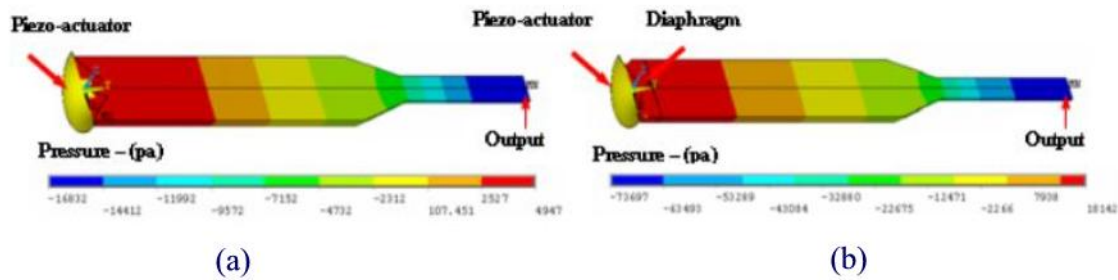


Figure 5.39: Pressure distribution predicted by the ANSYS model for a 0.5 m long resonator (a) without the diaphragm and (b) with the diaphragm.

5.8 Summary

In this chapter, the proposed finite element models for different cases have been experimentally evaluated. For the case of entirely driven resonators, the predictions of the proposed model are in a very good agreement with experimental results in both time and frequency domains. However, discrepancies become noticeable at higher accelerations. In the case of piston driven resonators, the piston is driven by either a shaker or a piezoelectric stack actuator. The results are again matching the predictions of the proposed model.

Also, when compared to the experimental results available in the literature, the predictions of the gas model at different frequencies are in very good agreement with the measurements obtained by Galiev *et al.* [22]. This makes the proposed model probably the first theoretical model to match these experiments that were carried out more than three decades ago. Experiments also showed that a D.C. flow can be obtained from axisymmetric resonators which definitely affects the pressures

developed inside. The model used for axisymmetric piezoelectric bimorphs is proved valid by being able to predict the natural frequencies of the bimorph. When coupled to gas-filled axisymmetric resonators, the model is able to predict the natural frequencies of the coupled system with a great accuracy. However, the developed pressures are too modest. This may be due to the fact that the used bimorphs are too soft since they are not designed for this type of application.

The developed finite element models are also compared to corresponding models developed on the ANSYS software. The natural frequencies of the axisymmetric acoustic cavities predicted by the proposed finite element model and that of the ANSYS are in perfect match, basically because both models are based on the same linear equations. The natural frequencies of the piezoelectric bimorph predicted by the developed model are 11% less than those of ANSYS. However, the experimentally measured value lies somewhere in between. The ANSYS predictions for a cylindrical cavity excited at its fundamental frequency behave just like equation (1.4) where it predicts large pressure oscillations in both compression and vacuum directions. In general, the proposed model is tailored to accurately simulate the nonlinear behavior of gas oscillations under harmonic excitations. Accordingly, its predictions for the system performance are superior to the predictions of commercial finite element software.

Chapter 6

Contributions and Future Work

6.1 Contributions

A mathematical model for gas oscillations in axisymmetric resonators has been developed starting from the basic nonlinear governing equations. Basically, the model can be solved in a weighted residual form to predict the pressure profile inside the resonator. From an application point of view, the model has several deficiencies as it is able only to deal with simple geometries and limited boundary conditions. However, the mathematical model is able to capture phenomena like gas stiffening frequency shifts and shock waves. A finite element model is developed to overcome these deficiencies starting from the weak form of the governing equations. The proposed model shows many advantages including

- being able to model resonators with any axisymmetric geometry including multi-segmented cavities in which each segment has an independent geometrical description and hence its ability of dealing with complicated resonator designs is increased,
- having a low computational cost since all integrals have been converted to discretized summations of simple functions over the elements. The computation time is independent of the complexity of the resonator geometry and is only a function in the number of elements and used modes,
- being based on the weak integral form enables incorporating the boundary conditions into the governing equations. Thus, the model can handle both entirely and piston driven resonators in a standard way without the need for selecting tricky basis and/or weight functions,
- being able to model more practical cases; namely axisymmetric resonators with flow across the boundaries.

The proposed finite element model is ready to be used for optimization purposes to select the resonator geometries which yield high pressure ratios desirable for many applications.

Axisymmetric piezoelectric bimorphs have also been modeled using the theory finite elements. The acoustic as well as the piezoelectric finite element models have been coupled together in one. The coupled model accounts for the dynamics of the acoustic fluid, the piezoelectric bimorph as well as the interaction between them by

including the effect of the acoustic pressure on the bimorph and vice versa. The importance of using a coupled model has been demonstrated theoretically and can be used as a tool to design piezoelectric actuated compressors which are clean, efficient, compact, and environment friendly as compared to other types.

The model was also experimentally validated both in the time and frequency domains. The nonlinear behavior of the gas being excited was captured by the model. The model was able to accurately match the wave forms of the experiments carried on by Galiev *et al.* [22] for the first time in more than three decades. Some experiments were carried using resonators entirely driven by electromechanical shakers, and piston driven either by a shaker or a piezoelectric stack actuators. In all these cases, experimental results were in a good agreement with the model predictions. Prototypes for axisymmetric resonators driven by piezoelectric bimorphs have been built and used to show that their natural frequencies match those predicted by the finite element model for the coupled system. However, the developed pressures were much less than the predicted ones which may be attributed to the fact that the available piezoelectric bimorphs have low control authority.

6.2 Future Work

6.2.1 Resonator Geometry Optimization

The developed finite element models can be used in resonator optimization. That is to say, to investigate the variation of the pressure wave that results from resonators with different geometrical shapes as the pressure ratio is highly dependent on the resonator geometry. The piezoelectric bimorph also has to be designed to be able to withstand the acoustic pressure while working efficiently. More importantly it is essential to optimally select the resonator/actuator combination that produced the maximum energy conversion efficiency.

6.2.2 Double Cavity Resonator

It is important to note that efforts should be exerted on the development of double cavity resonator as shown in Figures 6.1 and 6.2 in which two identical cavities are placed back to back with a piston in between. Such configuration can be very effective in increasing the output gas flow. There are two options for driving this configuration; either to have a piezoelectric bimorph in between or a piston mounted on disc springs which are selected such that the overall system (the mass of the piston and the stiffness of the springs) have their natural frequency in the neighborhood of the resonant frequency of the acoustic cavities. During operation, the whole resonator is excited at the desired frequency with certain amplitude. This will cause the piston

to oscillate at the same frequency at a much larger amplitude.

The advantages sought in this double cavity resonator include (1) increasing the efficiency by allowing the back and forth oscillations of the piston to excite air from both sides, (2) doubling the output of the resonator, and (3) reducing the noise emitted from the resonator by making the piston as an internal part of the resonator.

6.2.3 Piezo-Acoustic Actuation System

The development of a Piezo-Acoustic Actuation System (**PAAS**) will be a natural extension of the present work. Figure (6.3) shows a preferred configuration of that system in which the piezo-acoustic resonator (PAR) module, shown inside the dashed box; is integrated with an array of pneumatic components, sensors and controllers. The pneumatic components include an accumulator to regulate the flow fluctuations of the PAR, a directional control valve to control the travel direction of the load, and a pneumatic actuator to position the load. The input excitation to the piezo-actuator is controlled in response to the load to achieve optimal impedance matching conditions. Also, the position of the load is monitored using a position sensor and its travel direction is controlled by a dedicated position controller.

With such sensing and control capabilities, the performance of the PAAS system can be enhanced and its efficiency can be maximized. The system can be used in various vibration and shape control applications.

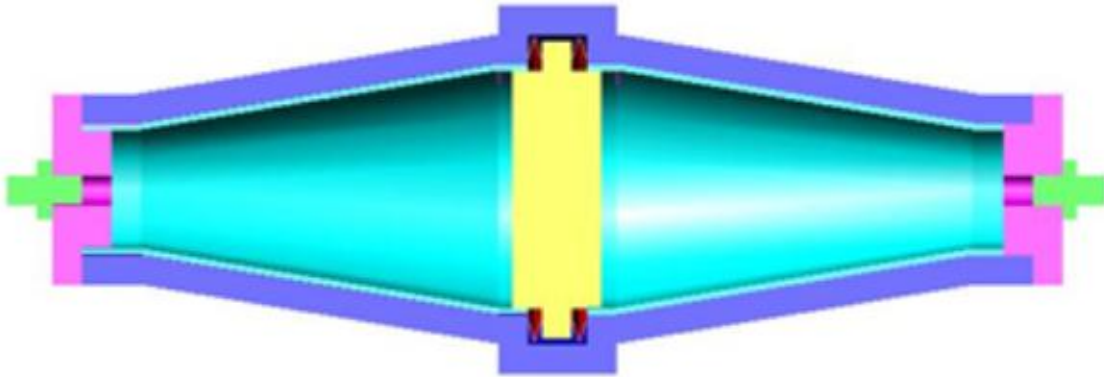


Figure 6.1: A schematic for a double cavity resonator.

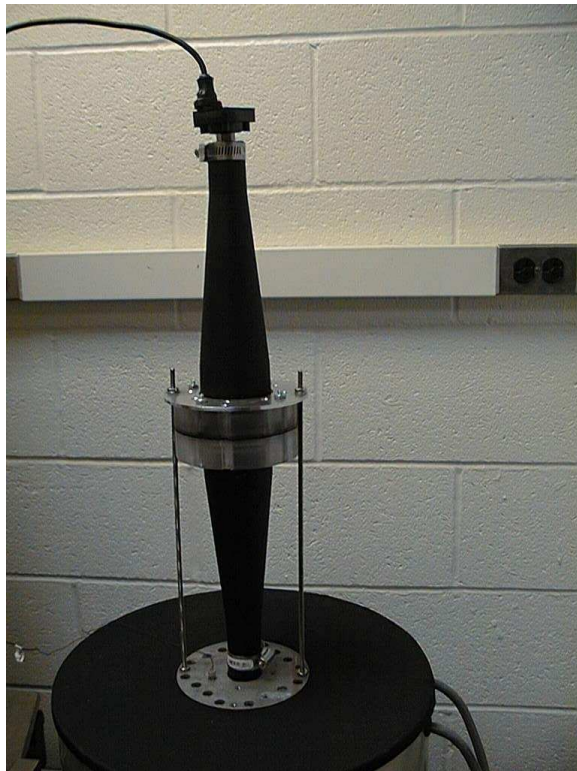


Figure 6.2: A double cavity resonator mounted on an electromechanical shaker.

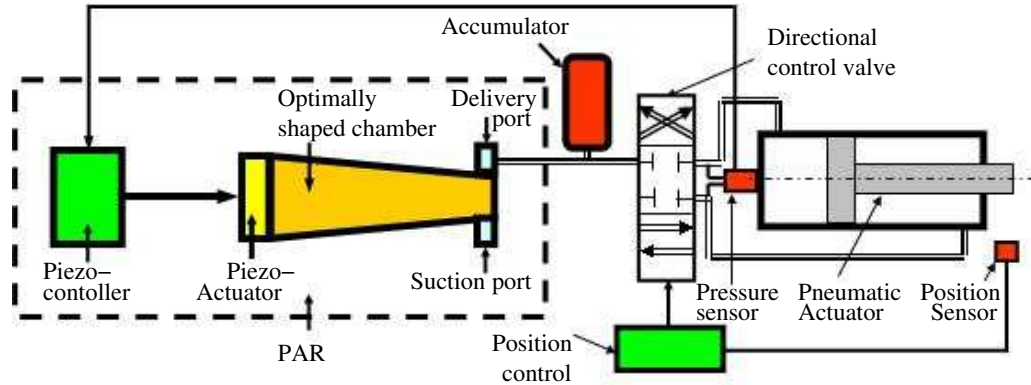


Figure 6.3: A Piezo-Acoustic Actuation System (PAAS).

6.2.4 Refrigeration Compressors

Another valuable extension of the present work is to investigate the utilization of the acoustic resonator as a Piezo-Acoustic Refrigerator (**PAR**) to replace classical refrigeration compressors in an attempt to improve the reliability and avoid unnecessary failures.

In this regard, work is needed to:

1. determine the performance characteristics of the refrigerator will be determined with the PAR as compared with the performance of conventional hermetic compressor.
2. determine experimentally the performance of the PAR while operating in a domestic refrigerator using refrigerant R134A by replacing a conventional hermetic compressor as shown in Figure (6.4).
3. determine the merits and limitations of the PAR as a refrigeration compressor

in domestic refrigerators.

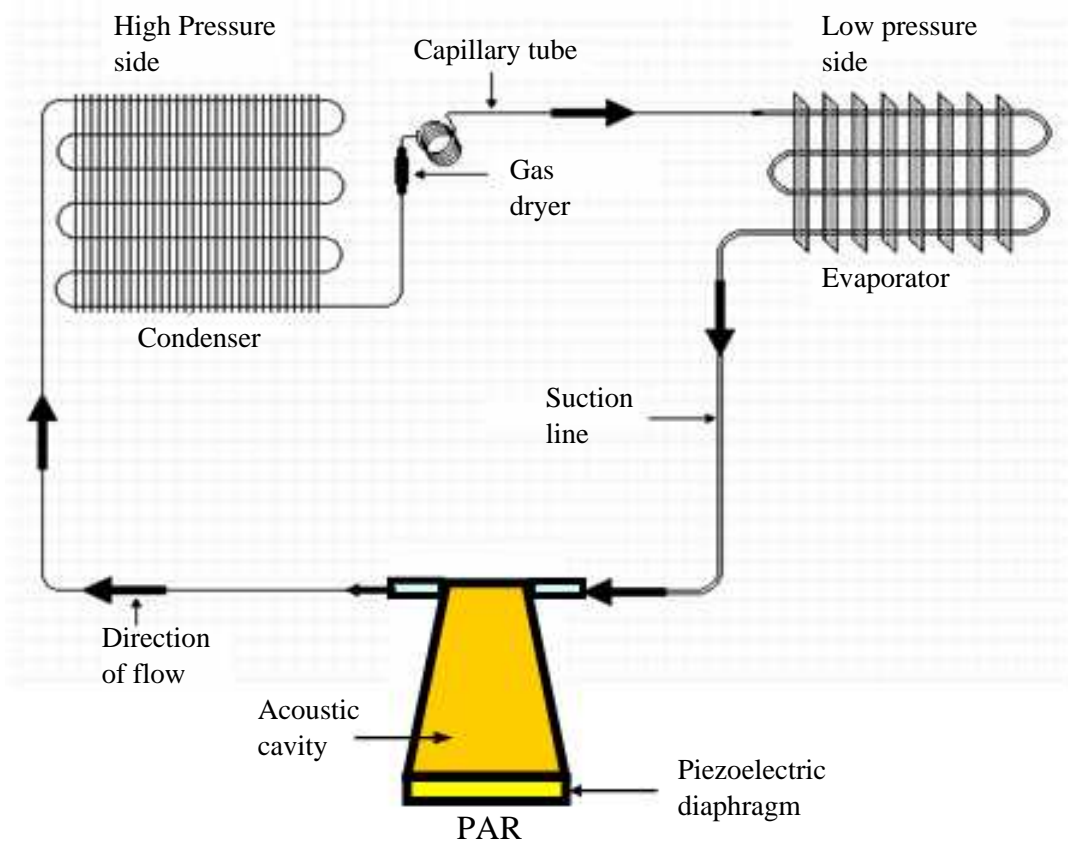


Figure 6.4: Use of PAR as a refrigeration compressor.

BIBLIOGRAPHY

- [1] S. Rayleigh, “The Theory of Sound”, Dover Books, 2nd edition, 1945.
- [2] J. Hartmann, “New Method for the generation of Sound Waves”, Physical Review Series II **20**, 719 - 729, 1922.
- [3] M. Ilgamov, R. Zaripov, R. Galiullin, and V. Repin, “Nonlinear Oscillations of a Gas in a Tube”, Applied Mechanics Reviews **49**(3), 137-154, 1996.
- [4] E. Lettau, “Messungen an Schwingungen von Grassanlen mit Steilen Fronten in Rohrleitungen”, Deutsche Kraftfahrforschung **39**, 1 - 10, 1939.
- [5] B. Coppens and J. V. Sanders, “Finite Amplitude Standing Waves in Rigid-Walled Tubes”, Journal of the Acoustical Society of America **52**, 1024 - 1034, 1968.
- [6] S. Temkin, “Nonlinear Gas Oscillations in a Resonant Tube”, The Physics of Fluids **11**, 960 - 963, 1968.
- [7] S. Temkin, “Selective Damping of Resonant Acoustic Waves in Tubes”, Journal of Sound and Vibration **36**, 389 - 398, 1974.

- [8] B. Sturtevant, “Nonlinear Gas Oscillations in Pipes. Part 2: Experiment”, *Journal of Fluid Mechanics* **63**, 97 - 120, 1974.
- [9] R. Zaripov and M. Ilgamov, “Nonlinear Gas Oscillations in a Pipe”, *Journal of Sound and Vibration* **46**, 245 - 257, 1976.
- [10] R. Saenger and G. E. Hudson, “Periodic Shock Waves in Resonating Gas Column”, *Journal of the Acoustical Society of America* **32**(8), 961 - 971, 1960.
- [11] D. Cruikshank, “Experimental Investigation of Finite-Amplitude Acoustic Oscillations in Closed Tubes”, *Journal of the Acoustical Society of America* **52**, 1024 - 1034, 1972.
- [12] C. Lawrenson, B. Lipkens, T. Lucas, D. Perkins, and T. Van Doren, “Measurements Of Macrosonic Standing Waves In Oscillating Closed Cavities”, *Journal of the Acoustical Society of America* **104** (2), Pt. 1, 623 - 636, 1998.
- [13] P. Merkli and A. Thomann, “Thermoacoustic Effects in a Resonant Tube”, *Journal of Fluid Mechanics* **70**, 161 - 177, 1975.
- [14] R. Althaus and A. Thomann, “Oscillations of a Gas in a Closed Tube Near Half the Fundamental Frequency”, *Journal of Fluid Mechanics* **183**, 147 - 161, 1987.
- [15] R. Ladbury, “Ultra-High Energy Sound Waves Promise New Technology”, *Physics Today*, February 1998.

- [16] D. Gaitan and A. Atchley, “Finite amplitude standing waves in harmonic and anharmonic tubes”, *Journal of the Acoustical Society of America* **93**, 2489-2495, 1993.
- [17] N. Sugimoto, M. Masuda, T. Hashiguchi, and T. Doi, “Annihilation of Shocks in Forced Oscillations of an Air Column in a Closed Tube (L)”, *Journal of the Acoustical Society of America* **110** (5), 2263 - 2266, 2001.
- [18] R. Betchov, “Nonlinear Oscillations of a Column of Gas”, *The Physics of Fluids* **1**(3), 205 - 212, 1958.
- [19] S. Weiner, “Standing Waves of Finite Amplitudes”, *Journal of the Acoustical Society of America* **40**, 240 - 243, 1966.
- [20] S. Temkin, “Propagating and Standing Sawtooth Waves”, *Journal of the Acoustical Society of America* **45**, 224 - 227, 1969.
- [21] W. Chester, “Resonant Oscillations in a Closed Tube”, *Journal of Fluid Mechanics* **18**, 44 - 64, 1964.
- [22] S. Galiev, M. Ilgamov, and A. Sagykov, “Periodic Shock Waves in Gas”, *Izv. Acad. Nauk. SSSR, Mekhanika Jidkosti I Gaza*, **2**, 57 - 66, 1970.
- [23] Y. Ilinskii, B. Lipkens, T. Lucas, T. Van Doren, and E. Zabolotskaya, “Nonlinear Standing Waves in an Acoustical Resonator”, *Journal of the Acoustical Society of America* **104** (5), 2664 - 2674, 1998.

- [24] Y. Chun and Y. Kim, “Numerical Analysis for Nonlinear Resonant Oscillations in Closed Tubes”, *Journal of the Acoustical Society of America* **108** (6), 2765 - 2774, 2000.
- [25] R. Erickson and B. Zinn, “Modeling of Finite Amplitude Acoustic Waves in Closed Cavities Using the Galerkin Method”, *Journal of the Acoustical Society of America* **113** (4), 1863 - 1870, 2003.
- [26] W. Boyce and R. DiPrima, “Elementary Differential Equations and Boundary Value Problems”, 4th ed., Wiley, New York, 1986.
- [27] L. Meirovitch, “Fundamentals of Vibrations”, McGraw-Hill, 2000.
- [28] C. Vanhille and C. Campos-Pozuelo, “Numerical Model for Nonlinear Standing Waves and Weak Shocks in Thermoviscous Fluids”, *Journal of the Acoustical Society of America* **109** (6), 2660 - 2667, 2001.
- [29] N. Sugimoto, M. Masuda, T. Hashiguchi, and T. Doi, “Frequency Response of Nonlinear Oscillations of Air Column in a Tube with an Array of Helmholtz Resonators”, *Journal of the Acoustical Society of America* **114** (4), 1772 - 1784, 2003.
- [30] Alexeev, A. Goldshtein, and C. Gutfinger, “Heat Interaction in a Resonance Tube”, *Physics of Fluids* **14** (5), 1812 - 1815, 2002.
- [31] X. Li, J. Finkbeiner, G. Raman, C. Daniels, and B. Steinetz, “Nonlinear Resonant Oscillations of Gas in Optimized Acoustical Resonators and the Effect of

- Central Blockage”, AIAA-2003-368, 41st Aerospace Sciences Meeting and Exhibit, Reno, Nevada, Jan. 6 - 9, 2003.
- [32] X. Li, J. Finkbeiner, G. Raman, C. Daniels, and B. Steinetz, “Optimized shapes of oscillating resonators for generating high-amplitude pressure waves”, of the Acoustical Society of America, **116**(5), 2814 - 2821, 2003.
- [33] C. Daniels, J. Finkbeiner, B. Steinetz, X. Li, and G. Raman, “Nonlinear Oscillations and Flow of Gas Within Closed and Open Conical Resonators”, AIAA-2004-677, 42nd AIAA Aerospace Sciences Meeting and Exhibit, Reno, Nevada, Jan. 5 - 8, 2004.
- [34] R. Meirovitch and A. Acosta, “Fluid Flow: A First Course in Fluid Mechanics”, The Macmillan Company, New York, 1964.
- [35] H. Oberst, “A method for the production of extremely powerful standing waves in air”, *Akust. Zh.* **5**, 27 - 38, 1940. The article was translated by R. T. Beyer.
- [36] S. Garrett and S. Backhaus, “The Power of Sound”, *American Scientist*, November - December 2000.
- [37] J. Smits, S. Dalke, and T. Cooney, “The Constituent Equations of Piezoelectric Bimorphs”, *Sensors and Actuators A*, **28**, 41 - 61, 1991.
- [38] F. Chong, Y. Lee, and C. Ng, “Vibration and Sound Radiation from Plates Excited by Piezoelectric Actuators”, *Building Acoustics*, **8** (3), 179-198, 2001.

- [39] C. Nguyen, and S. Pietrzko, “Piezoelectric-Mechanical-Acoustic Couplings from a PZT-Actuated Vibrating Beam and its Sound Radiation”, *Mechanical Systems and Signal Processing*, **18**, 929 - 945, 2004.
- [40] A. Dobrucki, and P. Pruchnicki, “Theory of Piezoelectric Axisymmetric Bimorph”, *Sensors and Actuators A*, **58**, 203 - 212, 1997.
- [41] W. Flügge, “Stresses in Shells”, Springer-Verlag, 1962.
- [42] A. Kalinichev, J. Bass, C. Zha, P. Han, and D. Payne, “Elastic Properties of Orthorhombic KNbO₃ Single Crystals by Brillouin Scattering”, *Journal of Applied Physics*, **74**(11), 6603 - 6608, 1993.
- [43] A. H. Nayfeh and B. Balachandran, “Applied Nonlinear Dynamics: Analytical, Computational and Experimental Methods”, John Wiley & Sons, Inc. 1995.
- [44] The Lee Company. LFPA Series Piezoelectric 2-Way Air Valves. Retrieved September 13, 2005 from www.theleeco.com